ORNL/TM-7958

ornl

OAK RIDGE NATIONAL LABORATORY

UNION CARBIDE

Evaluation of Tubular Ceramic Heat Exchanger Materials in Acidic Coal Ash from Coal-Oil-Mixture Combustion

M. K. Ferber
V. J. Tennery

Fossil Energy Program

OPERATED BY
UNION CARBIDE CORPORATION
FOR THE UNITED STATES
DEPARTMENT OF ENERGY

ORNL/TM-7958

Contract No. W-7405-eng-26

METALS AND CERAMICS DIVISION

EVALUATION OF TUBULAR CERAMIC HEAT EXCHANGER MATERIALS IN ACIDIC COAL ASH FROM COAL-OIL-MIXTURE COMBUSTION

M. K. Ferber and V. J. Tennery

Date Published: December 1981

Work sponsored by the Department of Energy
Pittsbury Energy Technology Center under
contract W-7405-eng-26 with Union Carbide
Corporation.

OAK RIDGE NATIONAL LABORATORY
Oak Ridge, Tennessee 37830
operated by
UNION CARBIDE CORPORATION
for the
DEPARTMENT OF ENERGY

CONTENTS

EVALUATION OF TUBULAR CERAMIC HEAT EXCHANGER MATERIALS IN ACIDIC COAL ASH FROM COAL-OIL-MIXTURE COMBUSTION

M. K. Ferber and V. J. Tennery

ABSTRACT

In a continuing study of the long-term chemical and structural stability of candidate heat exchanger ceramics, tubes of five different structural ceramic materials were exposed to the hot combustion gases from a coal-oil-mixture (COM) fuel in the Ceramic Recuperator Analysis Facility (CRAF) at about 1200°C for about 500 h. Air flow through each tube produced a temperature gradient across the tube wall, thereby simulating the condition in a tubular heat exchanger element. As-received and exposed materials and solidified coal slag were examined by optical microscopy, scanning electron microscopy, electron microprobe, energy-dispersive x-ray analysis, x-ray diffraction, x-radiography, and chemical analysis to identify degradation processes. Several important properties of the materials, including room-temperature helium permeability, room-temperature C-ring fracture strength, and thermal expansion from room temperature to 1100°C were measured for both as-received and exposed specimens.

The five structural ceramics included three types of silicon carbide, a high-purity alumina, and a newly available sialon. Siliconized SiC, sintered α-SiC, and chemically vapor deposited (CVD) SiC survived the long-term exposure with no major visible degradation. The alumina and sialon tubes were cracked extensively. Acidic coal slag deposited extensively on the upstream surface of all tubes. During cooldown, the slag did not strongly bond to any of the silicon carbide tubes, but a strong bond was developed with the alumina and sialon tubes. Thermal expansion differences between the bonded coal slag and the tubes caused significant tensile stresses in the tubes during cooling, apparently resulting in the observed fractures for alumina and sialon tubes.

Significant transport of various elements into and out of the ceramics occurred during the exposure to the hot coal slag. The silicon carbides corroded by a micropitting oxidation at the carbide-slag interface. The SiC and Si phases of siliconized SiC corroded at essentially the same rate. Recession rates for the outer surface of all these tubes were minimal during the exposure.

Exposure to the hot coal slag increased the room-temperature helium permeability of all the SiC-based tubes by one to two orders of magnitude. The room-temperature C-ring fracture strength increased modestly in siliconized SiC and essentially remained the same in both sintered α and CVD SiC.

The thermal expansion of some of these materials increased substantially from the exposure, and these increases were different in some cases for the upstream and downstream specimens from a given tube. For KT and CVD SiC, both the upstream and downstream sides exhibited expansion increases up to about 17% at 1000°C. Sintered α-SiC had much smaller increases. The high-Al_2O_3 tube had an expansion increase of about 14% on the upstream side at 1000°C but the downstream side was essentially unchanged. These substantial thermal expansion increases could generate significant stresses in long ceramic heat exchanger tubes, and the origin of these increases is under investigation.

INTRODUCTION

Fixed-boundary heat exchangers (HXs) serve important functions in the operation of fossil energy conversion systems. To date, HXs employed in energy conversion systems, such as coal-fired electrical generating plants, have been fabricated of alloys. The evolution of engineering alloys for HX applications has played a crucial role in achieving present steam-cycle power plant efficiencies of about 30%. Advanced fossil energy conversion systems, which have the potential for significantly higher energy conversion efficiencies compared with state-of-the-art steam-cycle systems, have received considerable attention in the United States in recent years. Several system configurations have been analyzed, and the general results of these analyses form one basis for this work on ceramic materials for HX applications. As is well known, the thermodynamic efficiency of a heat-engine-based energy conversion cycle is proportional to the difference between the temperature of the working fluid that drives the engine and the exhaust fluid temperature, if other factors are maintained constant. Major efforts have been made in both steam-cycle and hot gas turbine systems to develop materials to operate at even higher temperatures because of the accompanying increase in efficiency. In steam systems, this limit is dictated by the corrosion and mechanical properties of alloys in the steam generators (HXs). In gas turbine systems, this limit is dictated by the corrosion and mechanical properties of available alloys for use in the turbine-machinery. Hot gas turbines can operate with much higher working fluid temperatures than steam-cycle systems and thus have the potential of providing relatively high system conversion efficiencies if the energy losses in the exhaust are adequately minimized.

In systems up to several megawatts capacity, this heat is most conveniently utilized in a steam bottoming turbine. Alloys and the technology for their use in directly fired hot gas turbines are highly developed. The alloys are generally sensitive to particulate and corrosive degradation by species in the combustion gases. Because of the increasing emphasis on use of domestic fuels such as coal and synthetic fuels to supplant imported oil in electrical energy generating systems along with the required higher conversion efficiencies to reduce bus bar energy costs, the operation of hot gas turbines with heat derived from relatively dirty fuels is of growing importance. There are currently two conceptual means for achieving this goal. One, which has received major attention in recent years in DOE programs, is to remove damaging particulates from the hot combustion gases with hot cyclones before the gases enter the turbine. This mode of operation requires both pressurized combustors and cyclones in order to deliver the hot gas at the required pressure to the turbine inlet. The other concept, which has received relatively little attention, employs a high-temperature HX to isolate the turbine from potentially damaging species in the combustion gases. In this configuration, the combustor does not require pressurization but the secondary side of the HX must operate at essentially the turbine inlet pressure. Heat from the combustion gases is transferred through the HX wall to a second gas, which in turn drives the turbine. In this latter concept the material employed in the HX must be able to operate at temperatures well above the turbine inlet temperature, which can be 1350°C or higher, and still possess acceptably low corrosion, strength degradation, and creep while operating under high stresses. Selected structural ceramic materials are good candidates for use in this type of HX because their known high-temperature strength in relatively clean oxidizing environments offers promise for their use in highly contaminated environments.

In additional fossil energy system applications ceramic HXs could serve a unique function, including pressurized fluidized bed combustors (PFBCs) and coal gasifiers. In the former application, ceramic tubes in the bed would be employed to heat a gas such as air to operate a gas turbine or perhaps generate steam in a secondary HX. In the coal gasifier system, the gasifier product gas could be burned on the primary side of

the HX to heat a clean gas on the secondary side to operate a gas turbine. Alternatively, the HX could be used to extract high-quality sensible heat from the gas product stream before gas cleanup by water scrubbing.

We investigated the behavior of five structural ceramic materials currently considered for use in HXs, including three types of silicon carbide, high-purity Al_2O_3, and a sialon ceramic. Tubes of these materials were exposed to hot gases from coal combustion for 496 h in the Ceramic Recuperator Analysis Facility (CRAF) at ORNL. The material specimens were analyzed to determine if exposure to the coal slag changed their properties significantly. The combustion gas temperature and ceramic tubular specimen orientation in the CRAF simulated conditions for tubes in a ceramic tubular cross flow HX interfaced with a coal combustor. The combustion gas temperature at the tube positions was about 1350°C. The outer tube wall temperatures were about 1240°C, and air flowing through the tubes was heated to about 400°C. Coal was delivered to the CRAF burner in a coal-oil-mixture (COM) consisting of 10 wt % bituminous coal and about 90 wt % No. 6 oil. During the exposure 291 kg of coal ash was delivered by the combustor to the CRAF chamber. As far as we are aware, this work represents the longest exposure of candidate ceramic HX materials to actual coal combustion conducted anywhere to date. Following the exposure, helium permeability, microstructure, composition, fracture strength, and thermal expansion of the ceramic tubes were determined and compared with the as-received properties.

Previously, a 500-h combustion gas exposure of 14 different ceramic materials was completed in the CRAF, in which a relatively high-impurity No. 6 oil was burned. The tube configurations and tube wall temperatures for this first CRAF test were very similar to those employed in this second materials test. In CRAF Test 2, which is the subject of this report, only materials that were employed in the earlier test and showed promise of having reasonable stability in these environments were included. In addition, a new sinterable sialon was included to determine its behavior under these conditions.

EXPERIMENTAL

Ceramic Recuperator Analysis Facility

The CRAF at ORNL is a unique facility dedicated to long-duration exposures of candidate HX materials to hot combustion gases of fossil fuels. Details of its design and construction have been published previously.[1] The CRAF is capable of generating heat by the fuel combustion at a rate of up to 0.9 MW and therefore is of a scale that approximates at least the smaller combustor systems that are of interest for advanced fossil energy conversion systems. An isometric drawing of the CRAF is shown in Fig. 1. The tubular ceramic specimens were held, as shown in Fig. 1, between two refractory header blocks so as to be perpendicular to the flow of hot combustion gases from the burner. For this particular exposure, the design of the housing above the section containing the tubes was modified slightly from that shown in Fig. 1 to permit another materials exposure to be conducted above the tube array. This configuration is shown in Fig. 2 with the unit at temperature, with the combustion gas plume visible at the exit port.

Tubular specimens of the five ceramic materials included in the exposure were mounted between the refractory oxide header blocks as described previously.[1] Two tubes of each material were mounted in a single row across the CRAF test duct as shown in Fig. 3. Figure 3(a) is a view of the upstream side of the tube row, that is, the lower side of the tubes, which faces the combustor chamber. Figure 3(b) is a view of the downstream side of the tube row, or the upper side, showing the thermocouples located at the midspan of each tube. The thermocouple wires exit the duct through the air inlet header block. Temperatures at the outer surfaces of the tubes were continuously measured with Pt vs Pt–10% Rh thermocouples attached to the downstream sides of the tubes. A high-alumina (Degussit 81-50-010) cement was applied to the thermocouple junctions to protect them from degradation by reaction with the tube materials or the fuel combustion products. Appropriate thermocouple compensation wire was used to connect the thermocouples to multipoint recorders.

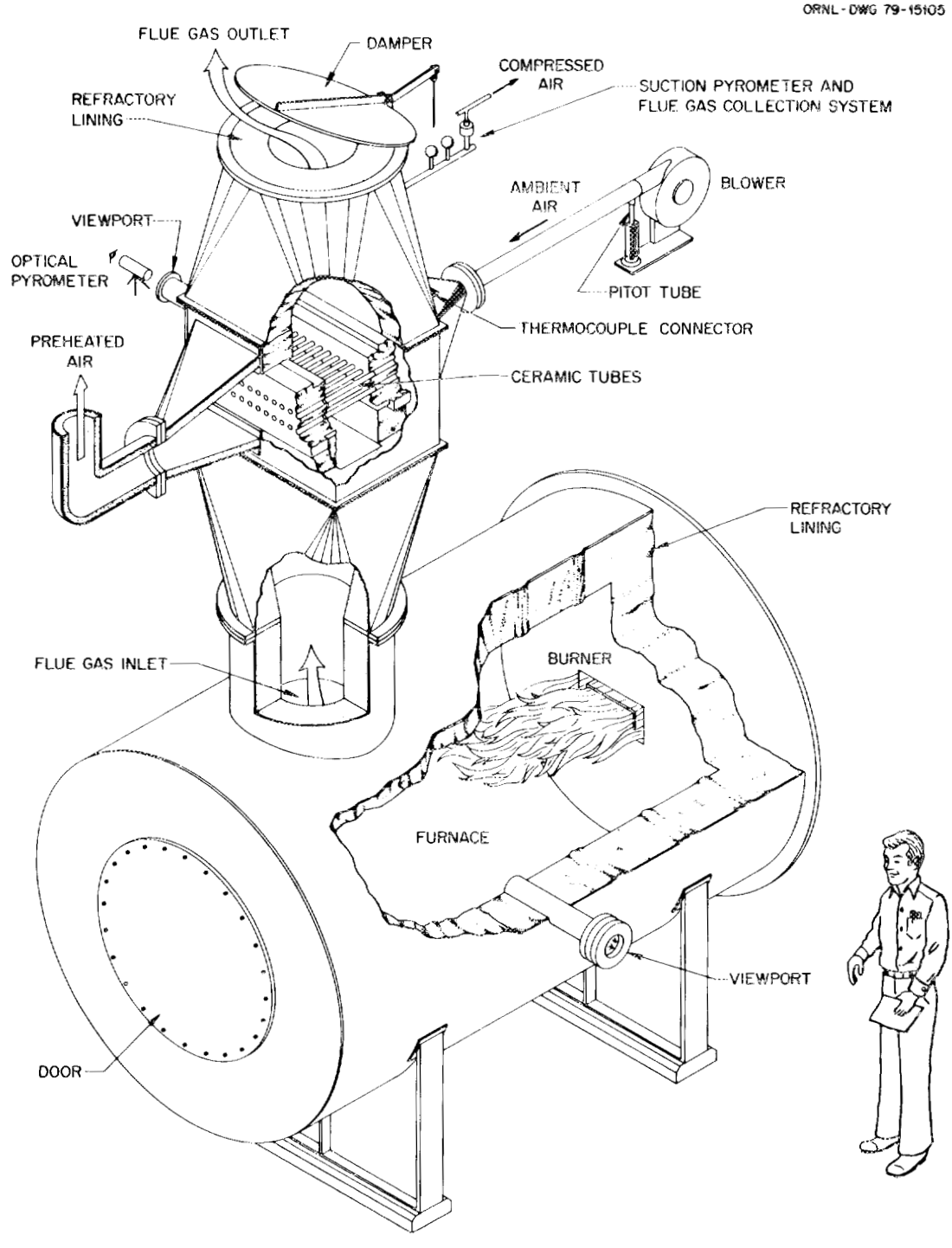

Fig. 1. The Ceramic Recuperator Analysis Facility dedicated to evaluation, testing, and analysis of ceramic heat exchanger materials by long-term exposure to fossil fuel combustion products.

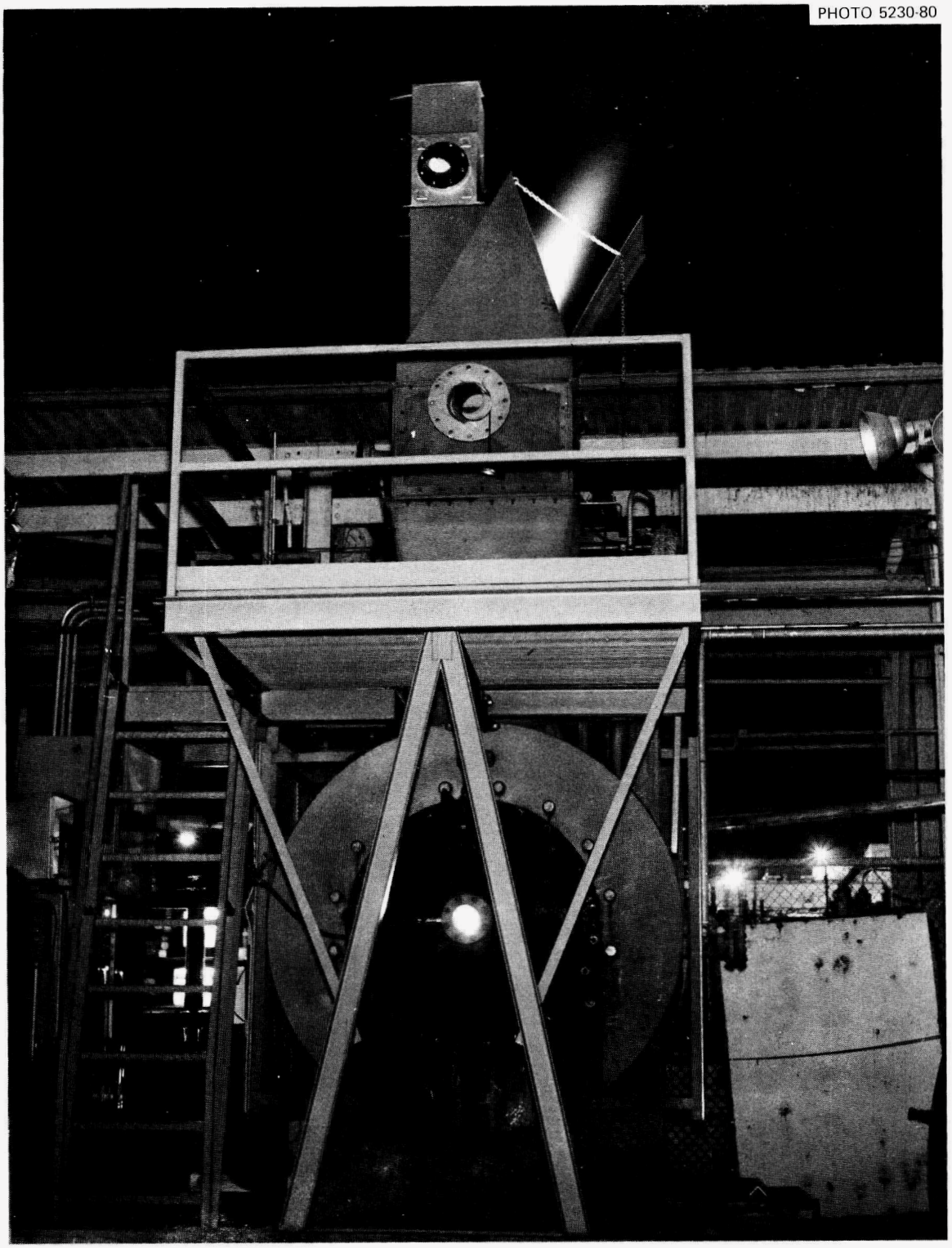

Fig. 2. Ceramic Recuperator Analysis Facility at temperature during CRAF Test 2.

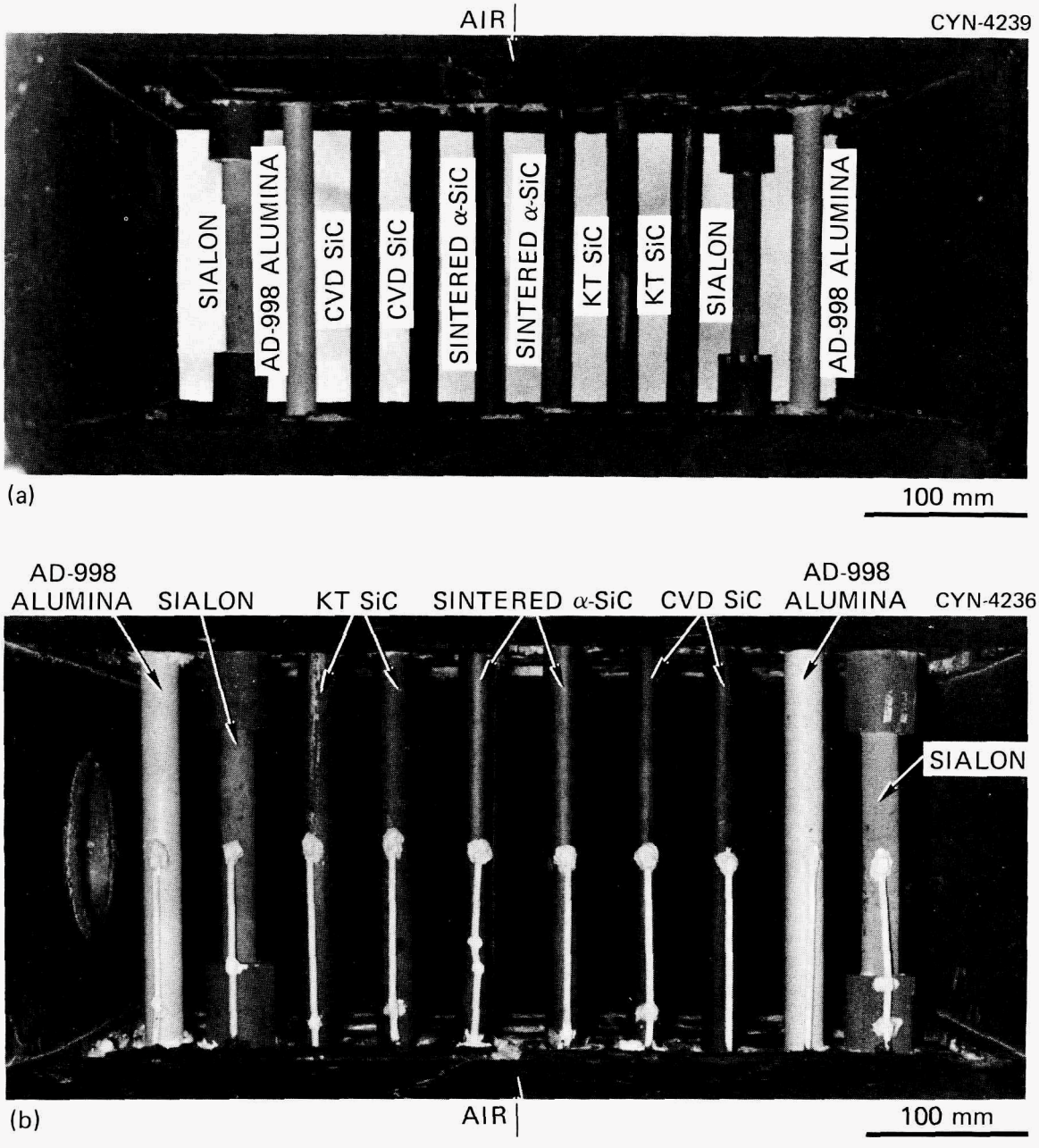

Fig. 3. The positions of individual ceramic tubes in the ten-tube array mounted in the flue gas duct before the CRAF Test 2 exposure. (a) Upstream side. The flue gas flow direction was into the page. (b) Downstream side. The flue gas flow direction was away from the page.

Secondary air supplied by an auxiliary fan flowed through the tubes during CRAF Test 2 so that they operated as HX elements in a cross-flow mode (Fig. 4). The air velocity was measured with a Dwyer* pitot tube located in the 100-mm ID pipe running from the exit of the secondary blower to the air inlet transition of the CRAF. In addition, the pressure was determined with the aid of a hydrometer. The temperature of the preheated secondary air exiting the tubes was measured with a water-cooled, radiation-shielded suction pyrometer.† This instrument, which was also used to measure the flue gas inlet and outlet temperatures, included a collection system for flue gas condensables and noncondensables present in the flow path. Complete details are given elsewhere.[1]

*Product of Dwyer Instruments, Inc., Michigan City, Ind.

†Land SU 6/5/12/1 suction pyrometer, product of Land Instruments, Inc., Tallytown, Pa.

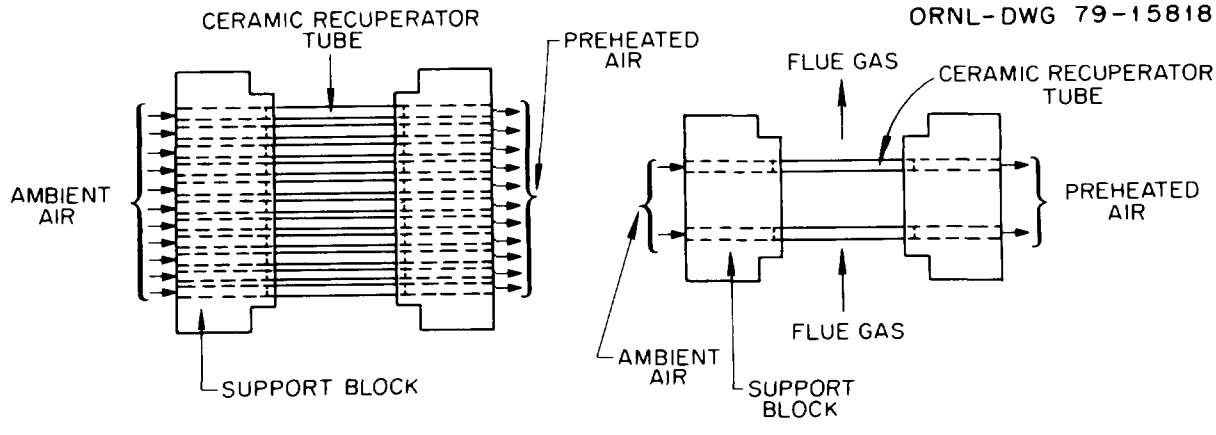

TOP VIEW OF CERAMIC RECUPERATOR TUBES MOUNTED IN SUPPORT BLOCKS. NOTE FLUE GAS FLOW DIRECTION IS OUT OF THE PAGE.

SIDE VIEW OF CERAMIC RECUPERATOR TUBES MOUNTED IN SUPPORT BLOCKS. NOTE THE CERAMIC TUBES ARE ARRANGED IN A TWO-ROW, STAGGERED CONFIGURATION.

Fig. 4. Ceramic heat exchanger tubes mounted in ceramic support blocks.

Ceramic Recuperator Analysis Facility Test 2 Conditions

The fuel used in the CRAF combustor was a COM, which consisted of 10 wt % powdered bituminous coal in a Venezuelan-crude-derived No. 6 fuel oil. The results of a chemical analysis of the coal reported by the vendor are given in Table 1. This coal was finely divided, with 98% of the particles being smaller than 44 μm. The ash was characterized by high concentrations of SiO_2, Fe_2O_3, and Al_2O_3 as equivalent oxides. In addition, the low base-to-acid ratio of 0.29 was expected to produce a viscous slag for the operation temperatures used in CRAF Test 2.

Before the long-term exposure, the stability of the COM in the CRAF combustor was demonstrated for furnace temperature up to 1400°C. About 1.9 m^3 (500 gal) of the 10 wt % COM fuel was received for these initial firing tests. The furnace was maintained at about 680°C by means of an auxiliary natural gas burner when COM fuel was not used. For the actual long-term test, the furnace was heated to approximately 1400°C with the COM at an average heating rate of 0.040°C/s (145°C/h). This resulted in a heating rate of 0.018°C/s (64°C/h) in the vicinity of the tubes. The average tube temperature was 1230°C. The furnace temperature was controlled by an oil flow valve, which was regulated by a Barber-Coleman PAT Controller.* A programmed μ-Datatrak† was used to obtain the desired temperature-time schedule. The total exposure time at the 1230°C tube temperature was 496 h. Two 18-m^3 (4750-gal) shipments of COM fuel were consumed during this period at an average rate of 0.076 m^3/h (20 gal/h). The total exposure time at 1230°C obtained from the first shipment was 290 h.

Several minor difficulties were encountered during the pumping and firing of the COM fuel. For example, first a small oil pump at the combustor malfunctioned, and later the pump that delivered the COM fuel from the trailer became blocked. The openings in the burner nozzle were also

---

*Barber Coleman PAT Controller: Product of Barber-Coleman Co., Rockford, Ill.

†μ-Datatrak: Product of Research Inc., Minneapolis, Minn.

Table 1. Chemical analysis of the coal provided by the vendor

Overall Analysis		Ash Analysis	
Constituent	Content (wt %)	Equivalent Oxide	Content (wt %)
C	73.9	SiO_2	50.80
S	1.82	Fe_2O_3	16.28
Ash	9.0	Al_2O_3	23.93
Water	0.0	CaO	2.72
		MgO	0.72
		SO_3	1.65
		P_2O_5	0.27
		Na_2O	0.47
		K_2O	1.60
		TiO_2	0.62
		Base/acid[a]	0.29

[a]The base-to-acid ratio is defined as $(Fe_2O_3 + CaO + MgO + Na_2O + K_2O)/(SiO_2 + Al_2O_3 + TiO_2)$.

eroded to an elongated shape after about 300 h of operation, which eventually necessitated nozzle replacement. Finally, the pressure gages on the fuel delivery system failed after about 400 h and had to be replaced. These problems, which were apparently related to the erosive nature of the fine coal particles in the fuel, resulted in several thermal excursions during which the furnace and ceramic tube temperatures dropped rapidly from their steady-state values. These temperature cycles are illustrated in Figs. 5 and 6, which are the respective temperature-time plots for the furnace and ceramic tubes. Both traces exhibit five temperature cycles (designated 1-5). The tubes also experienced an additional temperature deviation (3a) when the burner nozzle was cleaned. In general, the average cooling rates experienced during each temperature cycle were 0.14°C/s (500°C/h) for the furnace and 0.072°C/s (260°C/h) for the tubes. Both values are considerably greater than the desired value of 0.018°C/s (63.4°C/h). In addition, the average tube temperature dropped to as low

as 400°C (Excursion 1). As discussed later, according to examination of the exposed tubes, these thermal cycles could have caused some mechanical damage of the sialon and Al_2O_3 tubes.

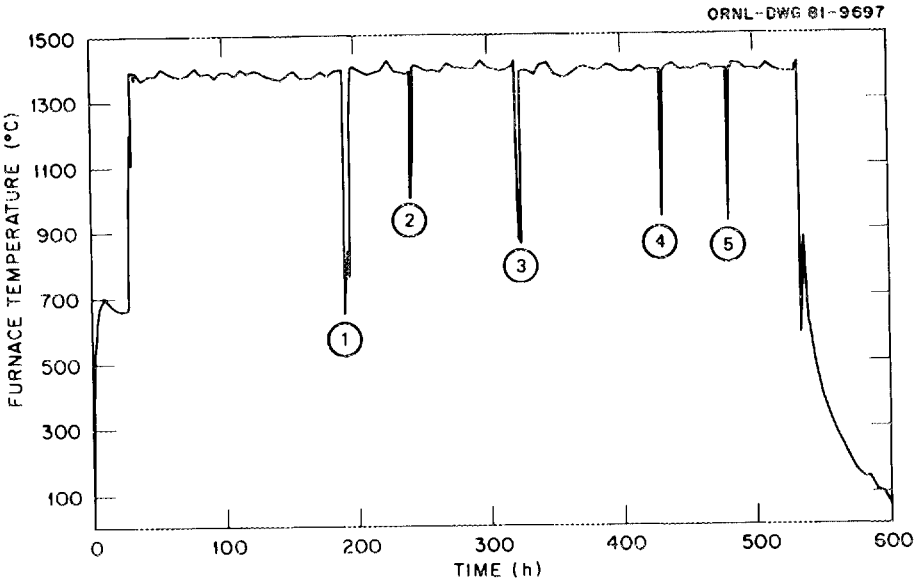

Fig. 5. Furnace temperature versus time showing temperature excursions during CRAF Test 2 exposure.

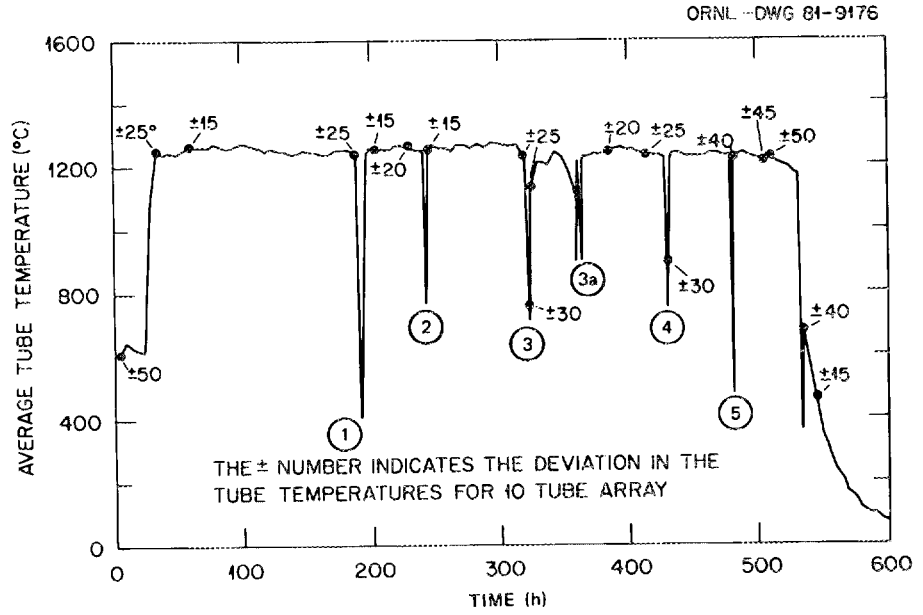

Fig. 6. Average tube temperature versus time showing six thermal cycles experienced by tubes during CRAF Test 2 exposure.

Visual observations of the upstream portion of the ceramic tubes (made through a sightport in the CRAF during the exposure) revealed large amounts of slag buildup on all tubes after about 100 h of exposure. Furthermore, the thickness of the slag on the tubes increased with increasing duration of exposure to the fuel combustion products. This is illustrated in Figs. 7 through 10, which show the upstream side of the tubes at temperature for the respective exposure durations of 50, 120, 260, and 366 h. The slag buildup was apparently not affected by the thermal cycles experienced during the long-term exposure. However, the slag deposit was probably responsible for the increasing spread in tube temperatures that occurred as the exposure time increased. This is shown in Fig. 6. Finally, it should be noted that the slag characteristics were distinctly different from the formations observed during CRAF Test 1, in which only a No. 6 fuel oil was used. In Test 1, only small nodules formed on the upstream side of the silicon carbide tubes and a contiguous hercynite coating formed on the alumina ceramic.

The temperatures of the flue gas entering and leaving the CRAF test sections, the air temperature entering and leaving the tubes, and the air velocity were measured three times during the long-term exposure. The results are summarized in Table 2. Also included are values for the effectiveness of the HX tube array, the heat transfer rate, and the heat flux through the tubes. The actual calculations were based on analyses given elsewhere.[2,3] For example, the effectiveness, ε, was determined from the expression

$$\varepsilon = \frac{T_{2a} - T_{1a}}{T_{1g} - T_{1a}}, \qquad (1)$$

where T_{2a} and T_{1a} are the respective values of the air outlet and inlet temperatures and T_{1g} is the flue gas inlet temperature. This equation, which essentially gives the ratio of the actual heat transfer rate to the maximum possible value dictated by thermodynamics, is based on the assumption that the air provides the minimum product of the mass flow rate and

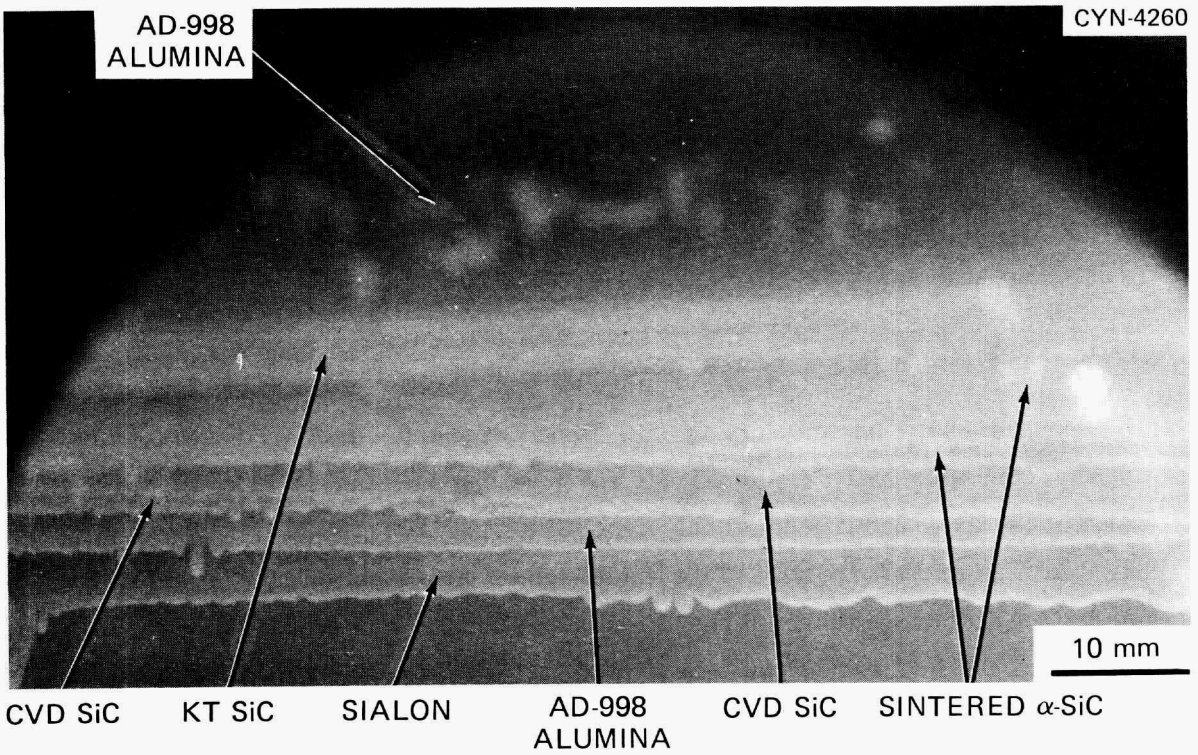

Fig. 7. Upstream side of the ceramic tubes at temperature after 50 h service, showing initiation of slag buildup.

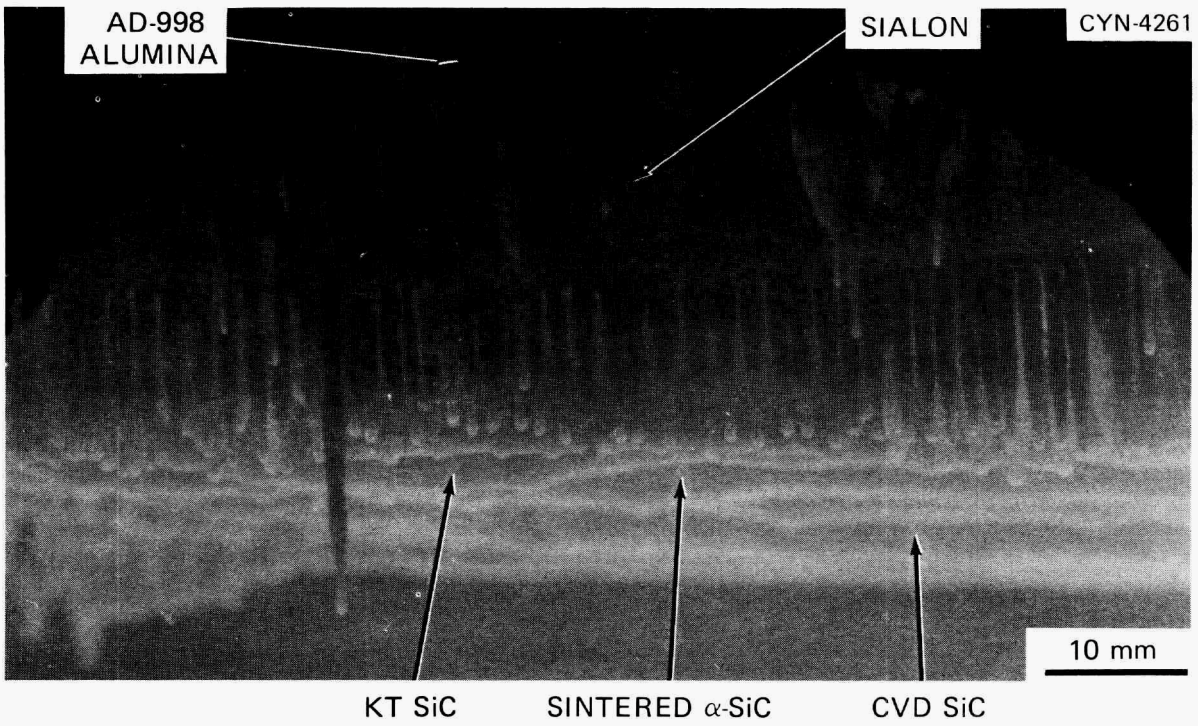

Fig. 8. Upstream side of the ceramic tubes at temperature after 120 h service, showing the formation of needlelike ash deposits on the AD-998 alumina and sialon tubes and massive deposits on other tubes.

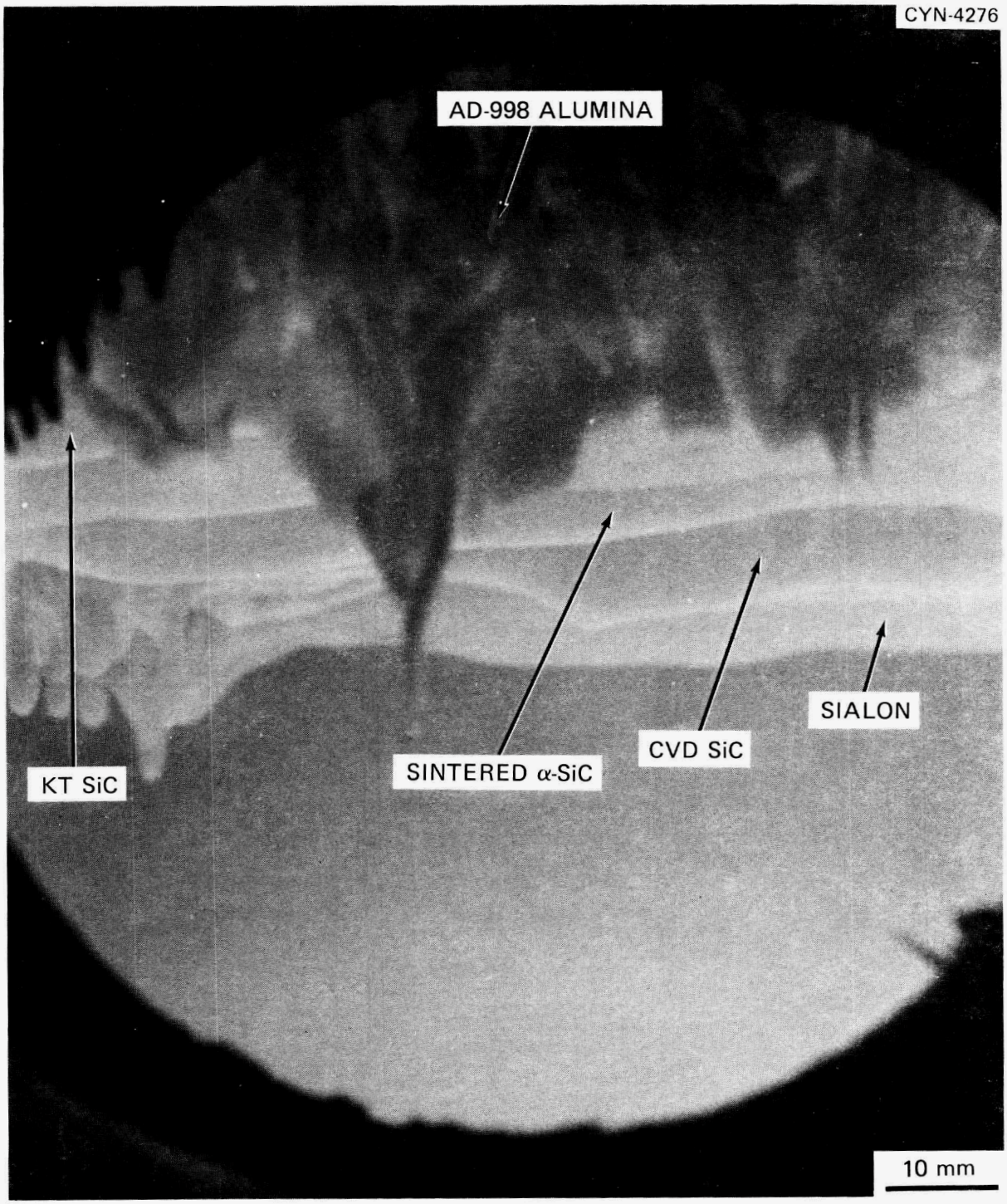

Fig. 9. Upstream side of the ceramic tubes at temperature after 260 h service, showing increasing buildup of slag deposits on the tubes.

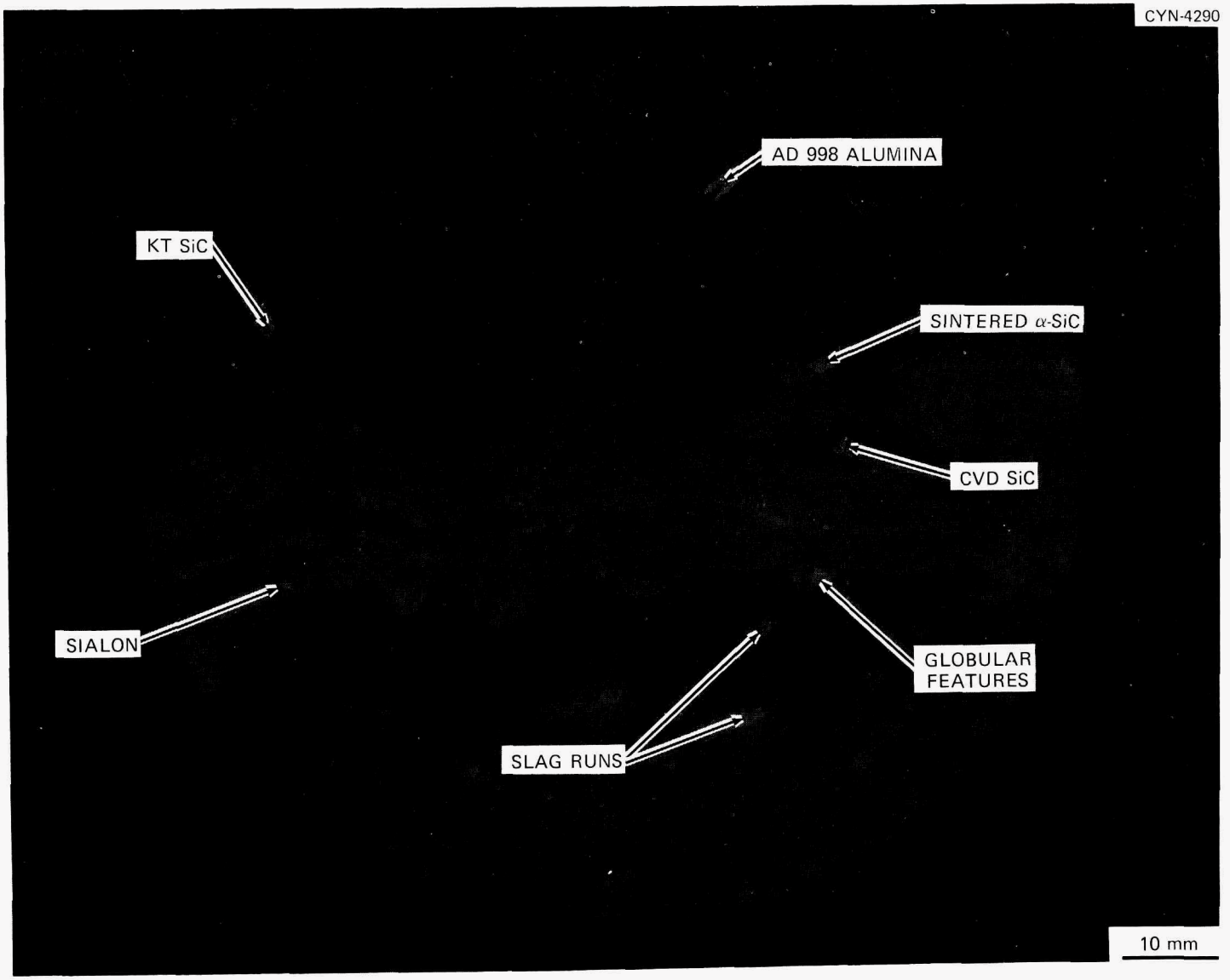

Fig. 10. Upstream side of ceramic tubes at temperature after 366 h service, showing globular features on slag deposits and slag runs on CRAF wall.

Table 2. Calculated values of the heat exchanger effectiveness, heat transfer rate, and heat flux for various exposure times

	Value for each exposure time		
	0.18 Ms (50 h)	1.61 Ms (447 h)	1.68 Ms (466 h)
Flue gas temperature, °C			
Inlet	1,390	1,374	1,352
Outlet	1,349	1,280	1,251
Air temperature, °C			
Inlet	21	21	21
Outlet	427	281	292
Air velocity, m/s	7.6	13.0	12.4
ft/min	1,500	2,560	2,440
Heat exchanger effectiveness	0.30	0.19	0.20
Heat transfer rate, kW	28.9	31.7	31.5
Btu/h	98,660	108,070	107,440
Heat flux, kW/m^2	142.6	156.4	155.4
$Btu/(in.^2 \cdot h)$	314	344	342

specific heat in the system.[2] The heat transfer rate, $\dot{Q}$, was calculated from

$$\dot{Q} = D_a V_a A C_{pa} (T_{2a} - T_{1a}) \ , \qquad (2)$$

where D_a is the air density, V_a is the air velocity, A is the cross-sectional area of the air pipe running from the secondary blower to the air inlet transition of the CRAF, and C_{pa} is the heat capacity of the air. Finally, the heat flux through the tubes was determined by dividing $\dot{Q}$ by the effective surface area of the tubes.

As illustrated in Table 2, the HX effectiveness and thus the heat transfer rate through the tubes dropped substantially as the exposure time increased. It is likely that the slag deposit, which increased in thickness with increasing exposure time, effectively reduced the heat transfer through the tubes. The fact that the actual heat transfer rates increased at the longer exposure times primarily reflects the larger air velocities that were used inside the tubes. Indeed, if these velocities had been constant, the heat transfer rates would have decreased substantially. It should be pointed out that in an actual HX system, increasing the air velocity to maintain a particular heat transfer rate would result in a greater power consumption by the blower or fan system and would thereby affect the economics of the HX.

The results of the chemical analyses of the condensable flue gas samples, which were collected during the measurement of the flue gas inlet temperature, are given in Table 3. The results of an atomic absorption chemical analysis of COM samples taken from the two fuel shipments (designated as COM-1 and -2) are also included in the table. The major metallic impurities (>10 ppm) in the COM fuel were Na, P, V, Ni, Si, Al, K, Mg, and Fe. In addition, 1.09 to 1.11 wt % S was detected. Notice that the concentrations of several of the elements in COM-2 (e.g., Na, Al, Si, K, Ti, V, and Fe) were about half the corresponding values in COM-1. The reasons for these differences are unknown. The major impurities in the flue gas condensables agree fairly well with those in the COM fuel. However, most of the impurities in the condensable matter were present in greater concentrations. Also the concentrations detected for a given element in each of the three flue gas condensable samples showed considerable scatter. Finally, the gas chromatographic analyses of the noncondensable samples (Table 4) revealed major concentrations of O_2 and N_2 with minor amounts of CH_4 and CO_2. No SO_2 or SO_3 was detected.

Table 3. Results of chemical analyses of COM samples and flue gas condensables

Element	Content, wt ppm, in two shipments of coal-oil mixture[a]		Content, wt ppm, in flue gas condensables for three exposure times[b]		
	COM-1	COM-2	50 h	447 h	466 h
B	na	na	40	80	50
Na	53	29	300	1000	500
Mg	18	18	70	500	50
Al	1100	590	70	1000	—
Si	780	450	major	600	major
P	510	90	300	100	300
S	1.11%	1.09%	major	major	major
Cl	na	na	—	<4	—
K	130	75	20	300	>2000
Ca	1.6	1.3	900	300	major
Ti	71	36	2000	40	major
V	31	18	500	50	2000
Cr	2.2	2.1	300	5000	>2000
Mn	1.0	0.8	100	50	600
Fe	690	360	800	500	>2000
Co	0.5	0.5	10	0.5	8
Ni	28	15	200	50	1000
Cu	1.6	1.2	200	50	4
Zn	3.4	2.5	500	80	100
Ga	na	na	—	1	—
Sr	4.3	2.6	20	6	90
Y	na	na	5	<0.1	4
Zr	na	na	6	0.3	3
Ba	3.6	1.7	200	200	260
Pb	3.9	1.7	70	700	100

[a]Atomic absorption chemical analysis by Technical Laboratories, Chattanooga, Tenn. na means not analyzed.

[b]Spark source mass spectroscopy by Analytical Chemistry, ORNL. A dash means that the element was not detected.

Table 4. Gas-chromatographic analysis of noncondensables

Component	Content, vol %, after three exposures[a]		
	50 h	447 h	466 h
O_2	11.6	19.4	19.1
N_2	80.5	76.4	78.2
CH_4	<0.1	<0.1	<0.1
CO	<0.1	<0.1	<0.1
CO_2	6.3	0.75	1.84
SO_2	—	—	—
SO_3	—	—	—
H_2O	<0.1	—	—

[a]A dash means not detected.

Description of Ceramic Materials

Five ceramic materials including KT SiC, α-SiC, CVD SiC, AD 998 Al_2O_3, and a sialon were selected for inclusion in CRAF Test 2. The selection was based on results obtained[1] in CRAF Test 1 and other factors. The KT SiC, which is a siliconized silicon carbide, has received considerable attention previously as a potential HX material.[4,5] Siliconized SiC can be fabricated by one of two techniques. One method involves the formulation of silicon carbide grains combined with silicon and carbon as admixtures. During a high-temperature firing process the silicon and carbon react to form silicon carbide by simultaneous reaction and sintering. In the other method silicon is infiltrated into a prefired SiC and carbon precurser mixture. A second firing converts most of the free silicon and carbon to silicon carbide. The final microstructure consists of the primary silicon carbide phase, a dispersion of smaller secondary SiC grains, a matrix of free silicon, small concentrations of unreacted graphite, and some porosity. The free silicon results in an abrupt mechanical degradation of the material at temperatures above 1250°C as one approaches the

melting point of silicon (1410°C). In addition, metallic impurities in the service environment can combine with the silicon to form low-melting eutectics, which can extrude out of the body.

The α-SiC is a dense, single-phase material, which has better mechanical properties than the siliconized SiC. It is prepared by sintering very fine-grained (<1 μm) silicon carbide using a relatively small amount of sintering aids including about 0.5 wt % B and 0.5 wt % C. These dopants, which are required for full densification, also reduce oxidation and corrosion resistance of the bulk material.

Chemically vapor deposited (CVD) silicon carbide is typically a theoretically dense material that is impervious to gases and characterized by a high mechanical strength when the material is fabricated into small shapes. Its fabrication requires use of gas mixtures such as methyltrichlorosilane (MTS or CH_3-$SiCl_3$), hydrogen, and an inert gas and the subsequent deposition of SiC onto a porous graphite or silicon carbide substrate at high temperatures. Generally only small shapes of pure CVD SiC (up to a few millimeters) can be produced from this process. Although larger deposits are possible, they often contain process-induced delaminations or cracks due to SiC grain growth, which degrade the resulting properties.

The AD 998 aluminum oxide is a fully dense, fine-grained material, which as fabricated contains minor amounts of silicate glass. Although this ceramic has a lower thermal conductivity and lower thermal shock resistance than the silicon carbides, its chemical stability, fabrication technology, and potentially low cost are attractive characteristics for HX applications involving fossil fuel combustion environments.

The final material exposed in CRAF Test 2 and subsequently analyzed was the relatively new sialon material. In general, the term sialon is used to identify a broad range of compositions existing within the silicon-aluminum-oxygen-nitrogen system. However most commercial sialon materials of interest are based on the β′-sialon formulation, in which the major phase is a solid solution involving Al_2O_3 and Si_3N_4.[6,7] This solid solution, which can be based on an expanded β-Si_3N_4 structure, has a range of compositions given by $Si_{3-x}Al_xO_xN_{4-x}$. The reported properties that make the β′-sialon a prospective HX material include low thermal

expansion, good thermal shock resistance, moderate high-temperature strength, and good oxidation resistance. In addition, it can be fabricated into dense shapes by conventional sintering techniques as long as a liquid phase is present at the sintering temperature. This can be accomplished by using formulations within the system Si_3N_4-SiO_2-Al_2O_3-AlN since these result in the presence of a liquid phase in equilibrium with the β′-sialon at temperatures above 1700°C. Alternately, additions of metal oxides such as MgO to the β′ composition can react with the β′ constituents to form a liquid phase at the firing temperature. However, since these liquids can degrade the properties of the ceramic, their presence must be minimized during the final stages of the densification process.

A GE 128 sialon having an initial starting compositon of approximately 64 wt % Si_3N_4, 26 wt % Al_2O_3, 8.5 wt % AlN, 0.9 wt % SiO_2, and 0.6 wt % MgO was chosen for exposure in CRAF Test 2. The microstructure of this material reportedly consists primarily of the β′-sialon composition with minor amounts of porosity.[6] This porosity significantly limits the room-temperature four-point bend strength to about 320 MPa (47 ksi). However, considerable variations in these properties and characteristics can result from minor changes in processing techniques.

Two tubes of each of the five ceramic materials were exposed to the combustion products of the COM fuel in CRAF Test 2. The pretest dimensions of each tube (Table 5) varied considerably. Normally, we would have preferred tubes of equivalent dimensions, but for materials such as sialon and KT SiC specifying specific dimensions would have resulted in excessive delivery times.

Characterization of the Tubular Materials

The physical and mechanical properties of the five types of structural ceramic materials used in CRAF Test 2 are given in Table 6 and the compositions in Table 7. The data on the silicon carbide and alumina ceramics were obtained from the vendors, and the data for the sialon were determined from published reports[6,7] describing the development of sialon materials. Since these properties were measured on generic materials made specifically for small-scale laboratory tests, they were not necessarily

Table 5. Dimensions, materials, and sources of ceramic tubes exposed in CRAF Test 2

Designation	Dimensions, mm			Material	Source
	Length	OD	ID		
KT-1	305.4	25.9	13.2	Siliconized SiC	Carborundum Co., Niagara Falls, N.Y.
KT-2	304.8	26.0	13.4	Siliconized SiC	Carborundum Co., Niagara Falls, N.Y.
Sintered Alpha-1	304.4	25.2	18.8	Pressureless sintered SiC	Carborundum Co., Niagara Falls, N.Y.
Sintered Alpha-2	304.8	25.3	18.8	Pressureless sintered SiC	Carborundum Co., Niagara Falls, N.Y.
CVD-1	306.0	23.6	19.1	Chemically vapor-deposited SiC	Deposits and Composites, Herndon, Va.
CVD-2	292.3	23.2	19.2	Chemically vapor-deposited SiC	Deposits and Composites, Herndon, Va.
AD 998-1	280.8	25.3	18.9	High-purity alumina	Coors Porcelain Co., Golden, Colo.
AD 998-2	279.8	25.4	18.9	High-purity alumina	Coors Porcelain Co., Golden, Colo.
Sialon-1	225.4	23.5	18.0	β′ Sialon	General Electric Co., Philadelphia
Sialon-2	223.8	23.5	18.1	β′ Sialon	General Electric Co., Philadelphia

Table 6. Vendor-supplied physical and mechanical properties of the ceramic materials used in CRAF Test 2

Property	Value for each material				
	KT SiC	α-SiC	CVD SiC	AD 998 Al_2O_3	GE 128 Sialon
Density, Mg/m^3	3.1	3.1	3.21	3.82	2.91
Modulus of Elasticity, GPa					
25°C	386	410	490	345	243
1000°C		375			
1200°C	352				
Strength, MPa					
Tensile at 25°C	142		314		
Compressive at 25°C	1034			2206	
Flexural at 25°C	304		690	186	300
1000°C				151	
1200°C	157	482			250
1300°C					160
Linear Thermal Expansion, $°C^{-1} \times 10^{-6}$					
25–1000°C	4.68	4.80		8.0	3.1
Thermal Conductivity, W/(m·K)					
25°C				29.4	
200°C		112		23.0	
1200°C	28	40			

Table 7. Chemical composition of the ceramic materials used in CRAF Test 2

Constituent	Content, wt %, in each material				
	KT SiC	α-SiC	CVD SiC	AD 998 Al_2O_3	GE 128 Sialon
SiC	90	100	100		
Free Si	10				
Al_2O_3				99.8	26.0
Si_3N_4					64.0
SiO_2				0.07	0.9
AlN					8.3
Fe_2O_3				0.025	
CaO				0.030	0.1
MgO				0.050	0.6
Other				0.025	

representative of the bulk tubular materials employed in this experimental exposure. Furthermore, many differences were found when data from Table 6 were compared with property values from the literature.[4,6–9] For these reasons, both the as-received and exposed tubes were extensively characterized by the techniques outlined in Table 8. The visual examinations and dimensional measurements provided an indication of bulk changes in the ceramic materials resulting from the long-term exposure to the COM fuel. The radiographic examinations, microstructural characterization, x-ray diffraction, and microcomposition analyses were used to detect physical and chemical changes in the five materials that could adversely affect their performance as structural HXs. The details of the procedures and sample preparations required for these techniques are well established and therefore not repeated here. Finally, the characterization also involved determination of as-received and postexposure values of the helium permeability, thermal expansion, and fracture strength. The measurement of these properties, which constitute critical factors in the design of structural ceramic HXs,[2] is discussed in more detail in the following text.

Table 8. Analyses used to characterize the structural materials

Visual examination
Dimensional measurements
Radiographic nondestructive examination
Helium permeability
Microstructural characterization
Scanning electron microscopy
Optical microscopy (metallography)
X-ray diffraction
Microcomposition
Wet chemical analysis
Spark-source mass spectroscopy
Induction-coupled plasma spectroscopy
Fast-neutron activation analysis
Energy-dispersive x-ray analysis
Thermal expansion
Mechanical strength

In many high-temperature HX designs, helium or another gas is used in large volume at high pressure as a working fluid on the secondary side. Leakage, which can occur by physical permeation through the bulk material, cracks, or leaking joints, can seriously reduce the effectiveness of the HX. We measured the room-temperature helium permeability through the tubular materials using a Veeco* helium leak detector (Model MS AB) calibrated with a standard leak rate source. Descriptions of the associated test fixture and measurement procedure are given in an earlier publication.[1] The helium leak rate was determined for both the as-received and surviving exposed tubes with successive pressure differentials of 101, 274, 446, and 618 kPa (14.6, 39.7, 64.7, and 89.6 psi)

*Product of Veeco Instruments, Inc., Plainview, N.Y.

maintained across the tube wall. The gas permeability, K, which is analogous to the thermal conductivity, was also determined for each tube by using the formula

$$K = \frac{\nu \dot{V} \ln(r_o/r_i)}{2\pi L \Delta P} , \tag{3}$$

where

K = permeability, m^2,
ν = viscosity of the gas, Pa·s,
$\dot{V}$ = helium leak rate, m^3/s,
ΔP = absolute pressure drop across the sample, Pa,
r_o = outer radius of the tube,
r_i = inner radius of the tube, and
L = length of the tube, m.

The helium leak rate determined as a function of temperature would have been desirable since the permeability of gases through dense ceramic materials usually varies exponentially with temperature. However, the low-temperature capabilty of the epoxy adhesive that was used to attach the necessary fixturing to the tube ends made high-temperature permeability measurements impractical.

The thermal expansion of tubular ceramic materials is generally believed to be one of the most important thermophysical properties controlling the thermal stress and thermal shock resistance of ceramic HX structures.[1] Changes in the thermal expansion of ceramic recuperator tubes resulting from the exposure to fossil fuel combustion products can lead to cracking or fracture of the tubes. Therefore, the characterization techniques used in CRAF Test 2 included measurements of the thermal expansion of approximately 25-mm-long specimens machined from the as-received and exposed tubes. In the latter case, samples from both the upstream and downstream portions of each tube were analyzed. All expansion

measurements were made from room temperature to 1200°C in air with a high-temperature dilatometer* calibrated with a high-purity recrystallized alumina standard.

The mechanical strength of the materials is another critical property required for the design of HXs. Our use of more conventional bar-type samples from the tubes for the strength determination would have involved complicated machining techniques, which might have altered the intrinsic characteristics of the surface flaws along the tube. Alteration of the surface flaw population could have a major effect on the measured fracture strengths. Therefore, a C-ring diametral compression test[10,11] [Fig. 11(a)] was employed in the strength characterization of the as-received and exposed tubes. The main advantage of this technique, which provided adequate results in a previous study,[1] is that fracture is initiated along the outside surface of the C-ring sample, where the tensile stresses are highest [Fig. 11(b)]. In CRAF Test 2 this outer surface area was most subject to strength variations resulting from the 496-h exposure to the combustion products of the COM fuel. Consequently, the results of the C-ring compression tests of the as-received and exposed samples were expected to provide a good indication of the relative change in strength due to reactions between the tubular specimens and the constituents in the fuel combustion gases. In the case of the nonoxide ceramics, strength variations could also result from oxidation of the materials at the exposure temperature.

Each C-ring specimen with a cross-sectional thickness of 6.6 mm was loaded to failure at room temperature in air with an Instron† machine operating at a crosshead speed of 8.5 μm/s (0.020 in./min). The exposed samples were oriented such that fracture occurred in the upstream region

*Harrop thermal dilatometric analyzer, model TD-716, product of Harrop Laboratory, Columbus, Ohio.

†Product of Instron Corporation, Canton, Mass.

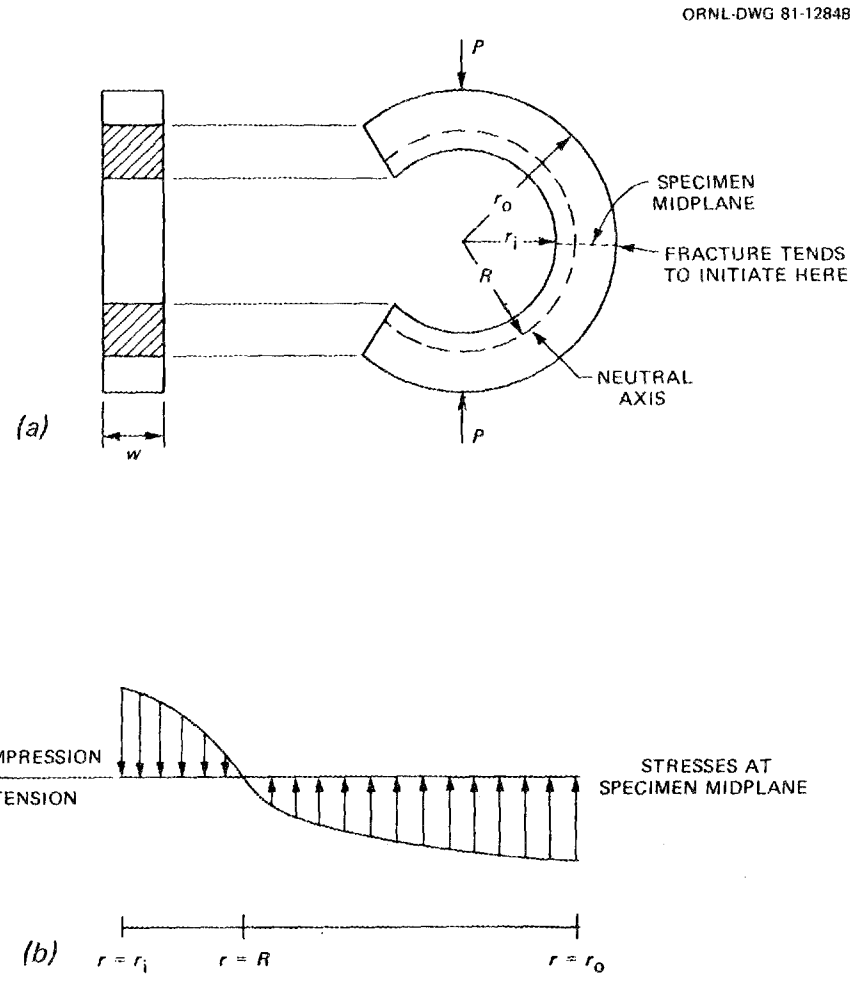

Fig. 11. C-ring specimen geometry, showing the stress distribution resulting from the application of a compressive load.

of the original tube. The fracture stress, σ, was calculated from the expression,

$$\sigma = \frac{P}{(r_o - r_i)w}\left[1 + \left(\frac{r_o + r_i}{2r_o}\right)\left(\frac{R - r_o}{\bar{r} - R}\right)\right] , \qquad (4)$$

where P is the breaking force (negative for compressive loading), $\bar{r} = (r_o + r_i)/2$, and $R = (r_o - r_i)/\ln(r_o/r_i)$. The parameters w, r_o, and r_i are defined in Fig. 11(a). Although it would have been desirable to

determine the strength characteristics of the tubular materials at high temperatures in either air or the flue gas combustion environment, equipment limitations made such measurement impractical.

It should be noted that visual examinations, dimensional measurements, radiographic examinations, and helium permeability measurements were made on the actual tubes used in CRAF Test 2 both before and after the 496-h exposure. However, the determination of the microstructural, x-ray diffraction, microcompositional, thermal expansion, and mechanical strength characteristics of the five as-received materials required the use of representative archive tubular samples. The detailed sectioning plans for these pretest analyses are outlined in Fig. 12. One exposed tube of each ceramic material was sectioned into C-ring and thermal expansion specimens (Fig. 13), and the other tube was used in the fabrication of x-ray diffraction, microcompositional, scanning electron microscopy, and metallographic samples (Fig. 14). These last four analyses were also used to characterize the coal slag deposits remaining on the exposed tubes. Finally, it should be noted that no exposed analytical specimens were fabricated from portions of the tube near the air inlet end, since the reaction between the slag and ceramic was generally negligible in these regions.

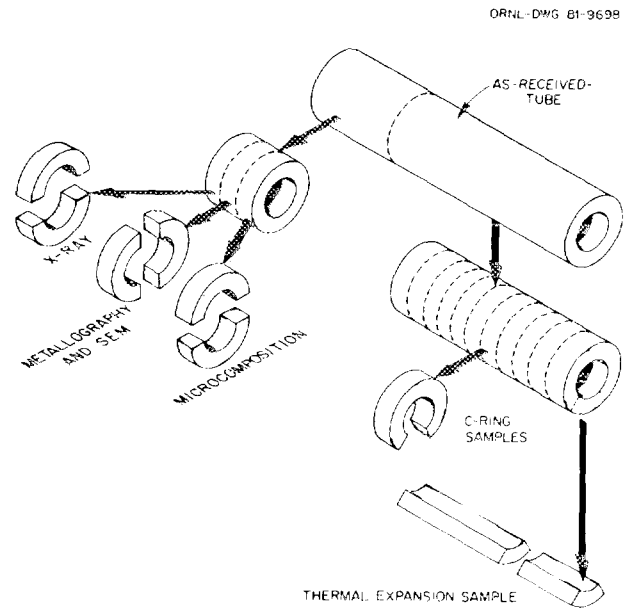

Fig. 12. Typical sampling plans for pretest characterization of ceramic tubes in CRAF Test 2.

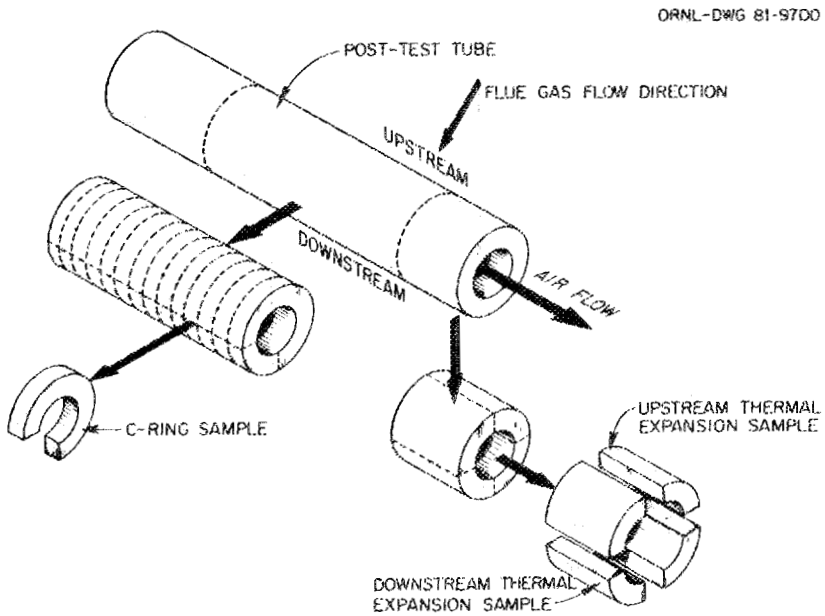

Fig. 13. Sectioning plans for C-ring and thermal expansion samples from exposed tubes.

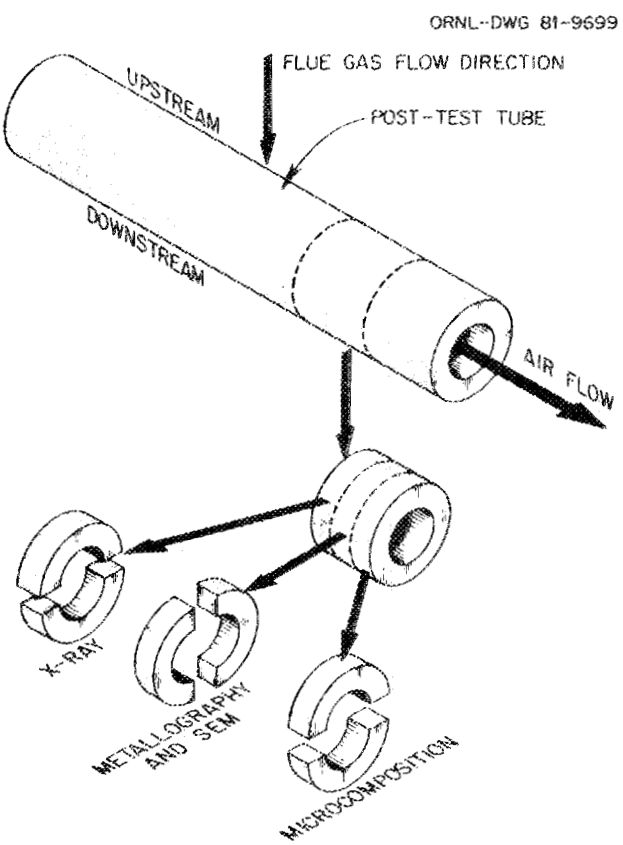

Fig. 14. Sectioning plans for x-ray, metallographic, scanning electron microscopy, and microcompositional samples from exposed tubes.

RESULTS AND DISCUSSION

Views of the upstream and downstream regions of the ten-tube array before starting CRAF Test 2 were shown previously in Fig. 3. Fuel slag deposits on the upstream side of the ceramic tubes were observed as small localized spots when viewed through the viewport at about 30 h. They increased in size and exhibited more structure at 50 h as shown in Fig. 7. The structure and amount of the fuel slag depositing on the tubes as a function of time were much different from those observed previously in CRAF Test 1, in which only No. 6 residual oil was burned. As will be shown subsequently, this difference was attributable to combustion of coal in Test 2. There was evidence that the fuel slag deposited on the tubes during this experiment was primarily derived from the coal ash in the COM fuel. This observation verified an earlier assumption that use of COM fuel in the CRAF combustor was a convenient method for burning coal in the unit, and that the use of No. 6 oil as a coal carrier had a minimal effect on the fuel slag composition or the reactions between the fuel slag and the five ceramic materials. The use of COM fuel for ceramic material exposures at high temperatures was therefore judged to be a suitable simulation of direct coal combustion for studying effects of coal slag on the properties and structure of the materials.

As combustion time increased to 120 h, the coal slag deposits on the tubular ceramic specimens attained a stringerlike character, as shown in Fig. 8. The deposits became larger and attained a more rounded appearance by 260 h, as shown in Fig. 9. The air flow direction through the tubes in all these figures is left to right. The effects of lower tube wall temperatures at the air inlet end are apparent in Fig. 9, where the globular slaglike features are visible on the left side of the view. The large slag deposit visible near the viewport is attributed to introduction of air into the duct to cool the window. This air reduced the local gas temperature and increased the oxygen content of the combustion gas. These two events would increase deposition of slag from the hot gas and increase the slag viscosity. The slag deposits on the upstream side of the ceramic tube surfaces beyond the first 2 to 3 cm from the air inlet end had a relatively smooth surface, as shown in Fig. 9. At 366 h, some globular

features were visible on the tube deposits, as shown in Fig. 10. The large slag growth near the viewport window is also visible but out of focus in the foreground of this figure. Coal slag runs on the CRAF walls also are clearly visible in Fig. 10. These resulted from the hot slag condensing on the refractory walls above the tubes and then running downward along the walls. At about this time in the combustion run, significant back pressure in the furnace became noticeable. The morphology of the slag deposits remained essentially the same, as observed through the viewport, from about 350 h of combustion until completion of the exposure at 496 h.

After CRAF Test 2 was completed, the top transition section containing the flue gas outlet port was removed and the CRAF disassembled. The upstream (lower) side of the ten-tube array contained a thick deposit of coal slag, but the downstream (upper) side of the tubes contained relatively thin slag deposits. The upstream (lower) side of the tube array while still in place in the CRAF is shown in Fig. 15. The walls of the CRAF duct below the tube row contained essentially no coal slag. Slag has deposited extensively at the tubes and on all wall surfaces of the duct above the tubes. This observation suggests that the coal ash constituents could not condense at the combustion gas temperature present below the tubes. Slag deposition at the tubes was due to the decrease in gas temperature by heat extraction by the tubes and/or due to changes in flow streamlines in the vicinity of the tubes. The decrease in gas temperature was apparently the major cause of slag deposition because the metal probe tube that originially projected perpendicularly into the gas stream just below the tubes (visible in Fig. 15) contained essentially no slag deposit. If gas flow disturbance was a major cause of slag deposition, rather than the gas temperature, this metal probe tube, which underwent significant corrosion and deformation, would have contained slag.

The downstream (upper) side of the tube row after removal of the top section of the CRAF is shown in Fig. 16. Note that the spaces between the tubes are nearly filled with solidified slag. Slag deposition on the downstream surface of the tubes was minimal, so the thermocouple protection tubes are still readily discernible.

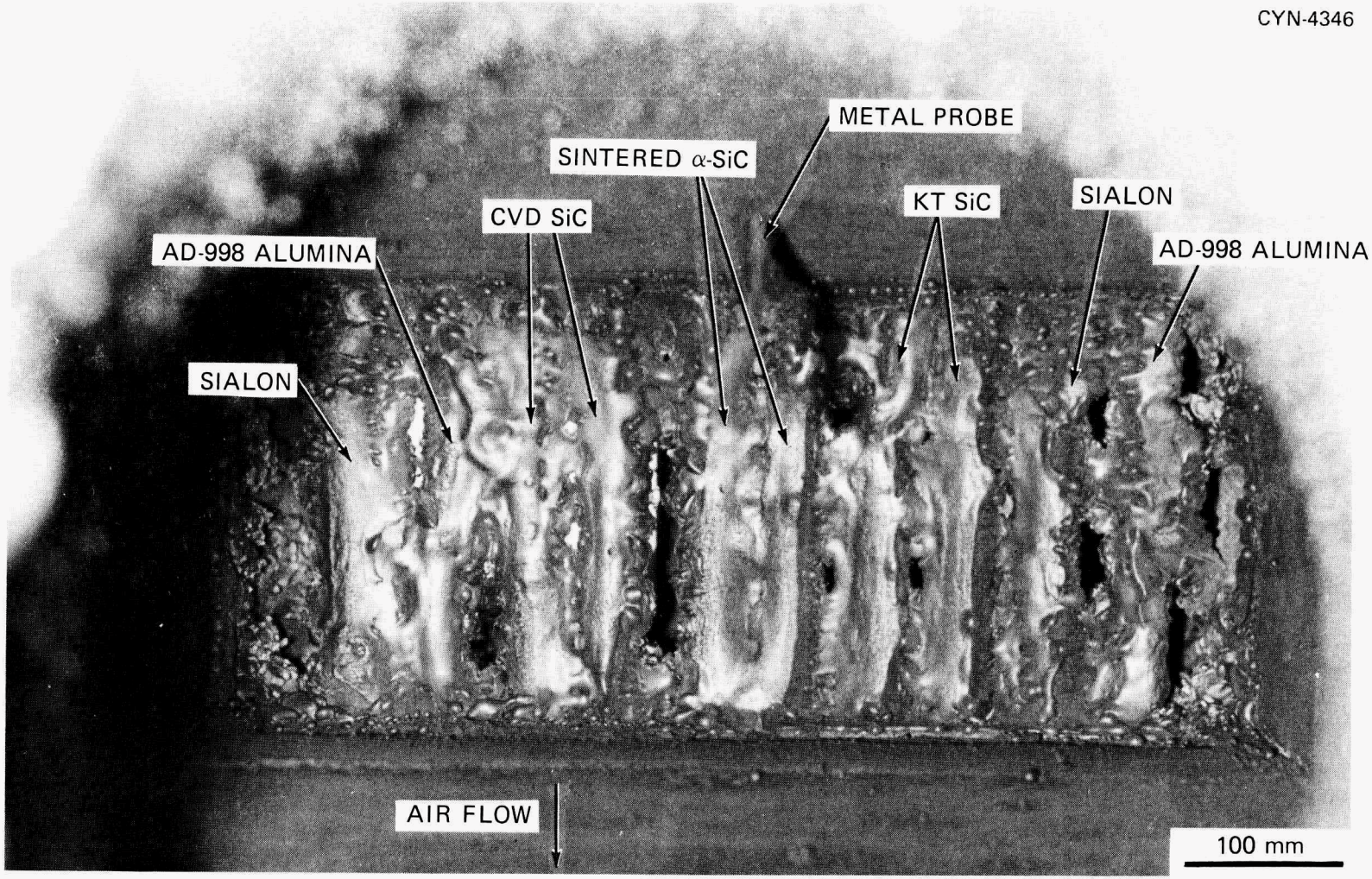

Fig. 15. Exposed tube array showing extreme slag buildup or upstream surface of ceramic tubes after the long-term exposure.

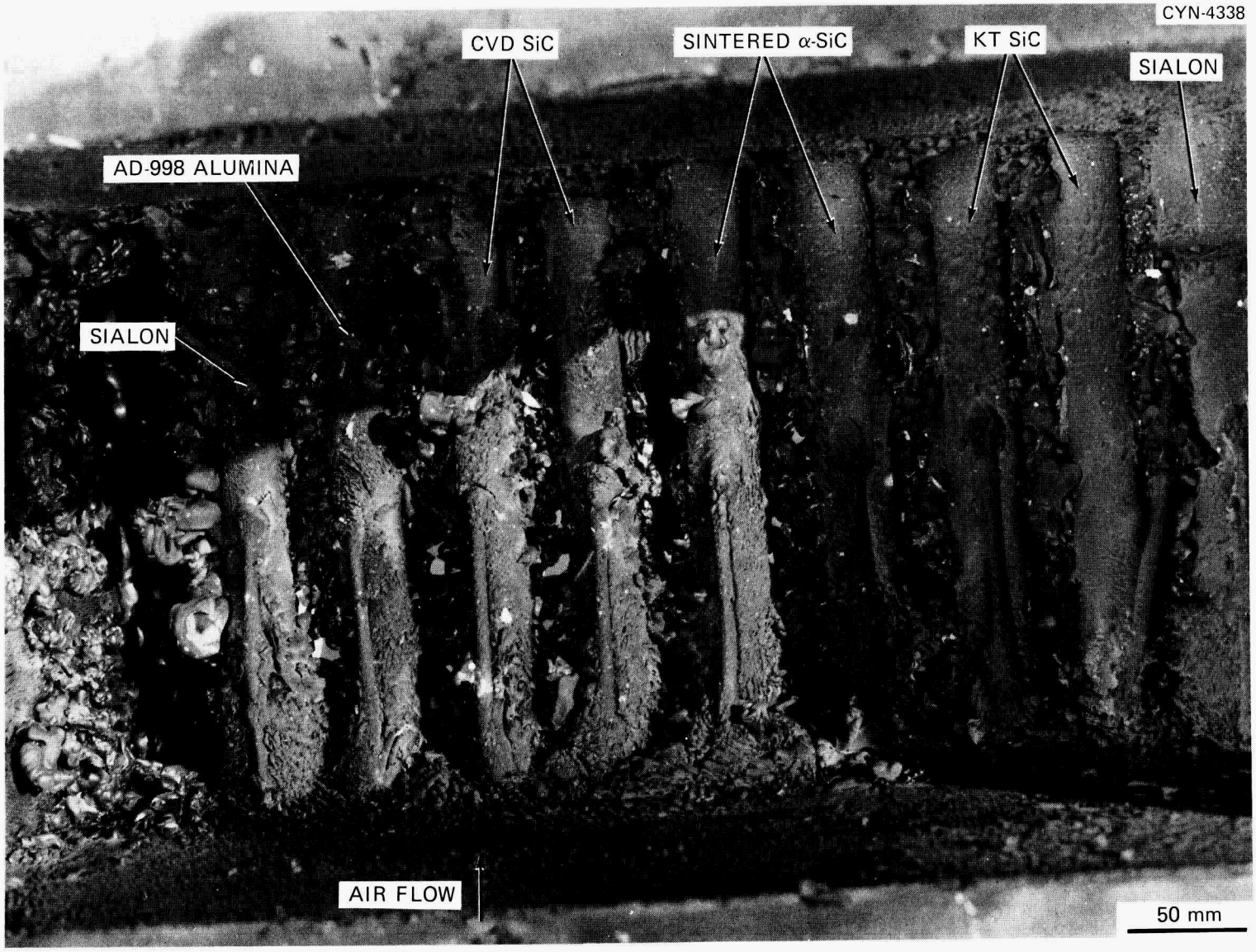

Fig. 16. Condition of downstream surface of ceramic tubes after the long-term exposure.

After CRAF disassembly, the ceramic tubes and their adherent slag were removed from the facility along with the refractory header blocks. The upstream (lower) side of the tube row is shown in Fig. 17. The slag surface that faced impinging combustion gas was relatively smooth and brown. The clean tube ends in Fig. 17 indicate where the tubes protruded into holes in the header blocks, which had been removed. The two tubes having the larger diameters are short KT SiC collars, which had to be used as extension tubes with the shorter GE 128 sialon materials. The large crack in the slag in Fig. 17 developed during header block removal. The coal slag joining the ten tubes was carefully fractured in the region between the tubes to separate the specimens from each other for analyses. This was accomplished without difficulty since the slag in this region was relatively thin. Each tube was then examined macroscopically. The helium permeability of the surviving exposed tubes was also measured. The tubes were then sectioned into samples for determination of C-ring fracture strength, thermal expansion, microcomposition, and chemical composition. The results of these various analyses are presented and discussed in the remainder of this report.

Macroscopic Examinations of Individual Tubes

After the 496-h exposure, all tubes were completely covered with a coal slag, which ranged in color from dark brown to black. The thickness of the coal slag ranged from 38 to 76 mm on the upstream surface and 3 to 13 mm on the downstream surface. The nature of this buildup, which was similar on all tubes, is illustrated for the Al_2O_3 tube by the upstream, downstream, side, and cross-sectional views shown in Figs. 18 through 21, respectively. The side view (Fig. 20) shows that the final morphology of the upstream coal slag depended on its horizontal position along the tube. For example, the slag structure near the air inlet end was characterized by columnar growth directed upstream from the tubular surface. However, as the air outlet side was approached, this columnar growth was completely eliminated, so that the surface contour of the slag was considerably more uniform. One explanation for this variation in the slag morphology is that, during the 496-h exposure, introduction of air

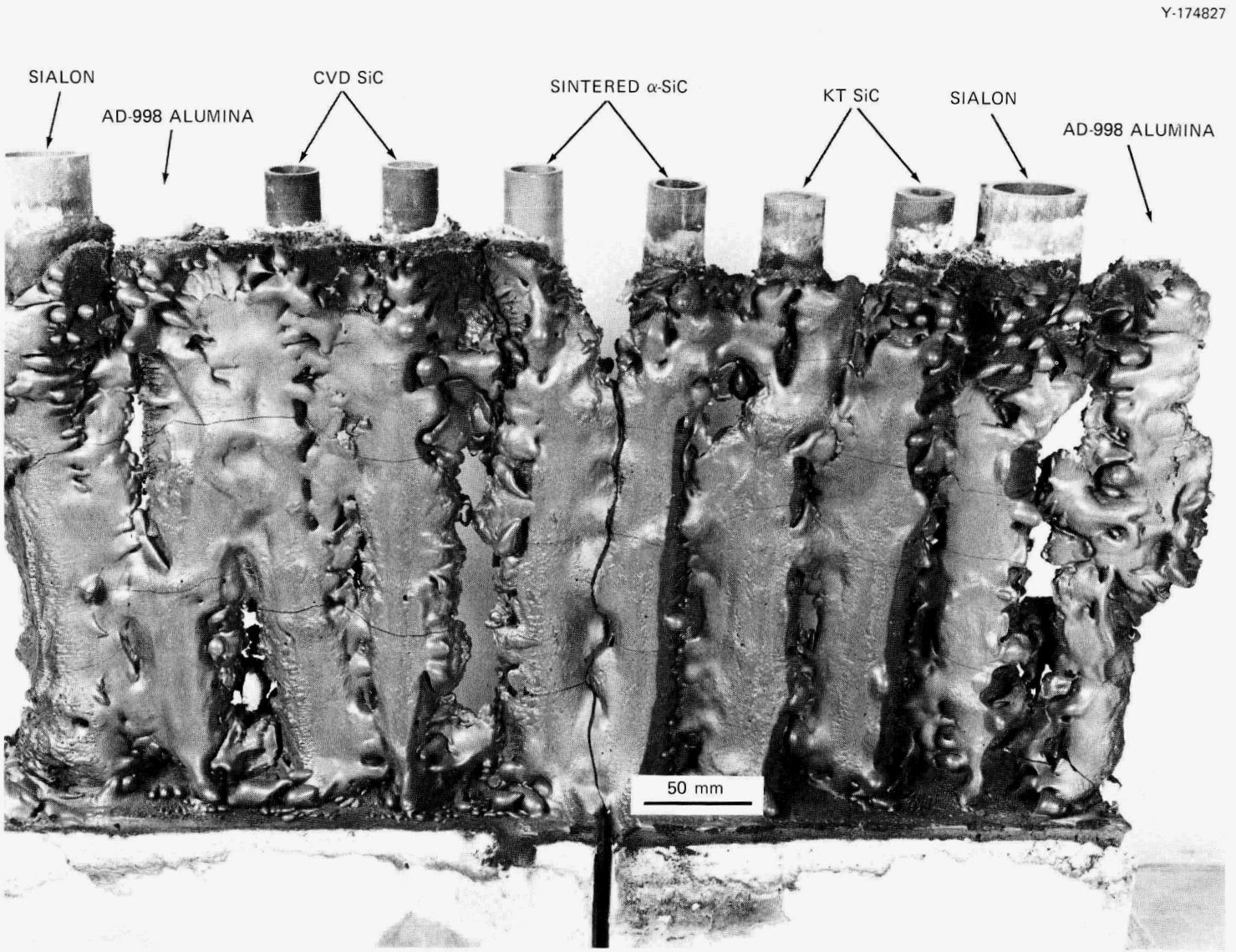

Fig. 17. Upstream surface of exposed ceramic tubes after removal from CRAF unit. (One header block has also been removed.)

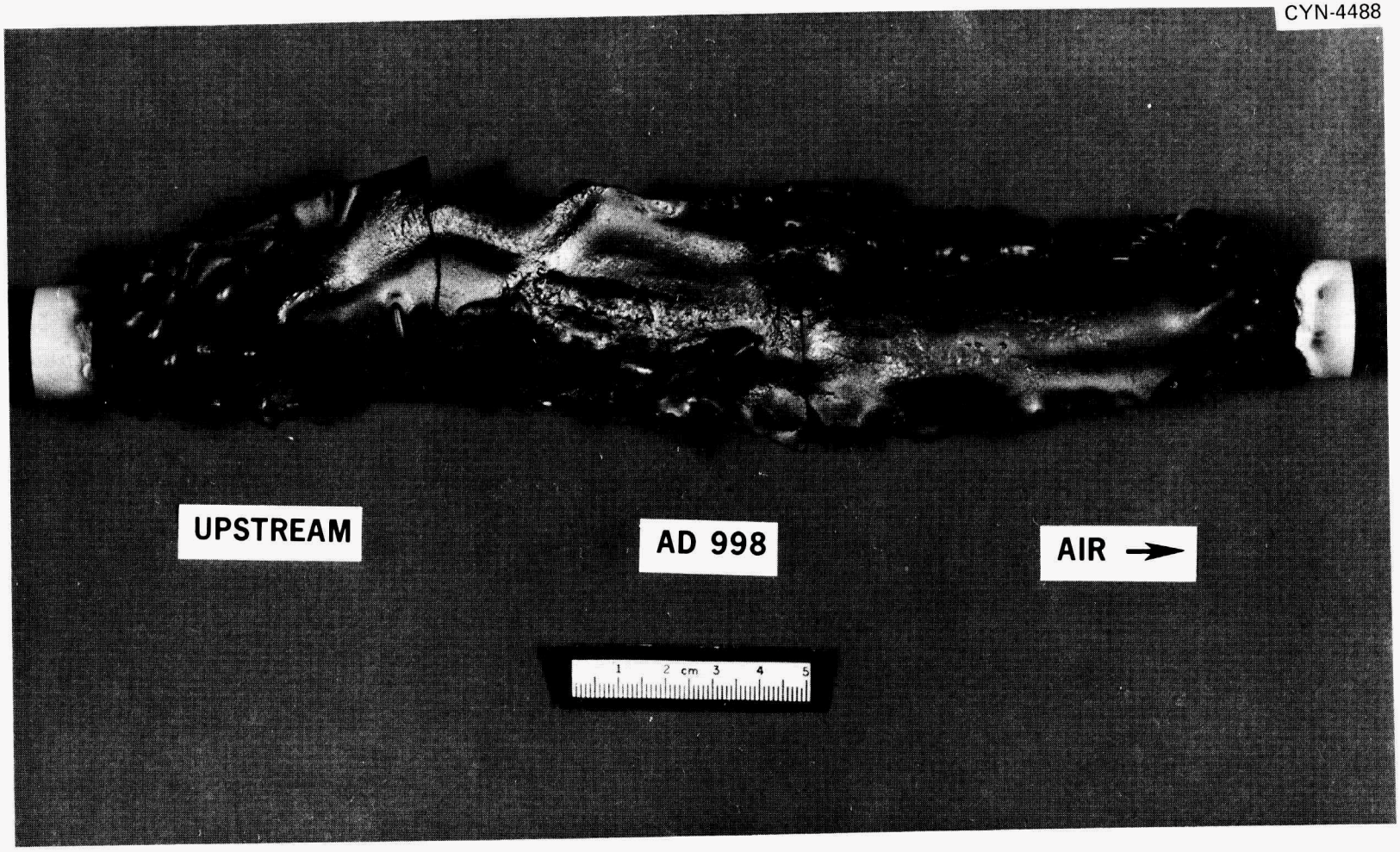

Fig. 18. Upstream view of exposed AD-998 Al_2O_3 tube.

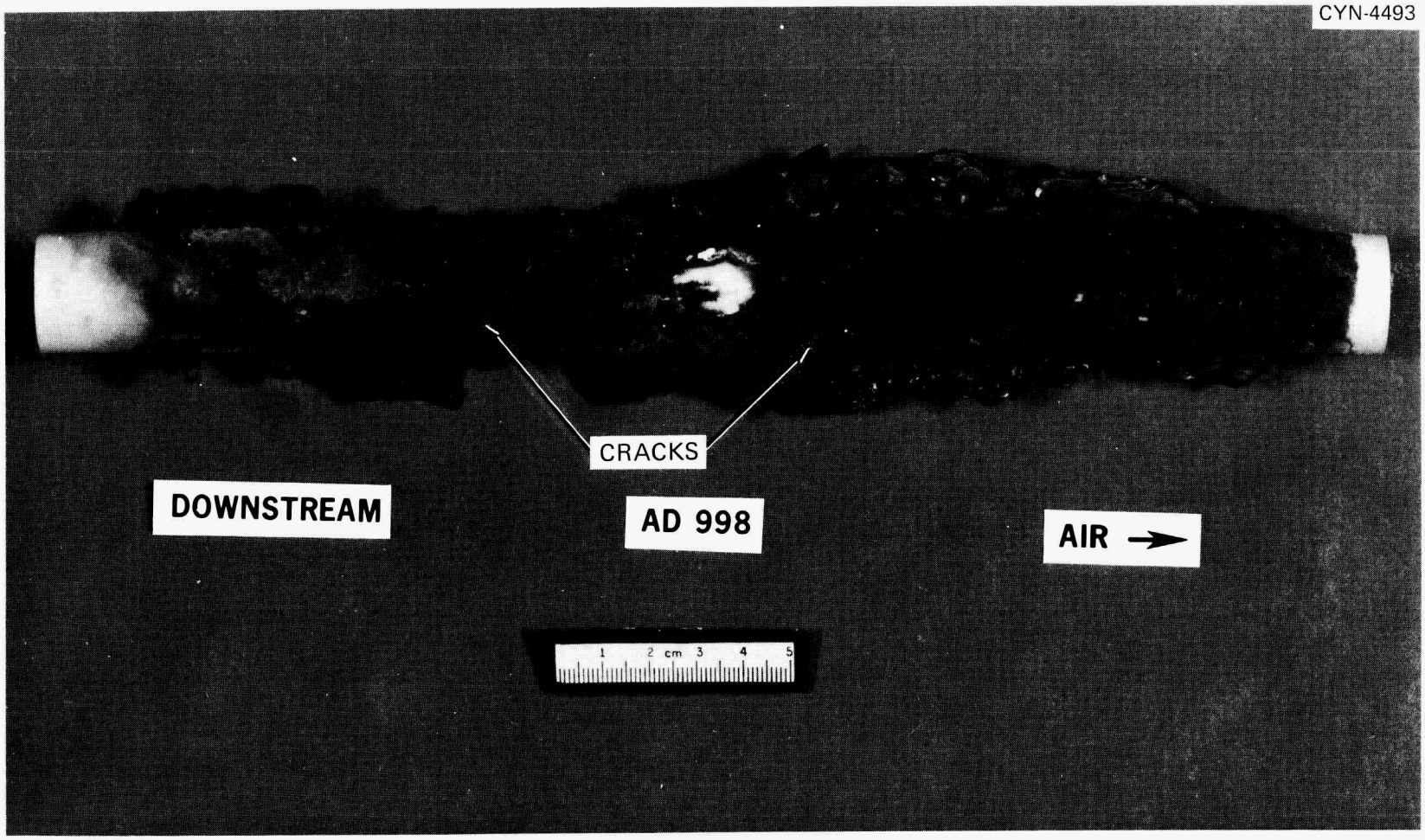

Fig. 19. Downstream view of exposed AD-998 Al_2O_3 tube, showing location of cracks.

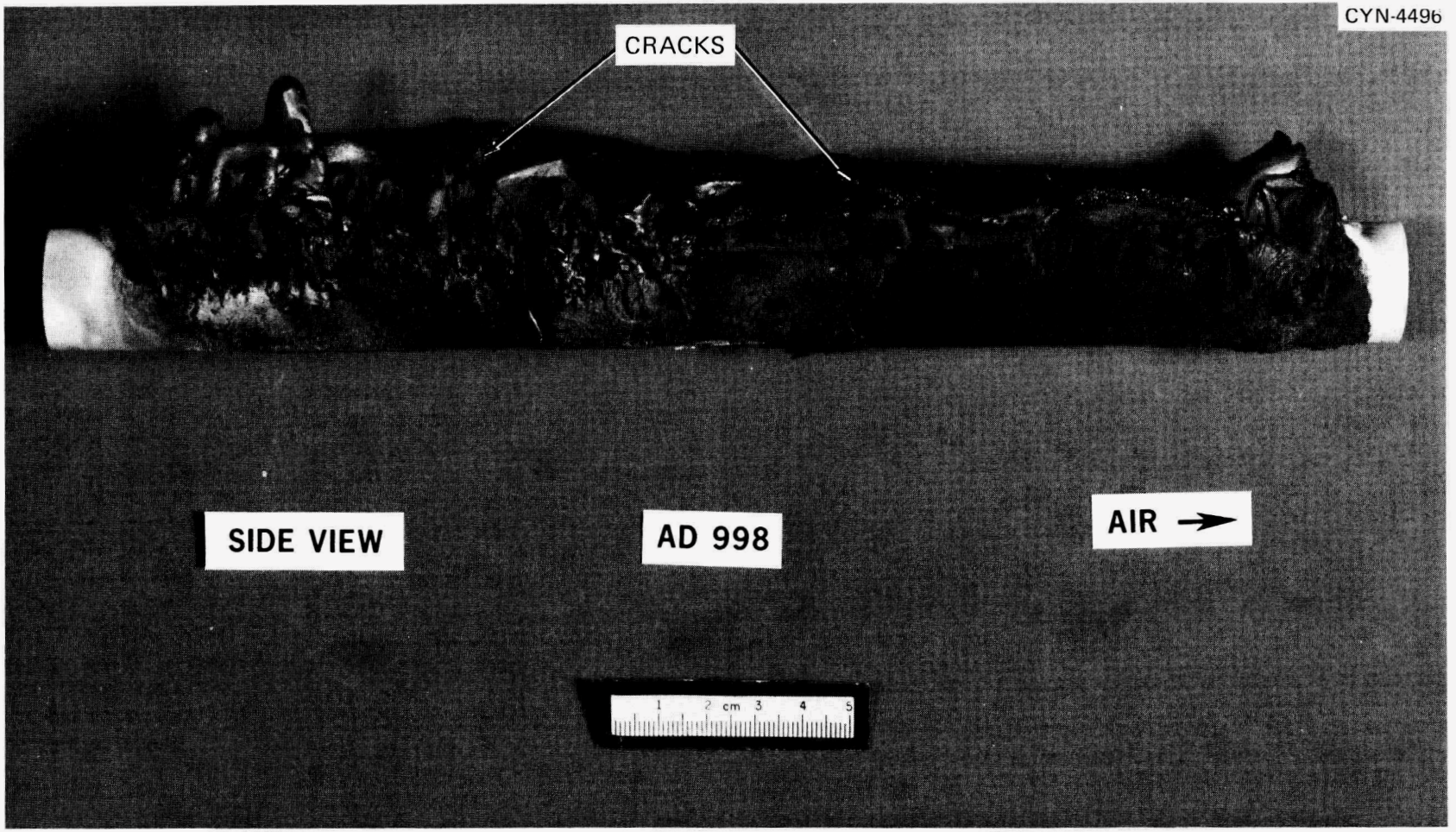

Fig. 20. Side view of exposed AD-998 Al_2O_3 tube, illustrating the extensive cracking.

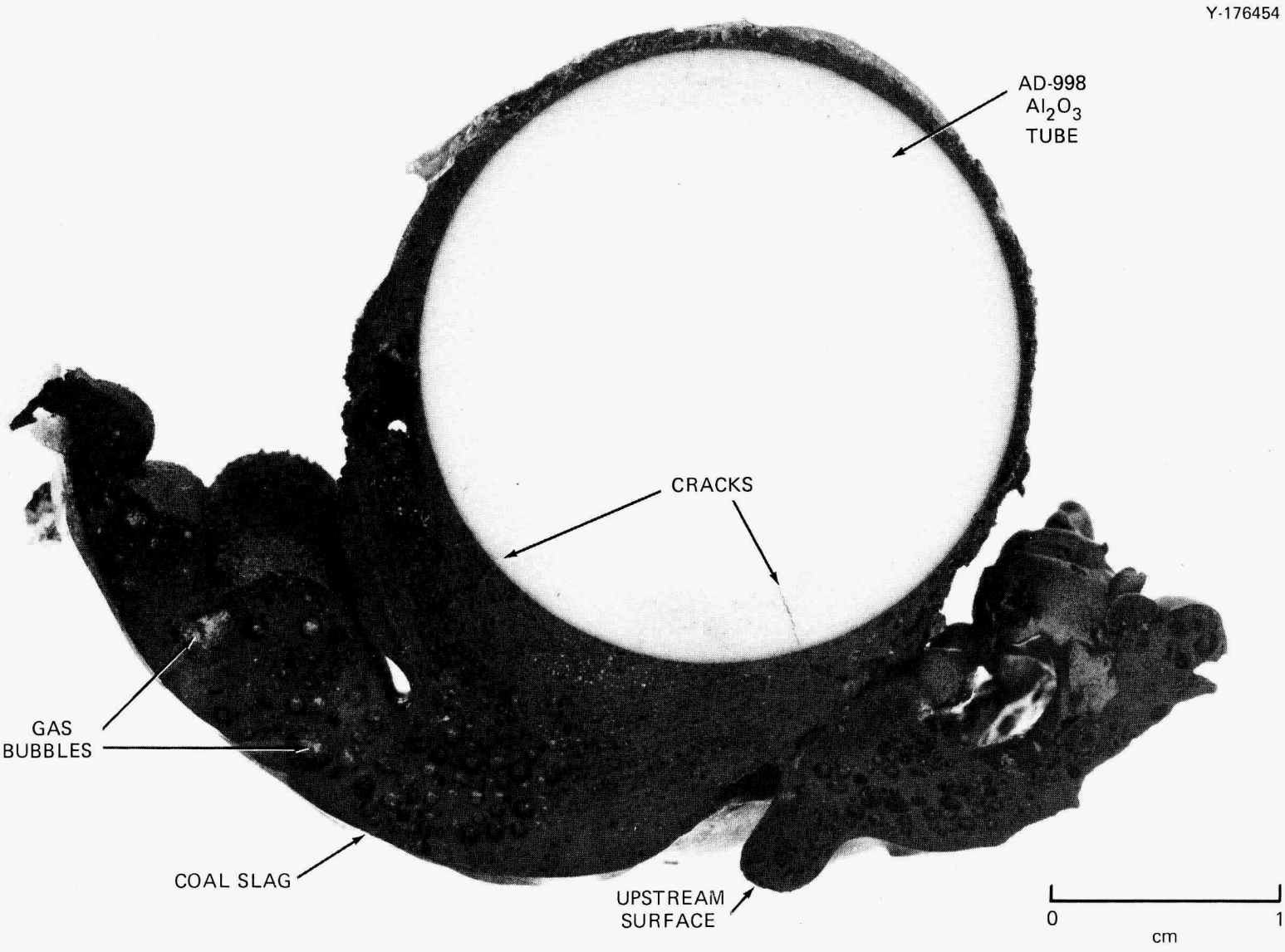

Fig. 21. Cross-sectional view of exposed AD-998 Al_2O_3 tube.

into the tubes lowered the temperature in the vicinity of the air inlet port, which limited the slag mobility and ultimately resulted in the columnar buildup. Since the magnitude of the temperature reduction attributable to the air flow through the tubes decreased as the air outlet side was approached, the temperature of the slag and thus its fluidity increased with increasing distance from the air inlet port. Consequently, the enhanced slag mobility resulted in a more uniform upstream surface morphology. However, in spite of this increased fluidity, the cross-sectional view (Fig. 21) indicates that the overall shape of the slag deposit, which depended on both the slag viscosity and the aerodynamics of the flue gas around the tube, was still quite complex. In addition, the upstream coal slag contained an intricate network of gas bubbles, whose average size increased with increasing radial distance from the tube surface. Finally, it should be pointed out that the cracks observed in the exposed Al_2O_3 tubes (Figs. 20–21) were also found in the sialon tubes but not in the silicon carbide materials. Reasons for this cracking problem are discussed in more detail below.

The upstream coal slag was easily removed from all the SiC tubes after cooldown following completion of the test exposure. Figure 22 shows the upstream surface of a KT SiC tube along with the upstream slag, which was removed and rotated 180° to expose the surface adjacent to the tube. Close examination indicates that the number and size of the voids or gas bubbles at the slag-ceramic interface gradually increased as the air outlet side of the tube was approached. This behavior, which is also reflected by the variation in the extent of the slag remnants remaining on the upstream KT SiC surface (Fig. 23), was presumably due to increase in interfacial temperature along the tube that resulted as the air temperature increased during its flow through the tube. Figure 24, which is a cross-sectional view of the KT SiC with the upstream slag removed, suggests that the surface receded only a limited amount in the material as a result of the high-temperature exposure to the coal slag. These results were typical of all the silicon carbide tubes. In fact, neither the α-SiC nor the CVD SiC showed evidence of appreciable surface corrosion.

The increased resistance to slag removal exhibited by the alumina and sialon tubes gave evidence of greater bonding between these ceramics and

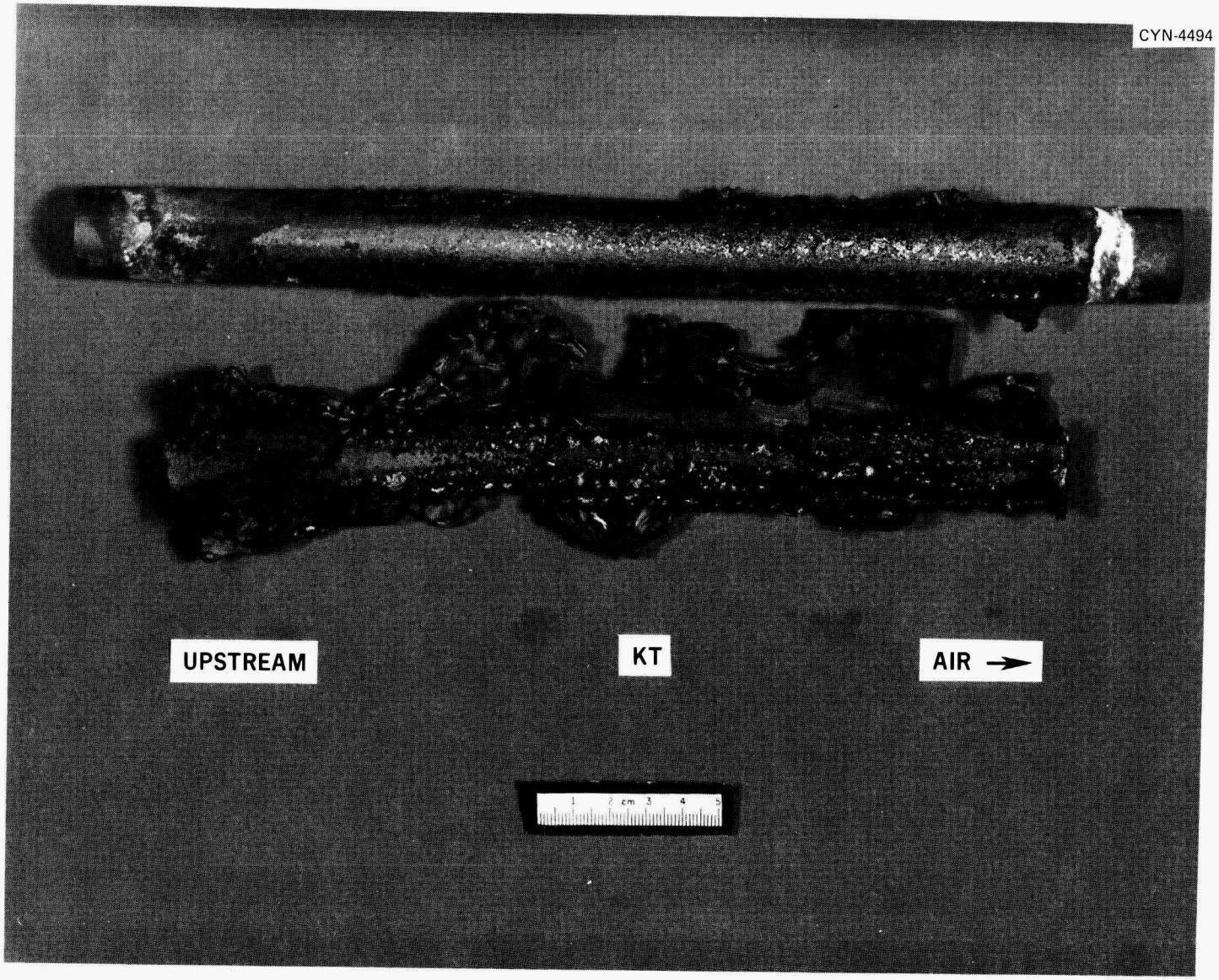

Fig. 22. Upstream view of exposed KT SiC and removed coal slag.

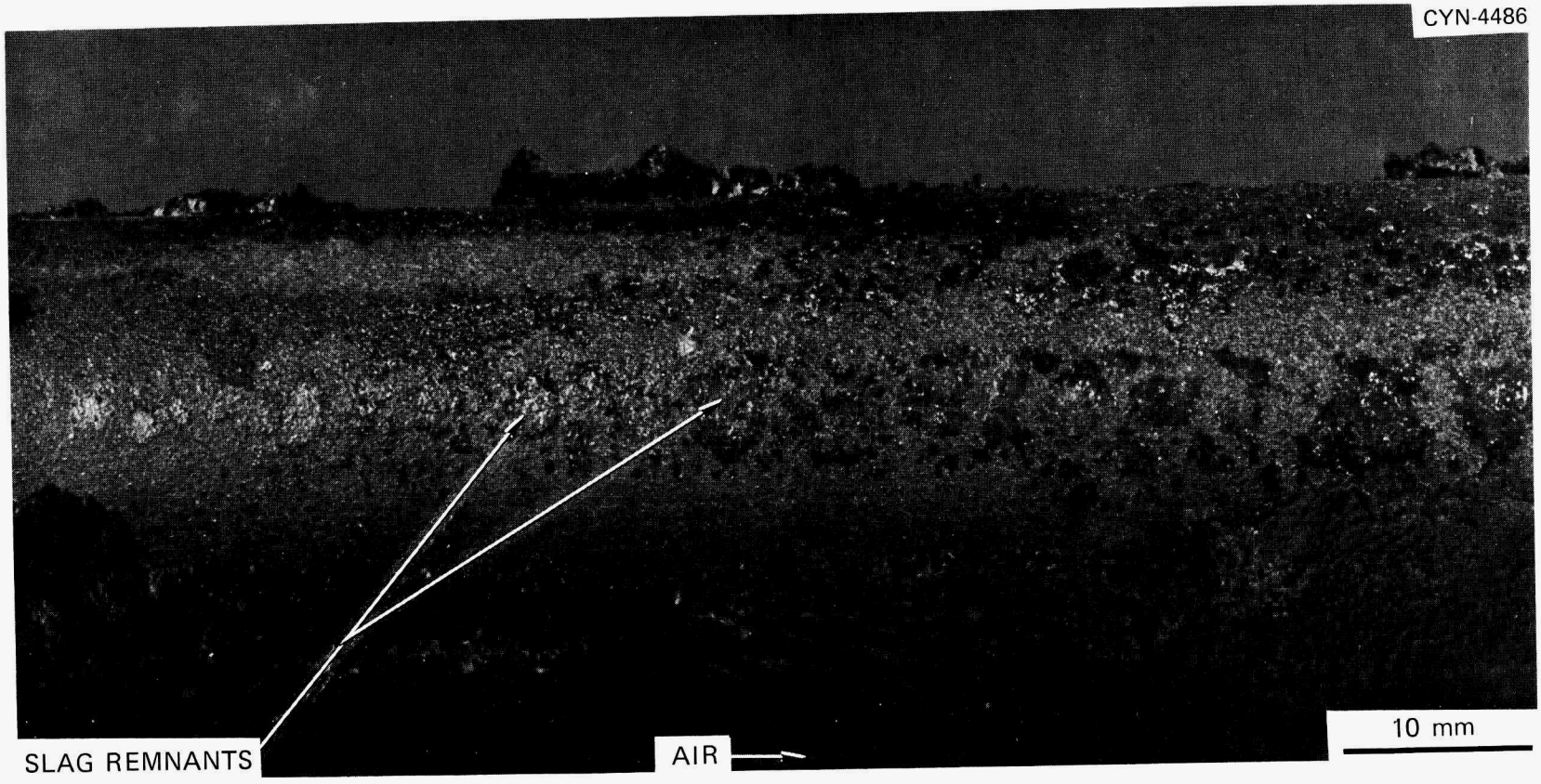

Fig. 23. Upstream surface of exposed KT SiC, showing slag remnants.

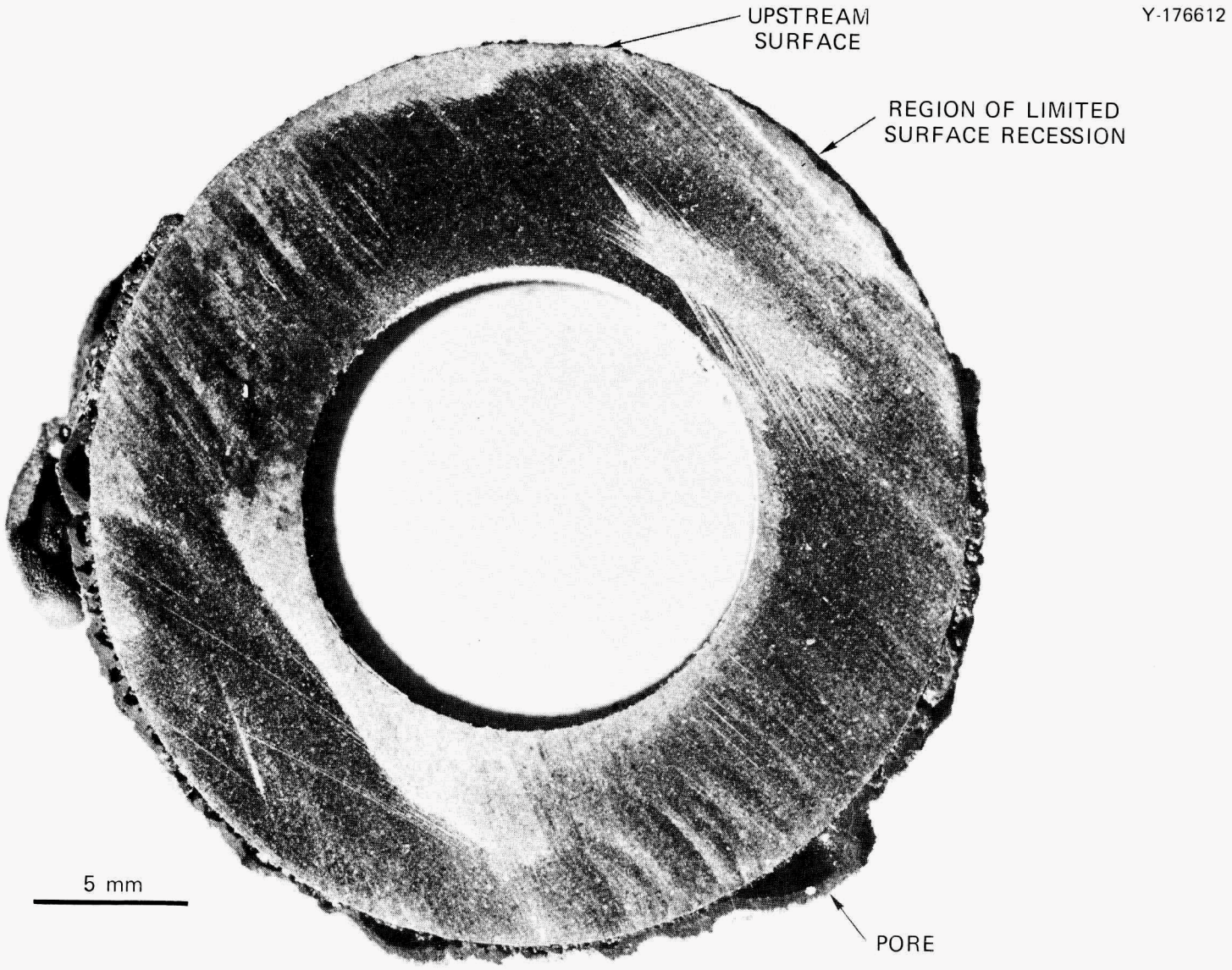

Fig. 24. Cross-sectional view of exposed KT SiC.

the slag. In the case of the alumina tube, Fig. 21 indicates that the Al_2O_3-slag interface was relatively distinct (i.e., the bonding was very localized). However, two intermediate phases were observed at the interface between the slag and the sialon tubes. The first phase, which was adjacent to the tube surface, was light colored and approximately 150 μm thick. This phase, which is shown in Fig. 25, was apparently formed by oxidation of the sialon. This oxidation product was also observed at the ends of the tube along the outside surface. These end regions, which were protected by the KT SiC extension tubes during the actual exposure, are shown in the upstream view of the exposed tube (Fig. 26). The second phase occurred between the oxidation layer and coal slag (Fig. 25). It was brownish and approximately 30 μm thick. The chemical characteristics of both phases are discussed in more detail in the following section.

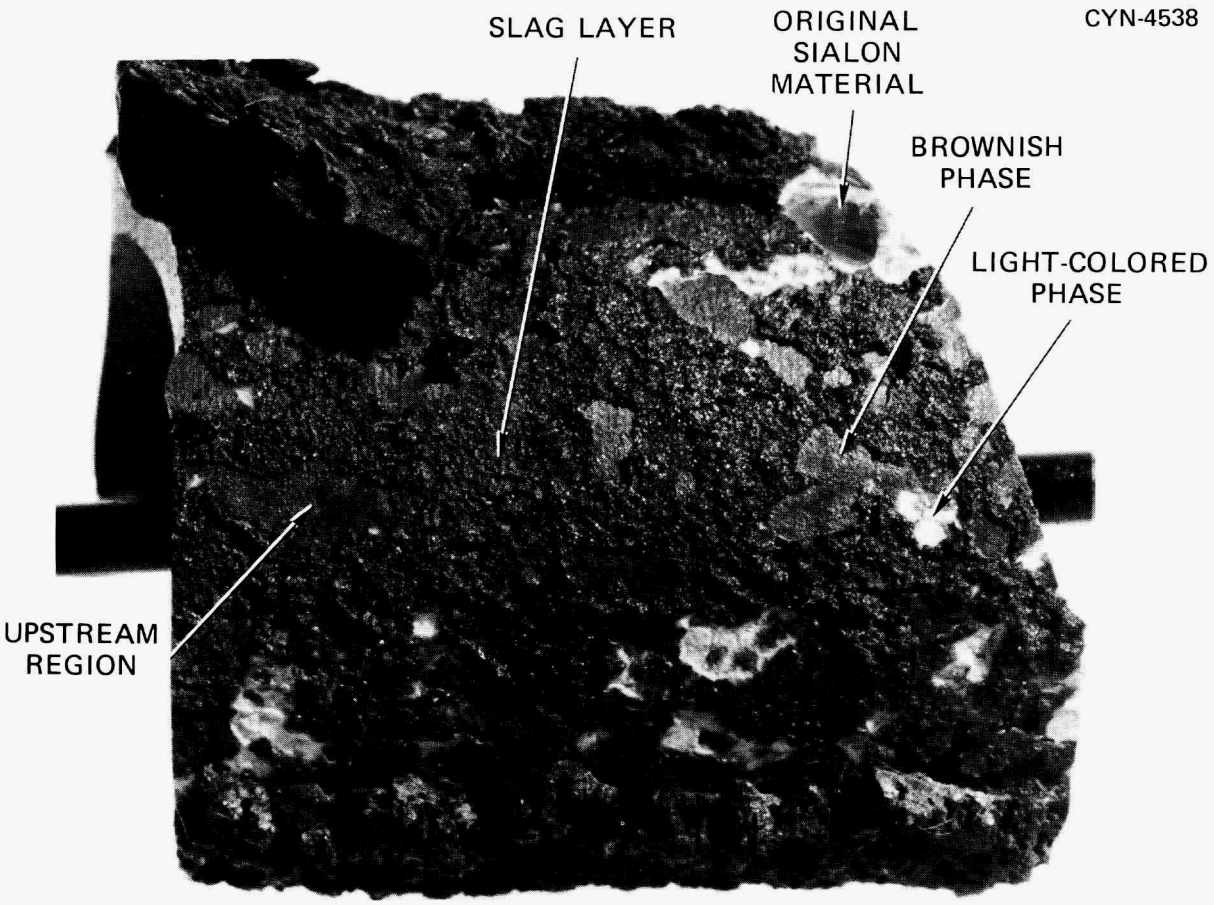

Fig. 25. Upstream surface of exposed sialon tube, showing various phases formed.

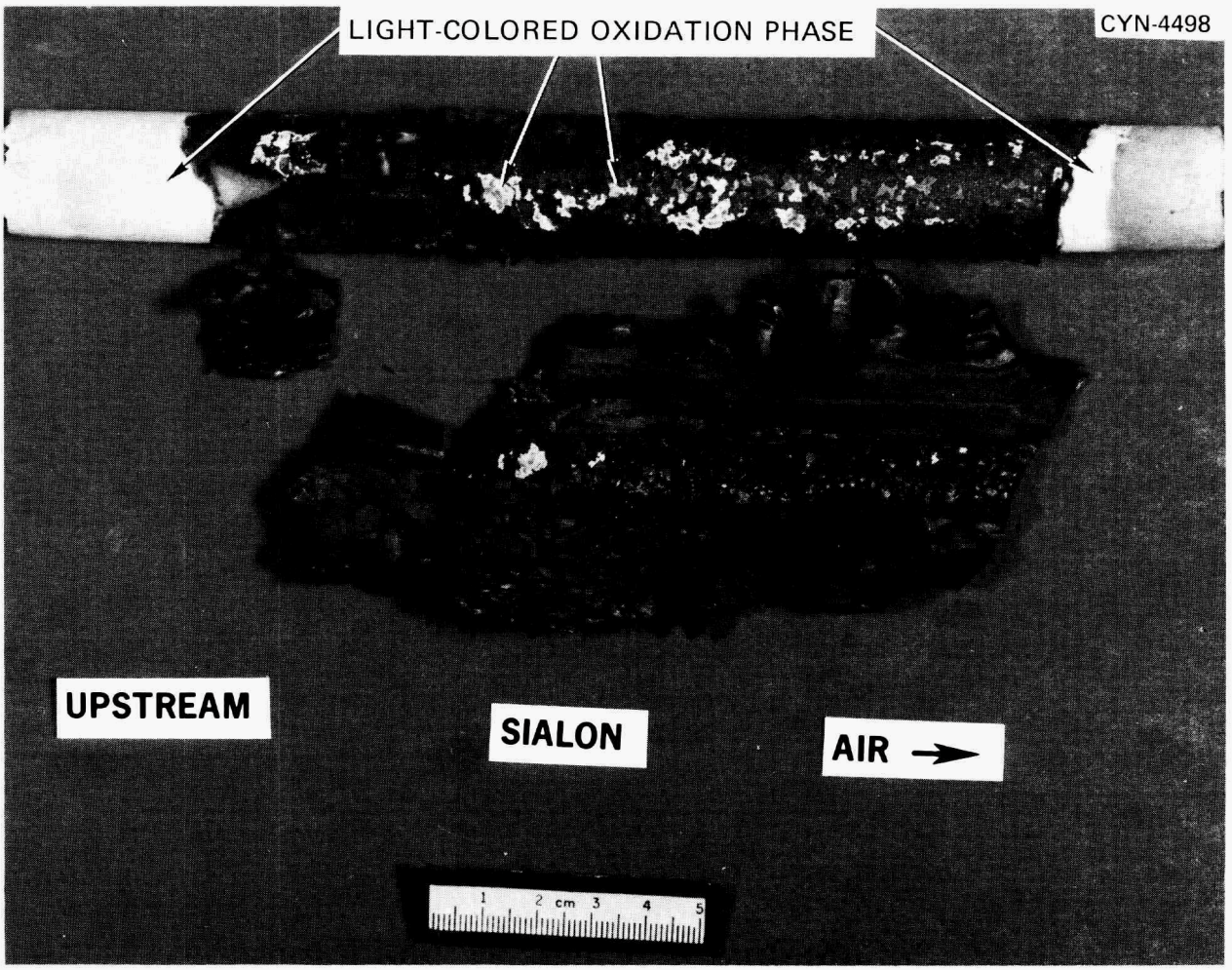

Fig. 26. Upstream surface of exposed sialon tubes with the coal slag removed.

No cracks were observed in any of the exposed SiC tubes with a low-power optical examination. However, radial and longitudinal cracks were clearly present in the Al_2O_3 (Figs. 19–21) and sialon (Fig. 27) tubes. The alumina probably cracked during the final cooldown, since slag had not penetrated into the tube interior or along the crack surfaces. The appearance of fly ash on the interior of the air outlet side of the sialon extension tube suggested that this material had cracked at some time during the high-temperature exposure, possibly during one of the thermal cycles. However, no slag was observed along the crack surfaces in these tubes. The extensive cracking in these two materials could have been related to the increased slag adherence. For example, if one assumes that the thermal expansion coefficient of the slag was less than that of either

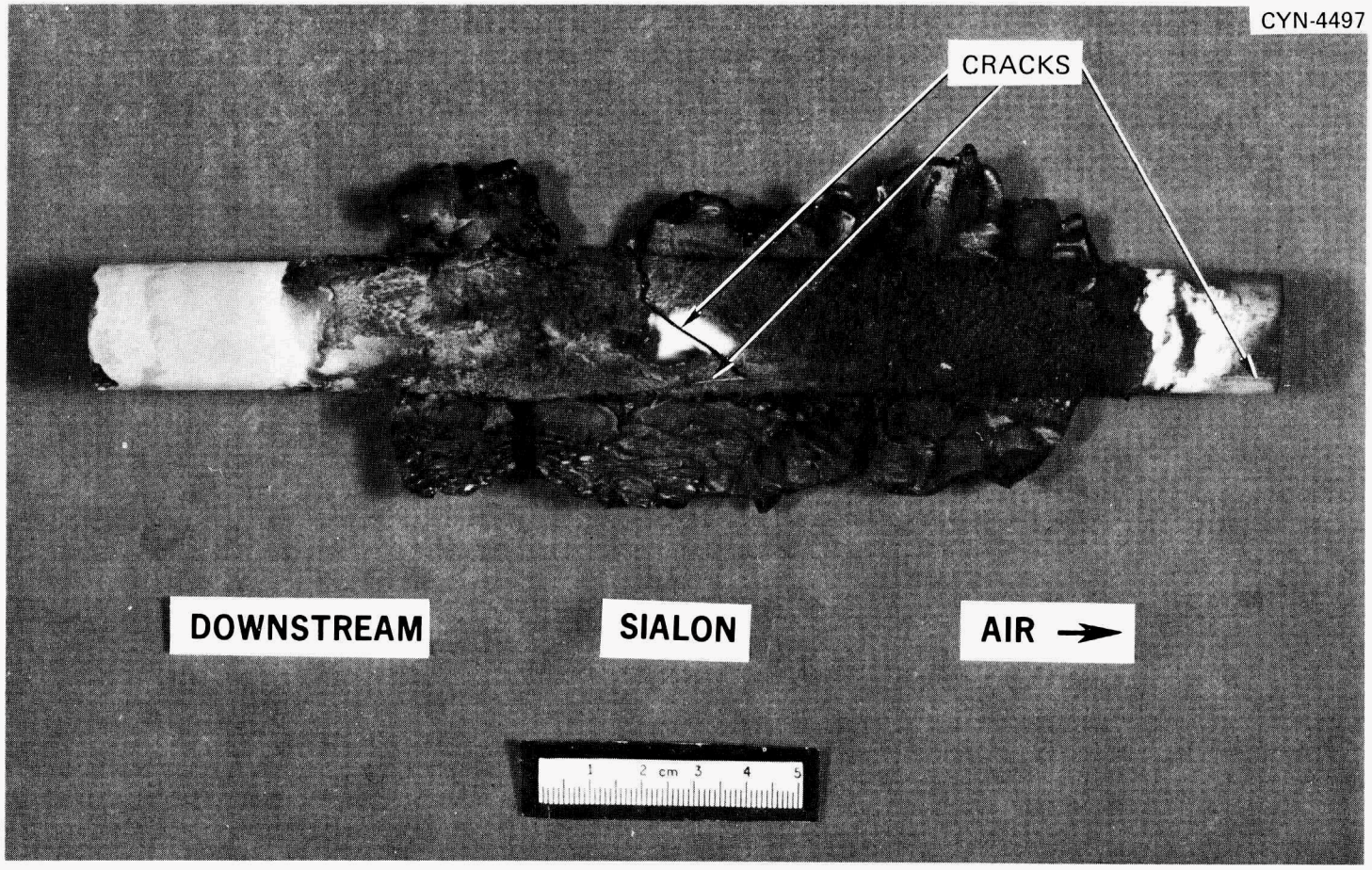

Fig. 27. Downstream surface of exposed sialon tube, showing extensive cracking.

the sialon or Al_2O_3, then upon cooldown the slag would partially constrain the contraction of the ceramic tube. The existence of this constraint would also require that the temperature be sufficiently low to avoid viscous deformation of the coal slag. Therefore tensile stresses would develop along the outside of the tube surface. An estimate of the stress magnitude is given in a subsequent section.

The macroscopic examinations also involved dimensional measurements and a radiographic analysis. The dimensions of all surviving tubes agreed with the respective pretest values given in Table 5, hence the 496-h exposure caused no large-scale deformation of the tubes. The pretest radiographic analyses did not reveal any major defects in any of the tubes. Unfortunately, program schedule constraints prevented the posttest radiographic examination. However, successful evacuation of all surviving SiC tubes to less than 13 mPa (1×10^{-4} torr) during the helium permeability analyses suggests that these materials contained no through-thickness defects.

Microcomposition

The results of the microcompositional studies — including wet chemical analysis, spark source mass spectroscopy, induction-coupled plasma spectroscopy, and fast-neutron activation analysis — are summarized in Table 9. The elemental composition of both as-received and exposed samples of the five tubular materials is given in the table. In general, the exposed samples were limited to the upstream region of the tubes. In addition, the analytical specimens removed from these tubular materials were cut to remove the residual coal slag from the upstream surface. Therefore, elemental variations in Table 9 represent changes that occurred in the bulk material as a result of the long-term exposure to the COM combustion products. Table 9 also includes the primary elements detected in representative upstream and downstream samples of the coal slag removed from several of the tubes. However, some of the major elemental concentrations (silicon in the SiC-based materials and aluminum and oxygen in the Al_2O_3 ceramic) are not given as specific values because inherent limitations in the analytical techniques precluded their measurement.

Table 9. Results of elemental analyses of as-received and exposed tubes plus upstream and downstream coal slag samples[a]

Element	Concentration, wt ppm[b]											
	KT SiC		Alpha-SiC		CVD SiC		Sialon		Al_2O_3		Coal Slag	
	As received	Exposed	As received	Exposed	As received	Exposed	As received	Exposed	As received	Exposed	Downstream	Upstream
Al	900	700	900	700	900	80	17.8%[c]	16.9%[c]	Major	Major	10.0%[c]	11.9%[c]
B	3.0	1.0	800	70	0.3	5	40	5	1	5	200	3
C (free)	0.87%[d]	0.68%[d]	0.38%[d]	0.56%[d]	<0.06%[d]	<0.1%[d]	na	na	na	na	na	na
Ca	80	70	30	70	30	20	0.1%[c]	0.1%[c]	100	500	2000	700
Co	≤2	900	≤1	3000	≤2	900	2000	900	<0.3	3	300	300
Cr	30	80	30	800	30	20	300	50	20	20	800	200
Cu	40	20	3	20	5	3	10	10	<0.5	3	100	30
Fe	3000	2000	300	800	2000	800	0.6%[c]	0.7[c]	500	8	9.1%[c]	8.0%[c]
Ga	<1	3	<1	5	<1	<3	<3	5	40	200	200	200
K	10	30	1	100	40	30	200	1000	0.1	10	3000	3000
La	≤5	20	≤5	10	≤5	3	3	5	0.1	<3	50	50
Mg	<1	10	<1	10	10	≤10	2.3%[c]	2.3%[c]	20	70	20	200
Mn	200	200	3	5	20	5	100	50	5	1	200	200
Mo	<3	5	<3	5	<3	10	30	5	na	na	na	na
Na	20	5	5	70	20	20	60	50	8.0	20	0.3%[c]	0.4%[c]
Ni	40	100	20	400	40	10	60	400	6.0	100	0.1%[c]	0.3%[c]
O	0.06%[e]	0.36%[e]	0.06%[e]	0.28%[e]	0.08%[e]	0.59%[e]	12.6%[e]	14.6%[e]	Major	Major	na	na
P	10	3	1	3	3	3	10	30	0.5	10	300	300
S	10	10	10	10	10	10	40	100	20	40	40	100
Si	Major	Major	Major	Major	Major	Major	na	na	na	na	na	na
Si (free)	7.83%[d]	7.74%[d]	na	na	<0.1%[d]	0.1%[d]	na	na	500	200	na	na
Ta	≤2	100	≤2	5000	≤2	50	2000	500	na	<20	20	50
Ti	200	100	60	600		10	1000	200	20	200	0.4%[c]	0.5%[c]
Y	<1	1	<1	1	<1	<1	5	20	30	21	10	5
V	70	200	20	10	70	1	10	200	5	5	600	600
Zn	<0.7	<3	<0.7	20	<0.7	<3	20	3	<0.03	3	200	200
Zr	0.20	20	≤1	5	0.4	1	10	20	8	20	50	10

[a]Determined by spark-source spectroscopic analysis unless specified otherwise; na means not analyzed.

[b]Weight percent if % is shown.

[c]Determined by inductively coupled plasma spectroscopy.

[d]Determined by wet chemical analysis.

[e]Determined by neutron activation chemical analysis.

KT SiC (Siliconized SiC)

For the KT SiC ceramic, the elemental composition changes considered significant include contents of the free C, Fe, Na, Ni, O, free Si, V, Co, and Ta. The free carbon content decreased from 0.87 to 0.68 wt %, indicating that some of the free carbon, which is typically present in siliconized SiC, either oxidized or reacted to form some oxidation-resistant carbide during the exposure. The microstructural observations indicate that the free carbon decrease was most likely due to carbon oxidation to CO or CO_2 during the high-temperature exposure. The elemental iron concentration decreased slightly from 3000 to 2000 wt ppm, which is opposite to the relatively large increase observed[1] in the KT SiC exposed to No. 6 oil combustion in CRAF Test 1. In that experiment both iron and nickel from the fuel ash diffused into the silicon phase of the material, but that process did not occur as readily in this experiment. The nickel content increased only slightly from 40 to 100 ppm in the KT material during the Test 2 exposure, whereas it increased by a factor exceeding 100 during No. 6 oil combustion exposure in Test 1. In Test 1, the nickel and iron from the fuel ash diffused into the silicon phase and were always located together within the silicon in the siliconized SiC. This diffusion process was apparently impeded in the presence of the coal slag during Test 2, perhaps because the slag covered the tube surface and protected it from the nickel present in the oil ash in the COM fuel. Also, in Test 2 the iron present in the slag liquid did not diffuse into the KT SiC. This observation suggests that nickel plays some role in allowing iron to diffuse into the silicon phase. Since the concentration of iron and nickel in the silicon phase of siliconized SiC is expected to result in formation of low-melting eutectics, their presence or absence could have considerable importance to the high-temperature mechanical properties of this type of ceramic. The decrease in sodium content in the KT SiC indicated that alkali ions do not diffuse readily from the siliceous slag into this ceramic. The oxygen content increased by about the same ratio (final/initial oxygen $\approx$ 6) as observed in Test 1, and this oxygen was probably present as crystalline and amorphous phases on both the internal and

external tube surfaces. The free silicon content was essentially unchanged by the exposure during Test 2. The tubes employed in this test contained about 7.8 wt % free silicon compared with a value of 9.1 wt % in the tubes exposed in Test 1. This observation illustrated the rather wide variation in the silicon phase content in this commercial ceramic material. The manufacturer's data sheets for KT SiC state the free silicon content as having a nominal value of 10 wt %. The vanadium content of this ceramic increased by a factor of about 2.9 to 200 ppm during Test 2. In Test 1, this ratio increased by a factor of 50 to about 1000 wt ppm, indicating that vanadium in the combustion gases from No. 6 oil alone diffuses more readily into the KT SiC than when coal slag is present. Therefore the presence of a coating of coal slag on the outer tube surface apparently inhibited transport of iron, nickel, and vanadium from the combustion gas into the carbide in some manner. Both the cobalt and tantalum concentrations increased from below detection limits of ≤2 wt ppm in the as-received material to 900 and 100 wt ppm, respectively, in the exposed materials. The same type of change (an increase in these two elements with exposure) was observed for the other two types of SiC-based ceramic materials studied. Cobalt was detectable at a relatively low concentration in the fuel, as shown in Table 3, and this may be the source of some of the cobalt detected in the exposed SiC ceramics. However, according to cobalt analysis of the fuel shown in Table 3 and the 36.8 Mg of fuel burned, only about 20 g Co was available from the fuel. Other sources of cobalt might include the combustor lining, which included a variety of experimental oxide refractories.

Sintered α-SiC

For the sintered α-SiC ceramic, the elemental composition changes considered significant include B, free C, Cr, Fe, Ni, O, Ti, Co, and Ta. Boron is employed as a sintering aid in the fabrication of this structural ceramic, and during the high-temperature exposure the boron concentration decreased by a factor of about 11. The boron apparently diffuses to the surface of this material during high-temperature oxidation and enters the siliceous oxidation products developed on the surface of the silicon

carbide. The free carbon content of the as-received α-SiC tubes was about 0.4 wt %. Transmission electron microscopic analyses of the α-SiC have shown the free carbon to be present in pyrocarbon or graphitic regions located largely at α-SiC grain junctions. They have dimensions up to about 0.1 μm, and apparently are the result of use of excess carbon in the formulation of this material.

The suggested increase in free carbon content of the exposed tubes to about 0.6 wt % from the chemical analyses is difficult to explain at present. The chromium content increased by a factor of about 27 to 800 wt ppm, and a similar change in chromium concentration occurred in this material in Test 1. The analyzed chromium concentration in the fuel was about 2 wt ppm, and during the experiment some chromium probably became available from a few exposed ends of stainless steel anchors in the monolithic refractory door of the combustor and from chromium-bearing experimental refractories located in the combustor. Chromium concentrations in the slag deposited on the tubes and in condensate extracted from the hot gases above the tubes were also in the range from 200 to 7000 wt ppm. This material was the only SiC-type ceramic employed in this experiment that showed a significant increase in chromium. The iron concentration in the α-SiC tubes increased by a factor of about 3 to 800 wt ppm during the exposure, which is very similar to the increase observed in Test 1. The extensive iron present in the coal slag in this exposure did not therefore result in a substantial increase in iron diffusion into this material. The nickel content in exposed α-SiC from Test 2 of 400 wt ppm was about the same as noted in Test 1, which suggests that under the exposure conditions of Test 2 nickel diffused into this ceramic about as readily as in the presence of residual oil combustion gases alone. This behavior is in contrast to the previously discussed observation for siliconized KT SiC, which showed more diffusion of iron and nickel into the KT SiC when coal slag was not present. These results suggest that nickel may diffuse into α-SiC from the slag by a different process than that operative in siliconized SiC ceramics. The analyzed oxygen concentration of about 0.3 wt % in the exposed α-SiC from this experiment is probably due to remnants of the coal slag on the outer surface of the tube as well as the silica oxidation film present on the inner

surface of the tube. The oxygen concentration is similar to that observed for this material in Test 1. The titanium concentration increased by a factor of 10 during the exposure to 600 wt ppm. The source of titanium in this case was apparently the coal ash, which contained 0.62 wt % of titanium expressed as TiO_2 equivalent, as shown in Table 1. Some titanium apparently diffused from the siliceous slag into the carbide during the exposure. Other elements such as cobalt and tantalum had substantial indicated concentration increases from the exposure, similar to the behavior of KT SiC, and no obvious explanation for these changes has been found. They may be due to selective contamination from carbide mills used to crush the analytical specimens, but this rationale is not supported by the analytical results for either the sialon or Al_2O_3 ceramics to be discussed shortly. Analyses of the coal slag from the tubes indicated cobalt and tantalum concentrations of 300 and 50 wt ppm, respectively, while relatively little cobalt was present in the fuel as noted previously. In summary, these results suggest that cobalt and possibly tantalum diffuse from the combustion atmosphere into α-SiC and KT SiC under the conditions of this exposure as well as those of Test 1.

CVD SiC

The significant elemental composition changes in the CVD SiC tubes from the exposure include Al, Co, Fe, O, and Ta. The elemental aluminum concentration in the as-received CVD SiC was 900 wt ppm and during the exposure it decreased by a factor of about 10, suggesting that aluminum diffused from the SiC into the slag on the outer tube surface or onto the inner tube surface, whereupon it was removed. The former situation is more reasonable. The cobalt concentration increased from a very low value to 900 wt ppm, suggesting that this SiC material assimilates cobalt from hot combustion gas environments, similarly to previously discussed results for KT SiC and sintered α-SiC. The iron concentration in the as-received CVD SiC tubes was relatively high at 2000 wt ppm and during the exposure this concentration decreased by a factor of about 3. The source of the high initial concentration of iron in this SiC is unknown, but it was presumably incorporated into the SiC during high-temperature deposition of the

tubes either from the chemical reactants, the graphite mandrels upon which they were deposited, or the equipment employed in synthesizing the carbide. The analyzed oxygen concentration increased by a factor of about 7 to 0.59 wt %, and this was again attributed to oxygen concentrated in small slag remnants of the exposed specimens. The microstructural and x-ray diffraction results of the exposed CVD SiC presented and discussed elsewhere in this report indicated no evidence of formation of oxygen-containing phases in the interior of this material or the other SiC-based ceramics. The tantalum concentration in exposed specimens increased from less than about 2 wt ppm in the as-received tubes to 50 wt ppm. This increase was similar to those shown in Table 9 for KT and sintered α-SiC.

GE 128 Sialon

The microcompositional analyses of the as-received and exposed sialon revealed fairly large concentrations of Al, Mg, O, Fe, and Ca. The presence of the first three elements is consistent with the reported starting composition (Table 7). The iron and calcium probably represent contamination products that were introduced during fabrication.[6] In addition the concentrations of S, K, B, O, Ni, and V in the exposed sialon were slightly larger than those in the as-received material. These increases likely resulted from the initial exposure of the sialon to the combustion products of the COM fuel. Notice that S, K, B, Ni, and V were present in both the COM fuel and the flue gas condensables (Table 3). However, the subsequent buildup of the refractory coal slag on the sialon tube and its reaction with the outer surface during the 496-h test may have prevented the concentrations of these elements from increasing further within the bulk of the sialon. This appears to be confirmed by the fact[1] that the exposed tubular materials in CRAF Test 1, which were covered only with small isolated nodules, contained fairly large concentrations of fuel impurities such as Ni, Fe, V, Na, and Cr when compared with the as-received materials. Table 9 indicates that the concentrations of Co, Cr, Mn, Ta, and Ti, which were fairly large in the as-received sialon, decreased significantly during the 496-h exposure. Therefore, the thick coal slag that formed upon the sialon was able to inhibit the diffusion of

some elements but not others. The sources of the relatively large concentrations of Co, Cr, Mn, Ta, and Ti in the starting material are unknown. Some of them could have been unavoidably introduced during the sample preparation.

AD 998 Al_2O_3

The primary impurity elements (>100 ppm) in the as-received Al_2O_3 were calcium, iron, and silicon. The 496-h exposure to the COM combustion products increased the concentration of calcium and decreased those of iron and silicon. Furthermore, tantalum, nickel, and gallium increased substantially during exposure. As before, the source of nickel was probably the COM fuel. These results are distinctly different from those obtained[1] in CRAF Test 1, in which the concentrations of Mg, Ca, Fe, Ni, and V in the Al_2O_3 exhibited large increases. Once again, the extensive deposit of coal slag upon the alumina tubes and the subsequent formation of an intermediate bonding phase at the ceramic-slag interface may have resulted in an effective diffusion barrier to these particular elements.

Coal Slag

The upstream and downstream slag samples contained extremely high concentrations of Al, Ca, Fe, K, Na, Ni, and Ti. As demonstrated later, all the elements except nickel were probably associated with the coal ash and the nickel was partitioned out of the No. 6 fuel oil. All remaining elements in the coal slag except B, La, Ga, and Ta were also present in the COM fuel (Table 3). However, the concentrations of Co, Cr, Cu, Mn, Zn, and V in the slag were slightly higher than one would expect from the analysis given in Table 3. This discrepancy provides further evidence that, during the 496-h exposure, these elements were selectively taken up into the siliceous slag matrix. The sources of the B, La, Ga, and Ta are again unknown. The results of the coal slag elemental analyses also indicate that minor differences occurred in the concentrations of several elements present in the upstream and downstream samples. For example, the

upstream concentrations of Al, Mg, Na, Ni, S, and Ti were higher than the respective downstream values, while the concentrations of B, Ca, Cr, Cu, Fe, Y, and Zr were lower. The reasons for these variations are uncertain.

Further insights into the composition of the coal slag were obtained from wet chemical analyses* performed on slag samples removed from the tubular materials and from several regions along the CRAF wall located above the tubular array. These results along with the coal ash analysis in Table 1 are summarized in Table 10. The coal slag composition was very similar to that of the coal ash. This similarity provides further verification that the chemical species in the flue gas that were responsible for the degradation of the tubular materials were primarily associated with the coal and not the No. 6 fuel oil. Therefore, the use of the COM to study the effects of coal combustion products upon the structural and chemical properties of candidate ceramic HX materials appeared to be highly successful. The fact that high concentrations of Al, Ca, Fe, Na, Ni, and Ti were generally not found in the exposed tubes, as in CRAF Test 1, suggests that the slag reduced the diffusion of these elements.

Table 10 also reveals several minor variations in the concentrations of the various equivalent oxides. For example, the equivalent CaO concentration was reduced from 2.72 wt % in the coal ash to less than 0.10 wt % in all the slag samples. This result suggests that under the exposure conditions the calcium in the coal ash was selectively partitioned out of the slag depositing upon the ceramic tubes and CRAF wall. Smaller reductions also occurred in Al_2O_3 and P_2O_5. Conversely, concentrations of SiO_2, MgO, TiO_2, and Na_2O were significantly larger in the slag samples than in the coal ash. Finally, the equivalent oxide concentrations of several elements in the slag tended to vary with the position of the slag in the CRAF unit. Specifically, the concentration of SiO_2 and Al_2O_3 increased while the concentration of Fe_2O_3 decreased with increasing distance above the tubular array.

---

*Wet chemical analysis by Spectrochemical Laboratories, Pittsburg, Pa.

Table 10. Wet chemical analyses of coal slag samples removed from tubular materials and CRAF wall

Equivalent oxide or element	Concentration, wt %			
	Coal slag adjacent to tubular materials	Coal slag from CRAF wall 0.36 m above tubular array	Coal slag from CRAF wall 0.71 m above tubular array	Coal ash analysis from Table 1
SiO_2	54.35	55.30	57.55	50.80
Fe_2O_3	21.42	17.88	14.74	16.28
Al_2O_3	18.68	21.29	21.69	23.93
CaO	0.10[a]	0.10[a]	0.10[a]	2.72
MgO	0.80	0.98	1.56	0.72
P_2O_5	0.12	0.01[a]	0.07	0.27
Na_2O	0.68	0.61	0.61	0.47
K_2O	1.76	1.68	1.68	1.60
NiO	0.34	0.28	0.38	[b]
SO_3	[b]	[b]	[b]	1.63
SO_2	0.014	0.016	0.012	[b]
Total C	0.033	0.032	0.006	[b]
TiO_2	1.29	1.37	1.29	0.62

[a]This value represents the detection limit of the particular element.

[b]Not analyzed.

Microstructure and X-Ray Composition

The microstructure of the as-received and exposed ceramic materials and that of the coal slag were characterized by using optical and scanning electron microscopy (SEM). The principal elements in the various microstructural phases were identified by energy-dispersive x-ray analyses in conjunction with the SEM examination. In addition, several x-ray diffraction studies were used to identify the phases in the as-received and exposed samples of all five ceramic materials. The postexposure analyses were limited to the upstream regions in each tube, where the reaction to the coal slag appeared to be the greatest. Upstream diffraction traces were obtained for both the surface and bulk material approximately 2 mm below the tube surface. Representative coal slag samples were also analyzed. The crystalline phases were identified by matching the *d*-spacings of the x-ray diffraction patterns with known spacings of specific crystalline materials given in the literature[7,12] or in the powder diffraction file published by the Joint Committee on Powder Diffraction Standards (JCPDS).[13] The results are summarized in Table 11, and the actual diffraction pattern indexings are given in the appendix.

KT SiC (Siliconized SiC)

The microstructure of this material included a two-phase mixture of SiC and silicon. The local concentration of silicon varied with distance through the tube wall. The silicon concentration was typically higher near the outer surface of the tubes than in the interior, as shown in Fig. 28, where the outer 20 μm or so of the surface consisted of a contiguous layer of SiC. Immediately under this layer the silicon concentration was relatively high in a zone having a thickness of about 200 μm. This type of ceramic material frequently contains phases in addition to the SiC and silicon, and under optical bright-field conditions these phases can frequently be observed because they are more reflective than silicon. These secondary phases are usually either metallic and contain relatively high concentrations of iron or they are graphitic. An example of some of the metallic and graphitic inclusions in as-received

Table 11. Crystalline phases in as-received tubes, exposed tubes, and coal slag

Material	Sample	Crystalline phases
KT SiC	As received	α-SiC(33R), α-SiC(12H), α-SiC(51R), Si, graphite(4H)
	Exposed, upstream surface	α-SiC(33R), α-SiC(12H), α-SiC(51R), Si, graphite (4H), unidentified phases
	Exposed, upstream subsurface	α-SiC(33R), α-SiC(12H), α-SiC(51R), Si, graphite(4H)
CVD SiC	As received	α-SiC(12H)
	Exposed, upstream surface	α-SiC(12H), graphite (4H), unidentified phases
	Exposed, upstream subsurface	α-SiC(12H), graphite(4H)
α-SiC	As received	α-SiC(33R), α-SiC(12H), α-SiC(4H), α-SiC(15R), graphite
	Exposed, upstream surface	α-SiC(33R), α-SiC(12H), α-SiC(4H), α-SiC(15R), graphite, unidentified phases
	Exposed, upstream subsurface	α-SiC(33R), α-SiC(12H), α-SiC(4H), α-SiC(15R), graphite
Sialon	As received, outer surface	β-Si_3N_4, $Si_3A_{2.67}N_4O_4$, β′-sialon, Mg-sialon(6H), unidentified phases
	As received, inner surface	β-Si_3N_4, $Si_3Al_{2.67}N_4O_4$, β′-sialon, Mg-sialon(6H)
	Exposed, upstream surface	β-Si_3N_4, $Si_3Al_{2.67}N_4O_4$, β′-sialon, Mg-sialon(8H), α-cristobalite, α-$Mg_2Al_4Si_5O_{18}$, $Al_2O_3 \cdot SiO_2$
	Exposed, upstream subsurface	β-Si_3N_4, $Si_3Al_{2.67}N_4O_4$, β′-sialon, Mg-sialon(6H)
Al_2O_3	As received	α-Al_2O_3
	Exposed, upstream surface	α-Al_2O_3, tridymite, α-quartz
	Exposed, upstream subsurface	α-Al_2O_2
Coal slag	Upstream	α-quartz, α-cristobalite, β-cristobalite, tridymite, $Fe(Al,Cr)_2O_4$, $3Al_2O_3 \cdot 2SiO_2$

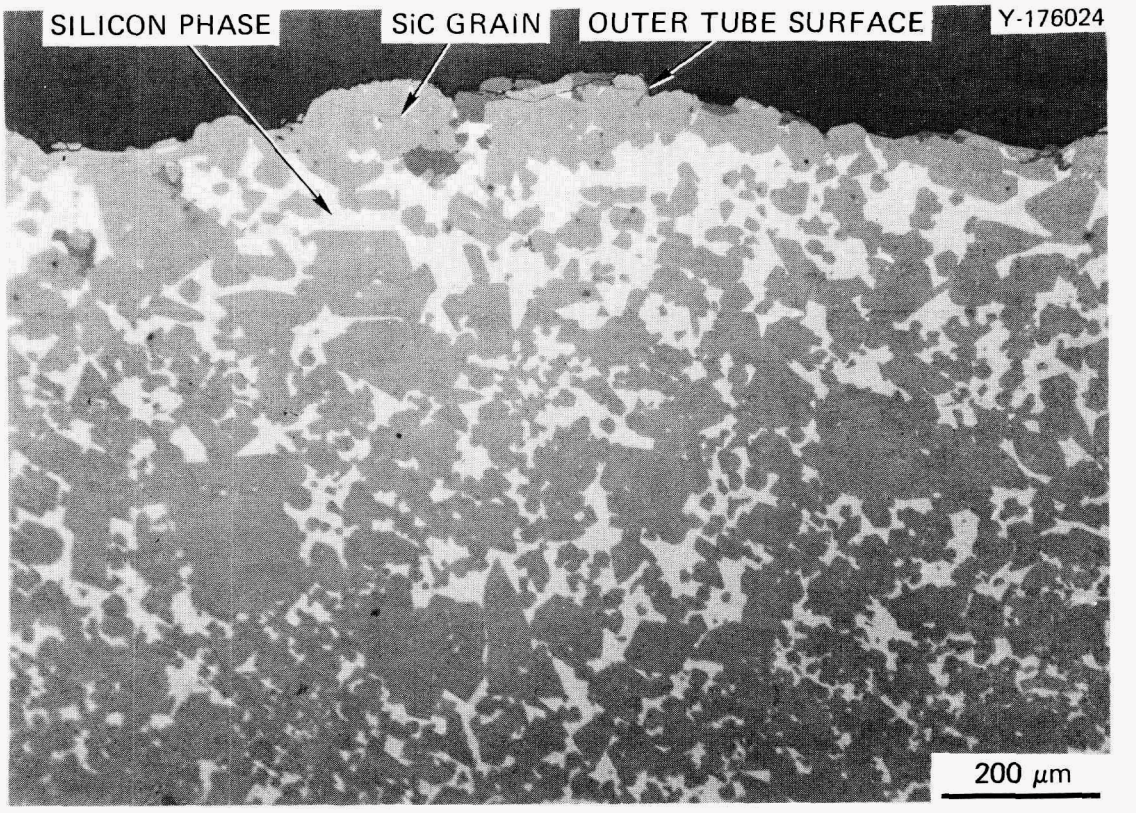

Fig. 28. Outer surface of as-received KT SiC tube, showing relation of SiC and silicon phases.

KT SiC tubes is shown in Fig. 29. Elemental analyses were performed of several of these regions and an example is shown in Fig. 30. The SEM image in Fig. 30(a) shows one of the inclusions located between several SiC grains. In Fig. 30(b) the same field is shown with the detector displaying only data for iron. The brighter object in Fig. 30(a) is obviously high in iron, but Fig. 30(c) shows that this inclusion is deficient in silicon relative to the surrounding silicon and SiC phases. Similar elemental analyses for titanium indicate no preferential concentration of this element in this inclusion, although concentrations of titanium had been found in other KT SiC specimens several months earlier. In summary, the microstructure of the as-received KT SiC tubes consisted of SiC grains varying in size from about 10 μm to as large as about 150 μm. These grains were surrounded by the silicon phase. Within the silicon phase other elements were present in localized regions having

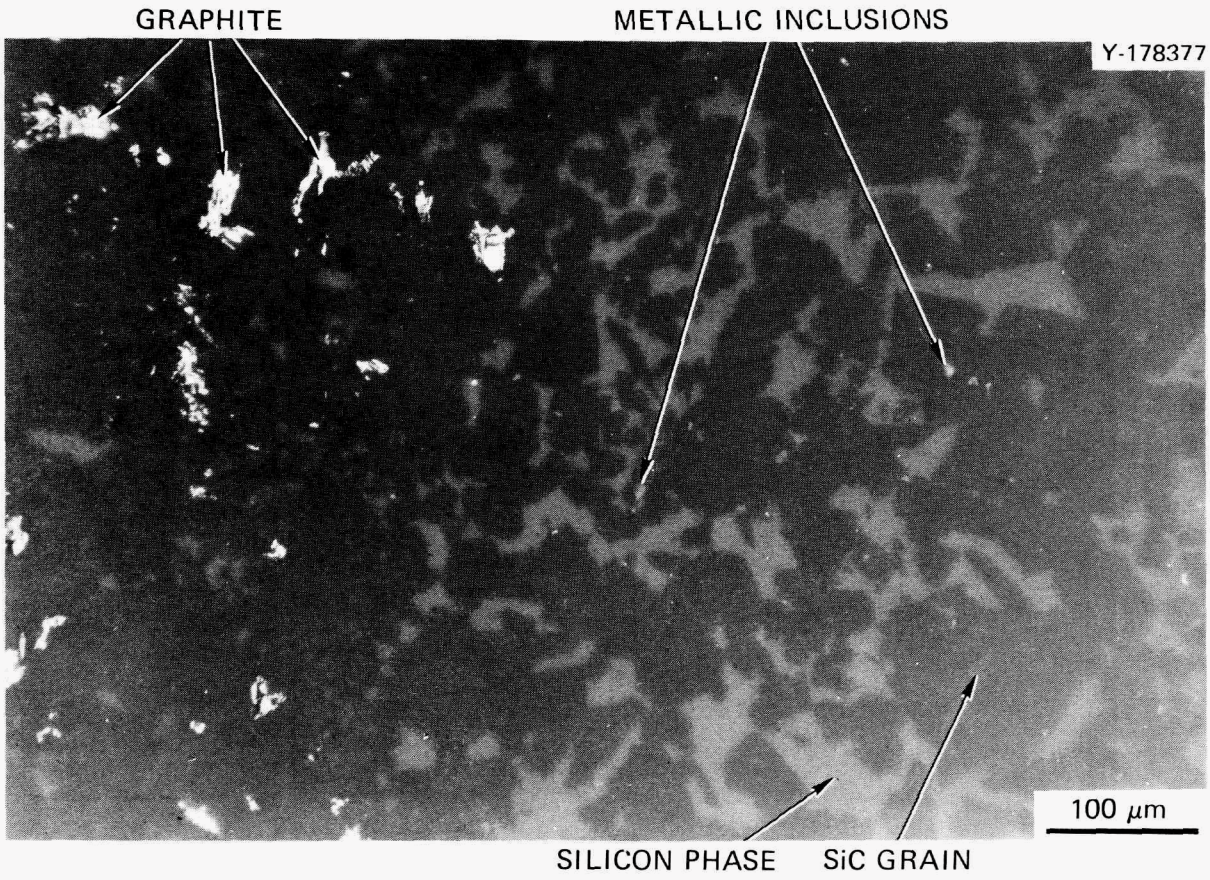

Fig. 29. As-received KT SiC tube showing localized concentrations of secondary metallic inclusions and graphite.

dimensions up to about 20 μm, but generally less than 10 μm. In the KT SiC tubes employed in this experiment, iron was the principal element present in these localized impurity regions or inclusions.

Following the combustion gas exposure, the KT SiC tubes were sectioned as shown in Figs. 13 and 14 and the microstructures characterized. Qualitatively, the KT SiC tubes appeared to be relatively stable in the presence of the coal slag, as noted previously in this report. Examination of the cross section of the upstream side of the outer tube surface showed localized corrosion, which was characterized by relatively small shallow pits, whose depth generally did not exceed about 50 μm. An example of the pitting is shown in Fig. 31, where a remnant of the coal slag glass is present in the shallow pit. The silicon and SiC phases

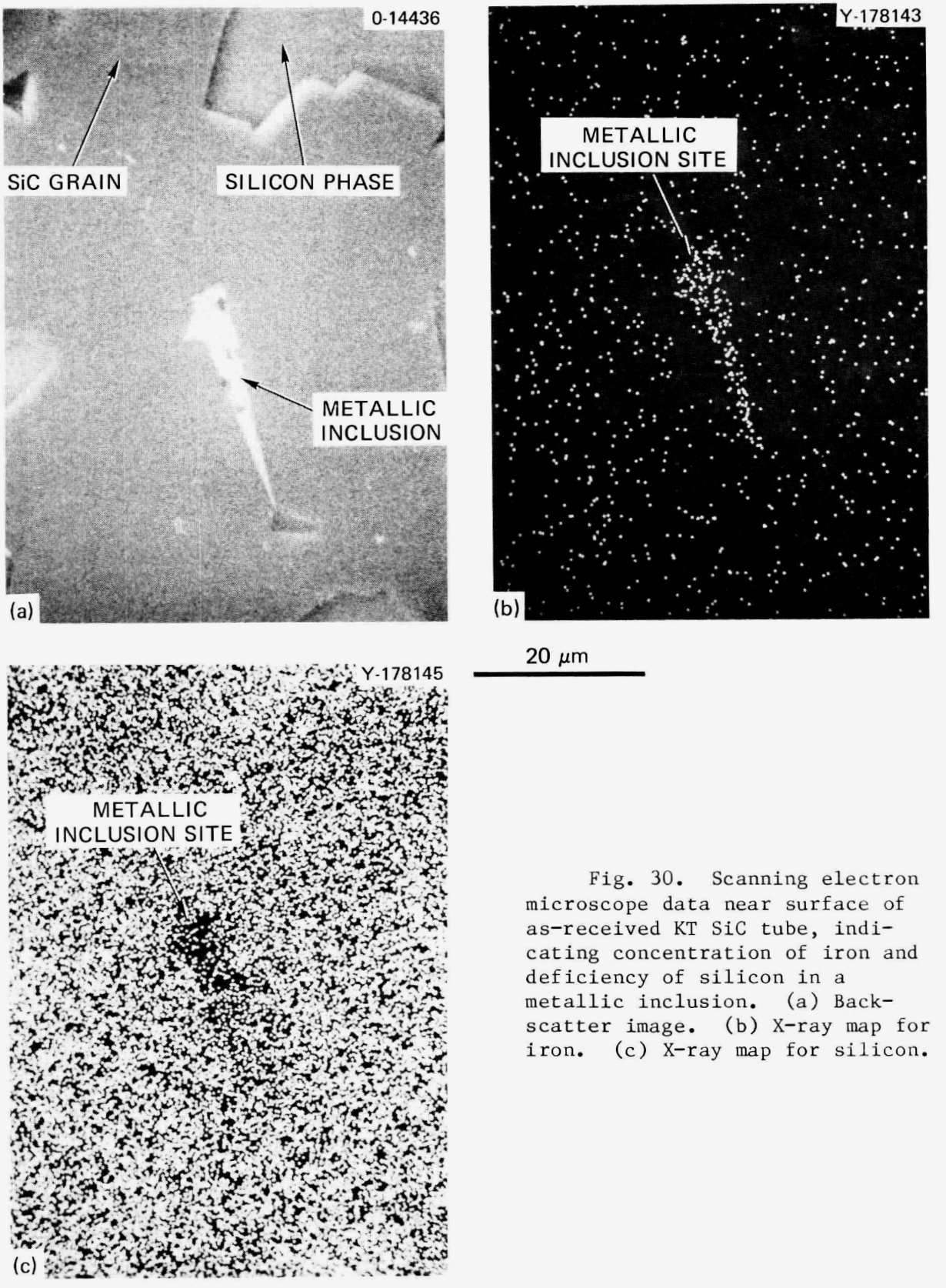

Fig. 30. Scanning electron microscope data near surface of as-received KT SiC tube, indicating concentration of iron and deficiency of silicon in a metallic inclusion. (a) Backscatter image. (b) X-ray map for iron. (c) X-ray map for silicon.

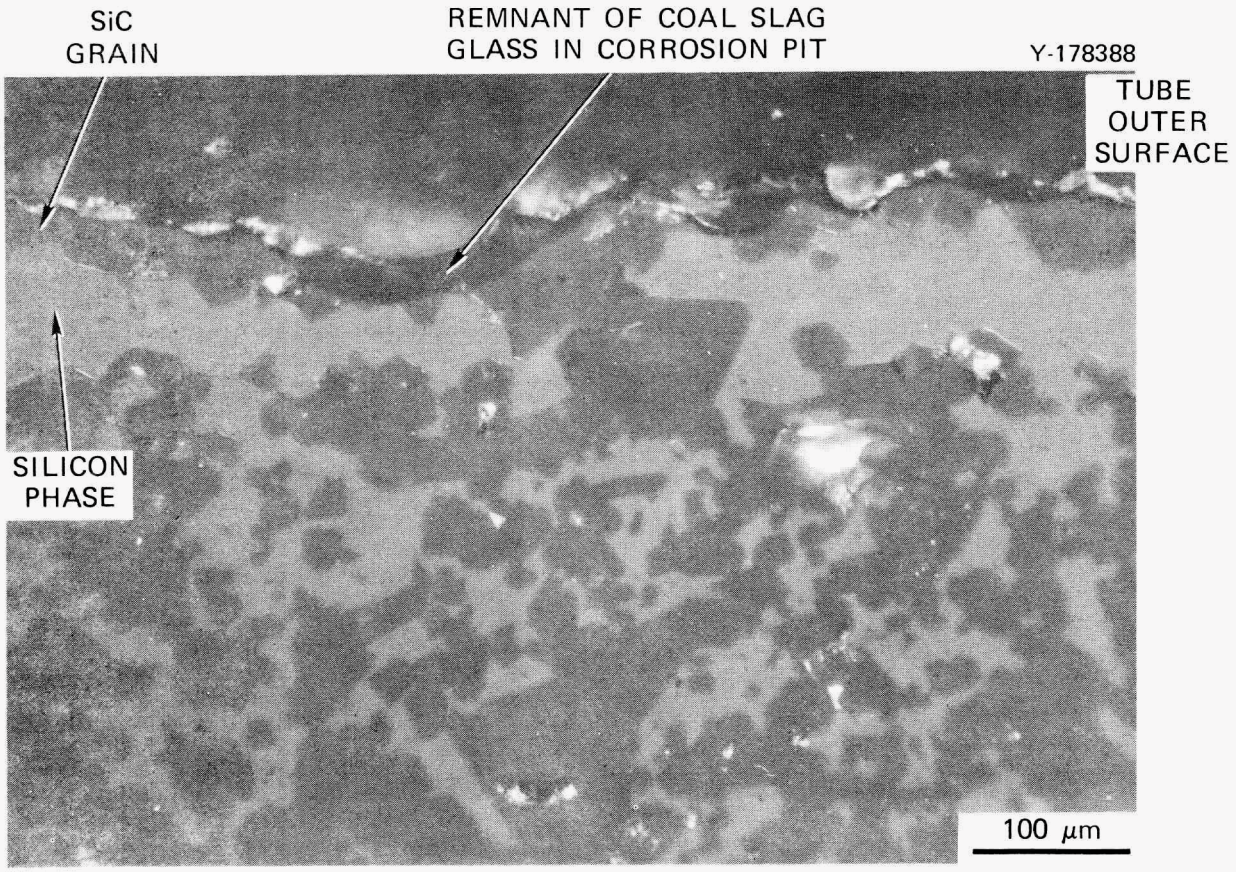

Fig. 31. Microstructure of upstream outer surface of KT SiC tube after exposure, showing corrosion pit.

corroded at very comparable rates. Micrographs illustrating details of the corrosion pit shown in Fig. 31 are shown in Fig. 32. Figure 32(a) illustrates in better detail the interface between the coal slag and the SiC and silicon phases and locates as well the secondary metallic phase inclusions originally present in this ceramic material. Figure 32(b) shows the bottom of the pit illustrated in (a) at higher magnification. In this micrograph, a small spherical object about 4 μm in diameter is located in the slag glass immediately above the tube surface. This object apparently came from the secondary phase region in the KT SiC located immediately below it in the tube wall. Removal of the secondary material from the carbide has produced a local micropit, which is filled with slag. The spherical shape of the object suggests that it was liquid under the

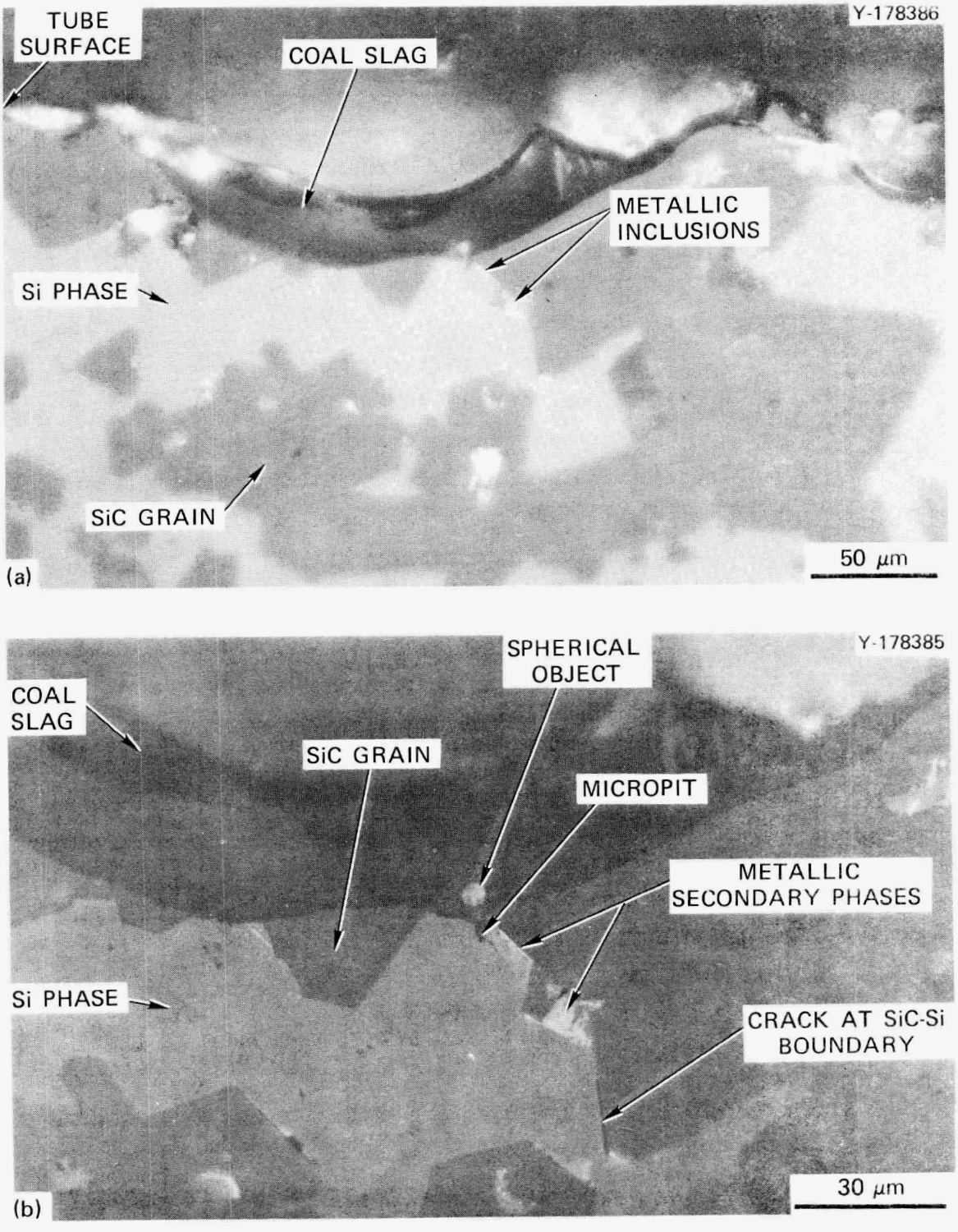

Fig. 32. Microstructural characteristics of corrosion pit in upstream side of exposed KT SiC tube. (a) Location of secondary metallic inclusions near bottom of pit. (b) Details of pit region, showing transport of secondary metallic material into slag, resulting in formation of a micropit.

exposure conditions. This observation indicates that the iron-rich secondary metallic inclusions often present in this type of ceramic served as origins for preferential corrosion under the exposure conditions employed. Examination of the KT SiC specimen also revealed some tendency for microcracking. Near the micropit discussed previously [Fig. 32(b)], an open crack of this type was observed at the boundary between an SiC grain and the silicon phase. Its location is shown in Fig. 32(b).

The surface structure of the upstream side of the tubes was studied by SEM following gentle mechanical removal of most of the coal slag. Figure 33 illustrates the typical appearance of the surface, which included a thin adhering layer of coal slag. The slag consisted of crystals dispersed in siliceous glass. Cracks were typically observed in the slag glass around the larger of these crystals, indicating that below a temperature at which the glass could no longer flow to relieve stress, the difference between the thermal expansion of large crystals and the glass was sufficient to stress the glass to fracture. A more detailed discussion of this situation is given later in this report.

Efforts to mechanically separate the coal slag from the surface of the exposed KT tubes to determine the surface appearance met with limited success. Removal of the bulk of the coal slag from the KT tubes left some remnant slag, which obscured surface details. One of the more definitive examples of these efforts is shown in Fig. 34. In this figure, a prominent feature is a fracture surface that propagated across a void or gas bubble within the siliceous slag, which was a liquid at the exposure temperature. The specimen orientation in the SEM gives the void in Fig. 34 an elliptical appearance. To the left of the void, a region of conchoidal fracture is visible in the slag. In the upper portion of the micrograph above the void, small crystals are visible in the slag. Immediately below and to the right of the void, the visible surface is relatively rough, and this region is considered to be the actual KT SiC surface. Failure to obtain a sharp image of this region was attributed to a thin residual amorphous glass coating, which caused rounding of surface features and loss of detail. The right-hand side of the micrograph shows more conchoidal fractures in the slag glass. The void in Fig. 34 is thought to be a local oxidation site on the KT SiC tube surface and probably represents the location of a pit in the tube surface.

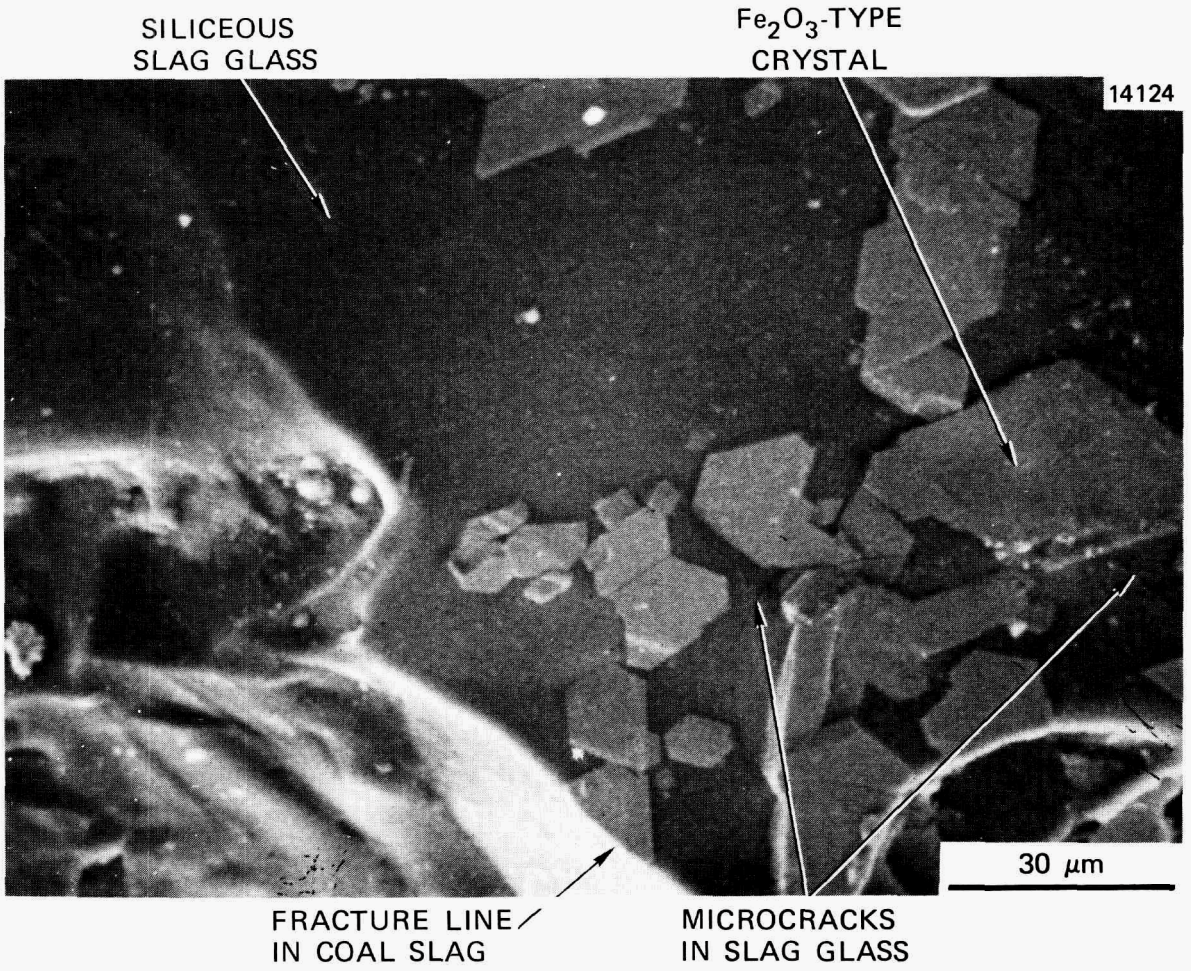

Fig. 33. Scanning electron micrograph showing fracture characteristics of upstream side of exposed KT SiC tube and details of adherent coal slag.

X-ray diffraction analyses were conducted for as-received and exposed KT SiC specimens. The phases identified are listed in Table 11. The SiC phase was hexagonal and included the three polytypes 33R, 12H, and 51R. Other major phases were silicon and graphite. The data for the surface specimen indicated the presence of a small amount of unidentified phase(s) having d-spacings of 0.448, 0.372. 0.326, 0.283, 0.281, and 0.275 nm. These lines had intensities of up to 5% of that of the 0.25-nm line of α-SiC and were presumably the stronger lines for the phase(s). In summary, the combustion exposure did not result in significant changes in the major phase types present in KT SiC.

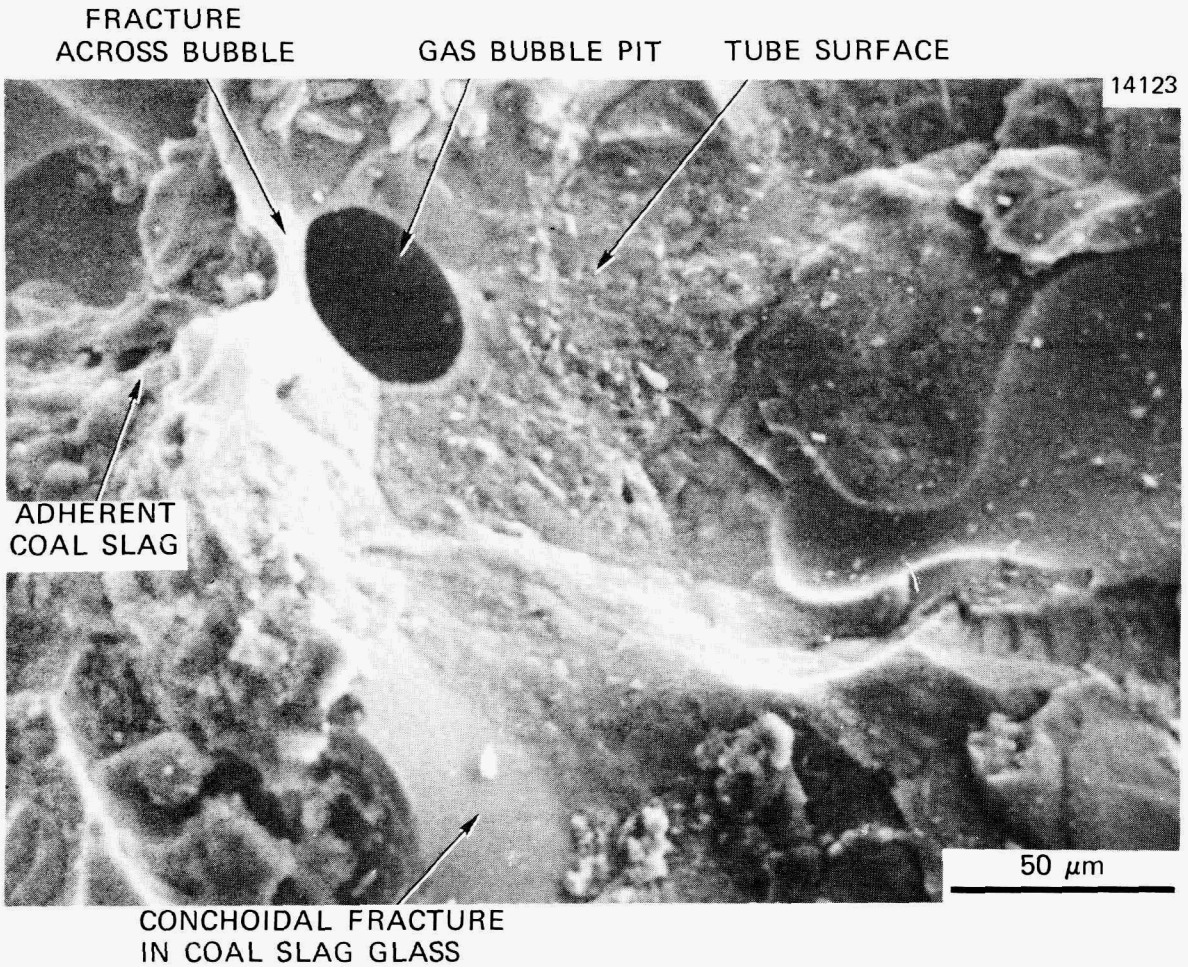

Fig. 34. Scanning electron micrograph of upstream side of exposed KT SiC tube showing site of gas bubble, remnant coal slag glass, and tube surface.

CVD SiC

The vendor produced the CVD SiC tubes by depositing the carbide from the reactant gases onto graphite mandrels. The mandrels were subsequently removed to produce freestanding SiC tubes. The microstructures of tube wall sections for both as-received and exposed CVD SiC tubes were very similar, and therefore only those of exposed tubes will be presented and discussed. Figure 35 shows the microstructure of a tube wall on the upstream side after the coal slag was removed. The specimen was etched to

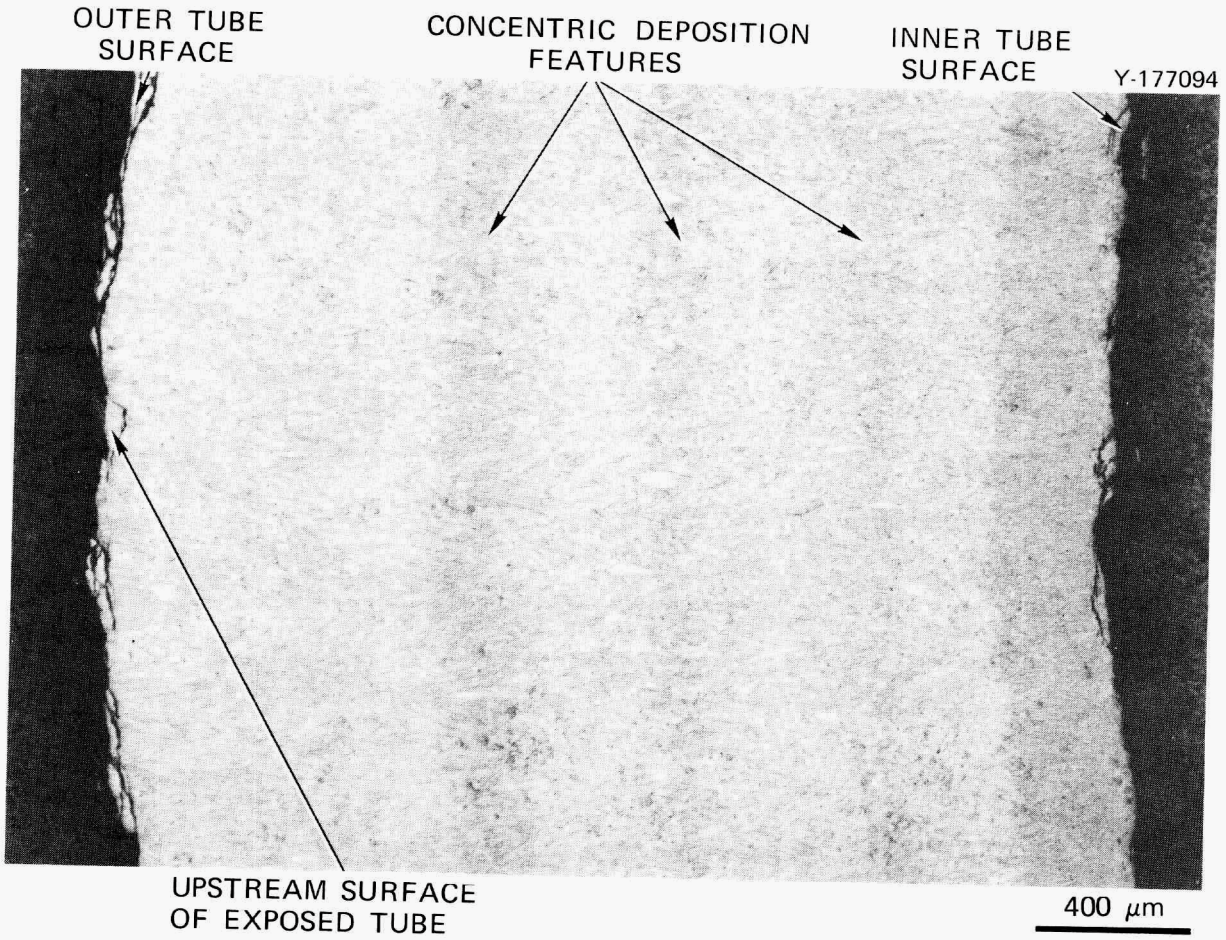

Fig. 35. Microstructure of exposed CVD SiC tube wall, upstream side.

show the SiC grain structure. The tube outer and inner surfaces contain microcracks that extend about 20 μm under the surface. The appearance of these cracks was essentially the same in the as-received and exposed specimens. The texture visible in the microstructure indicates the concentric radial features typical of CVD SiC tubes fabricated by this method.

The wall thickness in the tube, as shown in Fig. 35, following the exposure was essentially identical with the original. Figure 35 also shows that exposure to the coal slag did not result in appreciable corrosion or cracking of the tube. The microstructure of the tube shown in Fig. 36 illustrates the structure of a CVD SiC tube near the upstream surface. Note the circumferential cracks in the tube wall. Such cracks

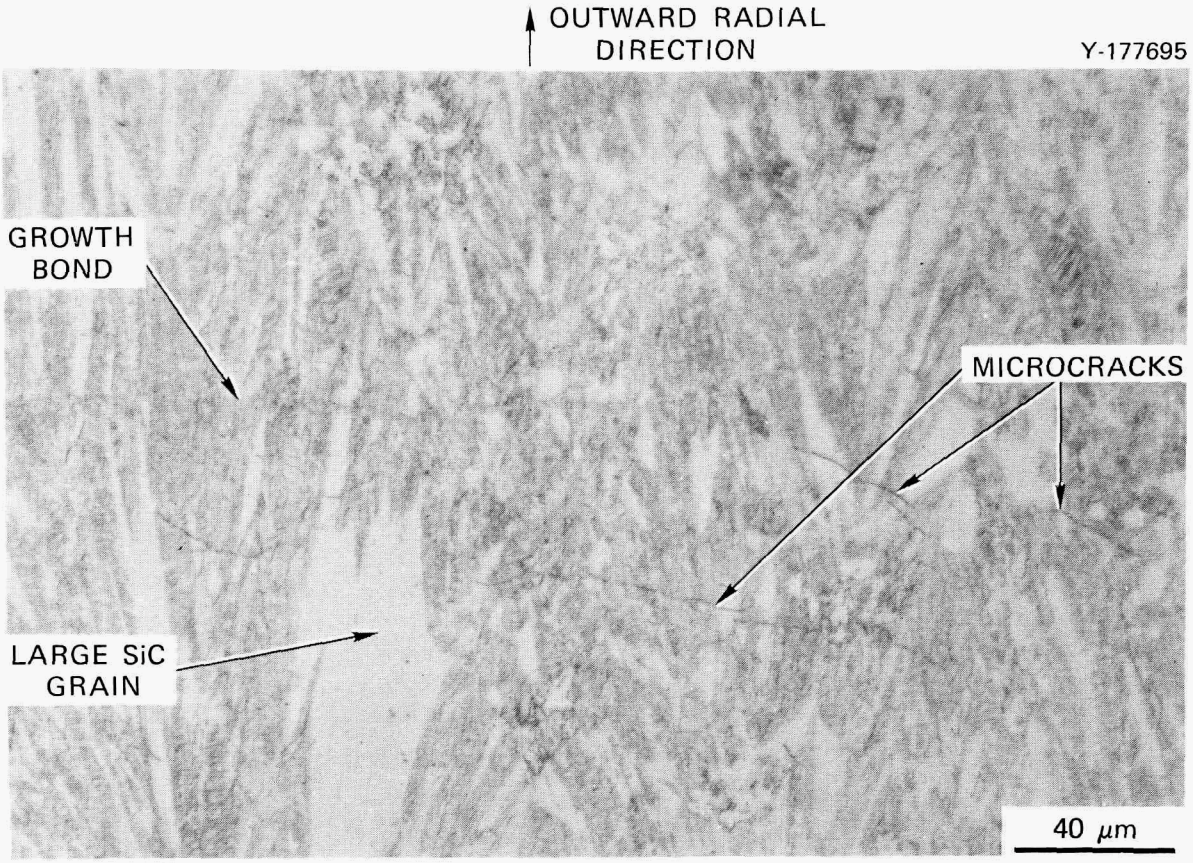

Fig. 36. Microstructure of exposed CVD SiC tube, upstream side, showing circumferential microcracks and growth features.

are characteristic of the CVD SiC tubes examined before and after combustion gas exposure in this test as well as the previous Test 1. The cracks apparently resulted from internal stresses generated in the microstructure by the growth of SiC grains during deposition. The cracks tended to be circumferentially oriented within the tube walls and they occurred more frequently in the outer half of the wall thickness.

X-ray diffraction analyses of the as-received ceramic tube revealed a highly faulted structure, which is identified in Table 11 as α-SiC. The CVD SiC often consists primarily of cubic β-SiC, but if deposition occurs under conditions that produce a high stacking fault density in the beta polymorph, the highly faulted beta structure cannot be distinguished from the hexagonal alpha structure by standard x-ray powder diffraction methods.

The combustion gas exposure did result in the appearance of graphite or carbon graphitized sufficiently to provide measurable diffraction intensity for interplanar spacings characteristic of graphite in the upstream surface and upstream subsurface specimens. The size of these graphitic regions was apparently relatively small, because they could not be detected in the metallography specimens. Several low-intensity diffraction lines were observed in the upstream surface specimen that could not be identified either with SiC polymorphs or with the graphite structure. These lines had intensities between 1 and 9% of the intensity of the SiC line at about 0.25 nm. The interplanar spacings of these lines were 0.497, 0.294, 0.291, 0.283, 0.278, and 0.2705 nm.

In summary, long-term exposure of the CVD SiC tubes to the coal slag did not result in significant corrosive degradation. Microcracks that are typically observed in massive CVD SiC were present in both as-received and exposed tubes, and these were oriented circumferentially, as discussed previously. No slag penetration into such cracks was observed.

Sintered α-SiC

The microstructure of sintered α-SiC tubes used in this experiment consisted of grains of α-SiC having sizes from about 20 to 30 μm, graphitic inclusions smaller than 1 μm, and lamellar voids whose smallest dimensions were generally oriented parallel to the tube radius. Examples of the microstructure of this material in the as-received condition, including one of the voids, are shown in Fig. 37. Figure 37(a), which is a bright-field micrograph of an unetched polished cross section, shows the small bright metallic inclusions and the large graphitic inclusions. Figure 37(b) shows a void-type defect observed in the walls of the tubes, as viewed perpendicular to the tube axis. These voids typically had an elongated dimension in the direction of the tube axis. An example of this geometry from an exposed tube is shown in Fig. 38. Note that the microstructure of the exposed α-SiC appears to be identical with that of the as-received material in Fig. 37(b).

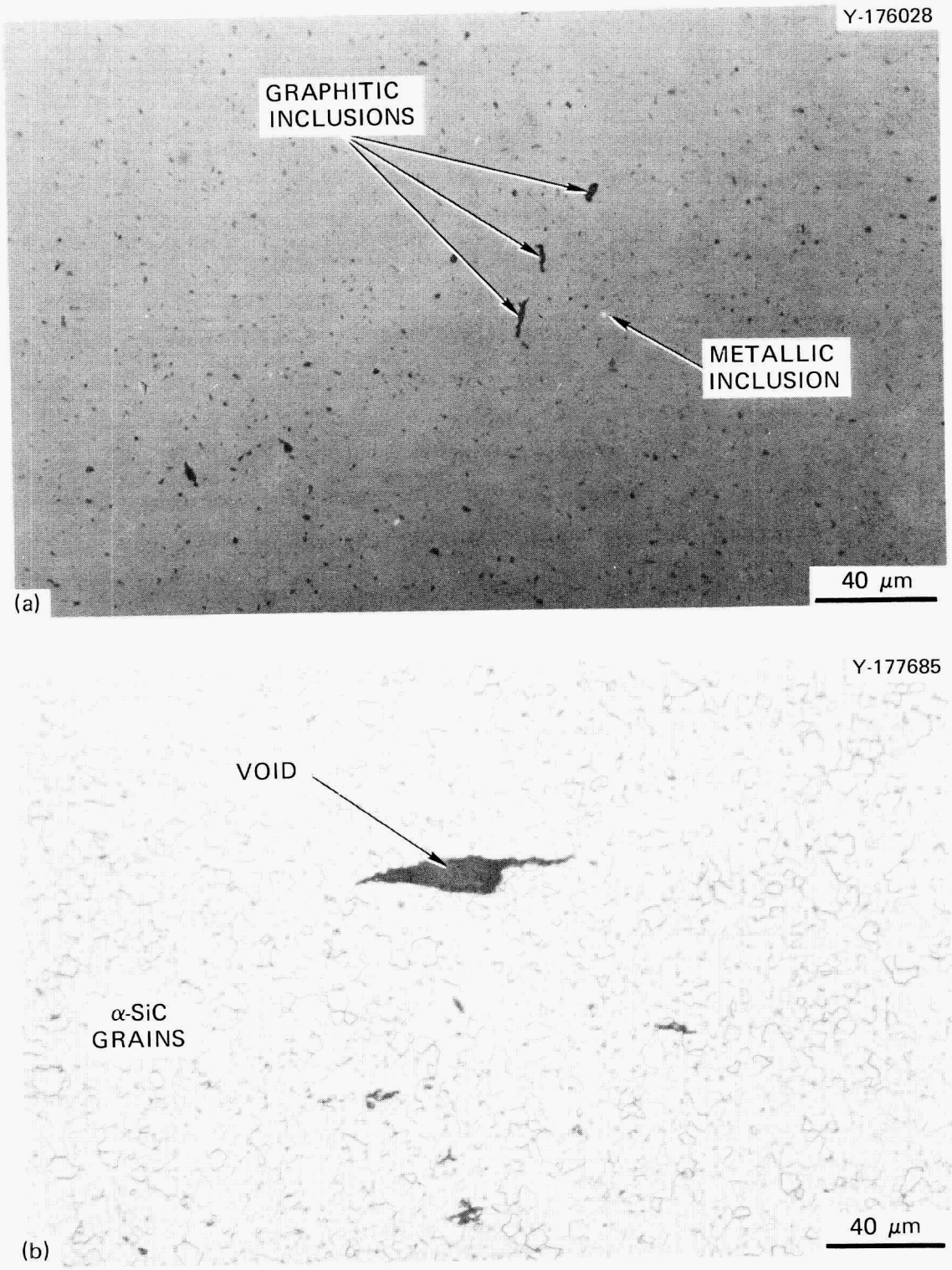

Fig. 37. Bright-field micrographs of as-received α-SiC tube. (a) As polished, showing metallic and graphitic inclusions. (b) Etched, showing void defect in plane perpendicular to tube axis.

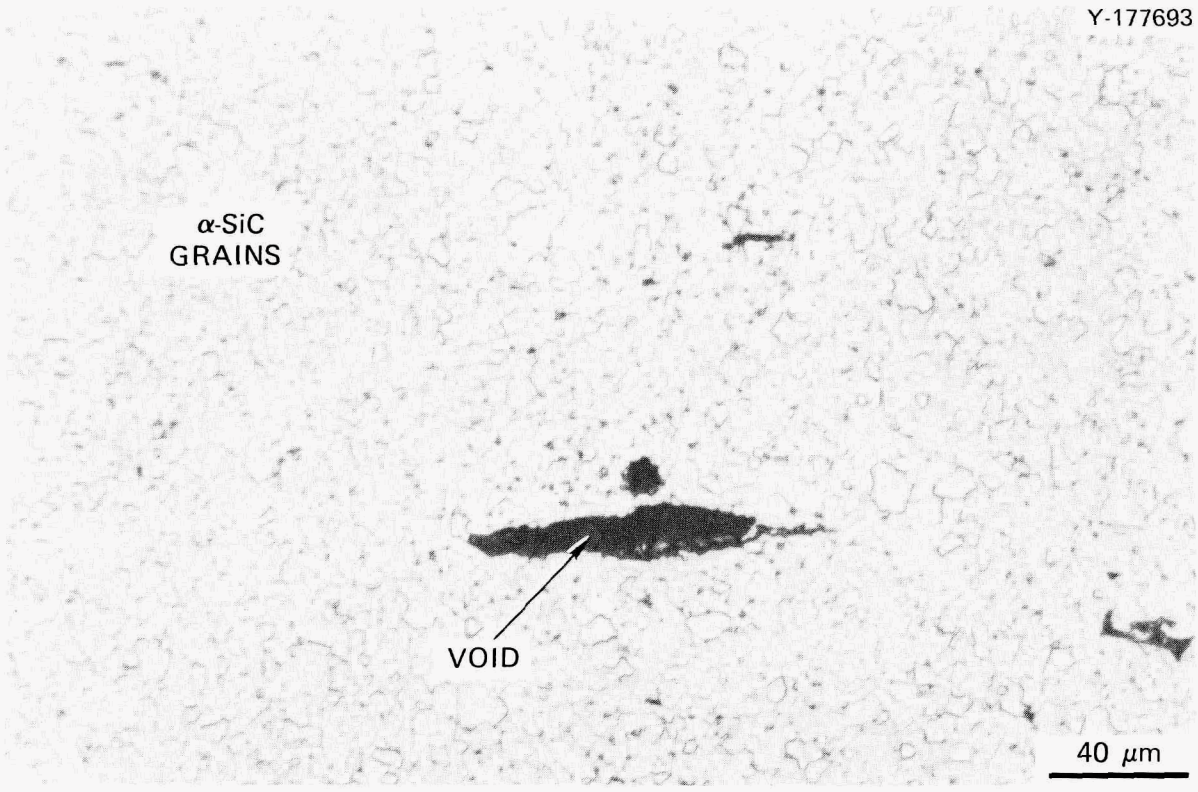

Fig. 38. Void defect in wall of exposed α-SiC tube in plane parallel to longitudinal axis.

In summary, the microstructure of the α-SiC tubes as determined optically consisted of SiC grains having maximum dimensions up to about 30 μm, graphitic inclusions with dimensions of about 1 μm or less, metallic inclusions with dimensions much less than 1 μm, and relatively large voids having major dimensions of about 100 μm and minor dimensions of about 20 μm. The microstructure did not undergo any obvious change during the exposure to coal slag. The α-SiC grains in both the as-received and exposed material were generally irregular in shape.

Scanning electron microscopy was used to identify the nature of the coal slag interface on the outer surface of the tubes. Figure 39 shows remnants of the slag on the upstream surface of an α-SiC tube, including an area where the slag fractured rather cleanly from the SiC. The remnant slag contains the blocky crystals discussed previously, and the edge of the slag at its junction with the tube surface exhibited the conchoidal

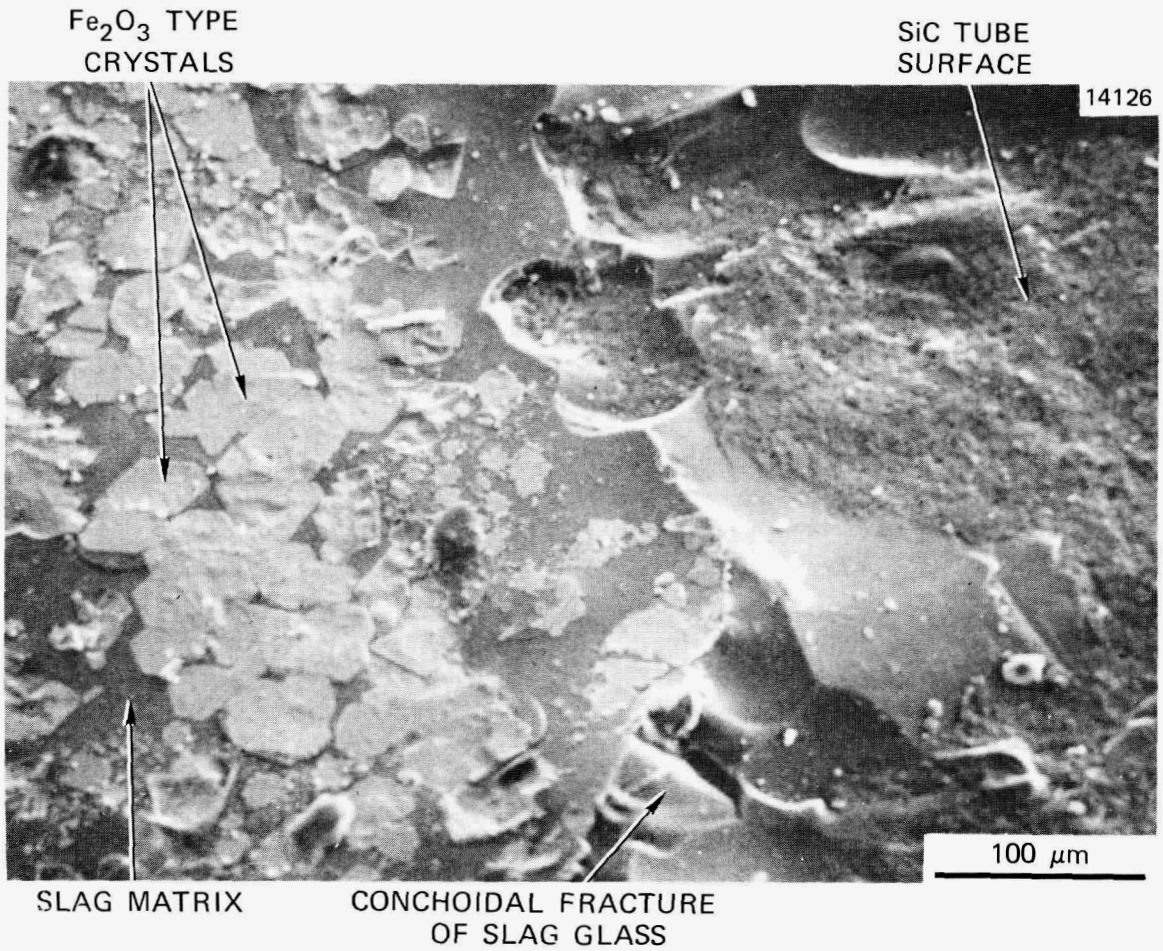

Fig. 39. Structure of coal slag on upstream side of exposed α-SiC tube, showing iron oxide type crystals with similar orientations near tube surface.

fracture typically observed in glasses. Examination of the slag-SiC interface on the exposed tubes at higher magnification in the SEM revealed a network of small cracks in the slag glass very close to the tube surface. An example of the cracks is shown in Fig. 40. The cracks appear to be characteristic of the slag located near the tube surface on all the SiC-based tubes employed in this experiment. We postulate that the crack system visible in Fig. 40 was produced by stresses produced during cooling of the tubes from the exposure temperature and resulted from thermal expansion mismatch between the slag glass and the SiC ceramics. The extensive microcracking at the slag-SiC interface would result in a

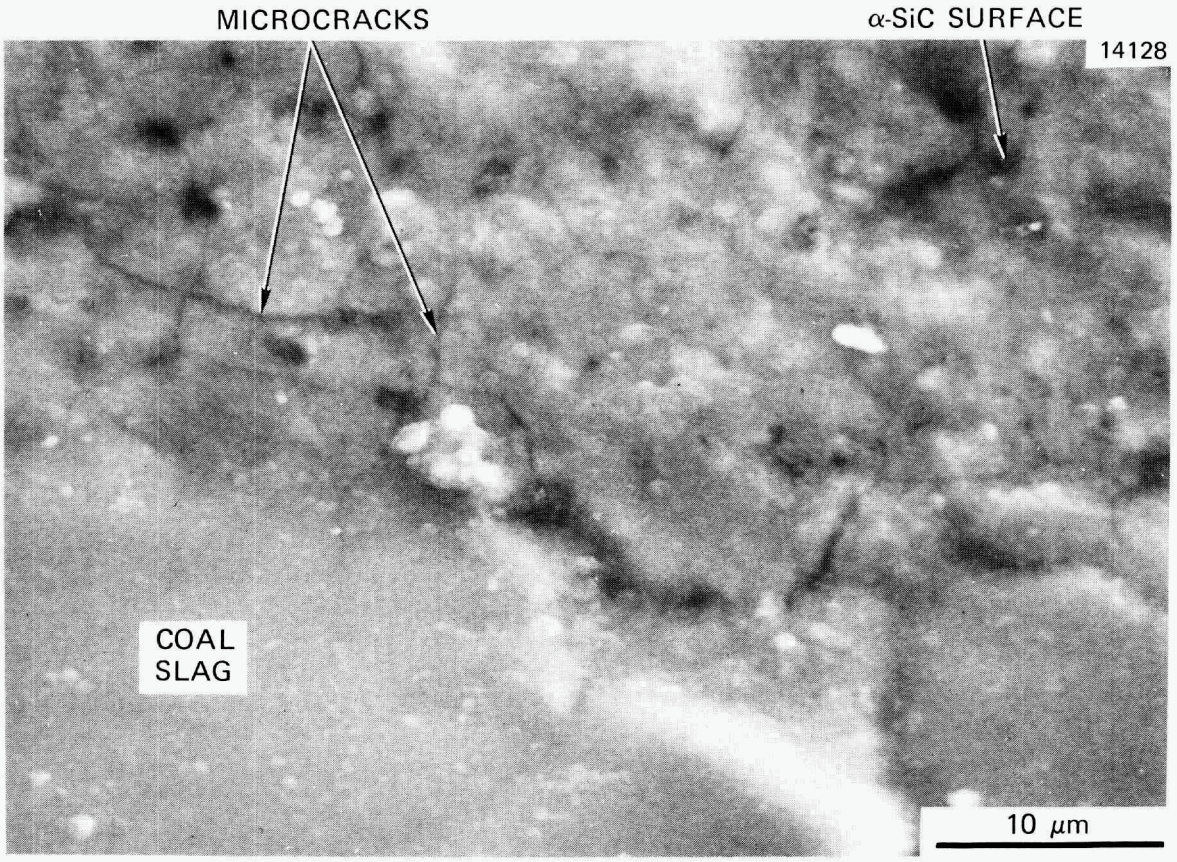

Fig. 40. Microcracks in slag at slag-SiC interface in exposed α-SiC tube.

relatively weak mechanical bond and may explain the relative ease with which the solidified slag could be removed from the SiC tubes. The slag deposited on both alumina and sialon tubes developed a much stronger mechanical bond with the ceramic, and the resulting stresses during cooldown probably resulted in the extensive fracturing observed in these materials.

GE 128 Sialon

The microstructure of the as-received sialon was very inhomogeneous. For example, a low-magnification examination revealed large grains within the bulk of the material. These grains, which are shown in the cross-sectional view of the tube wall in Fig. 41, may have represented remnants

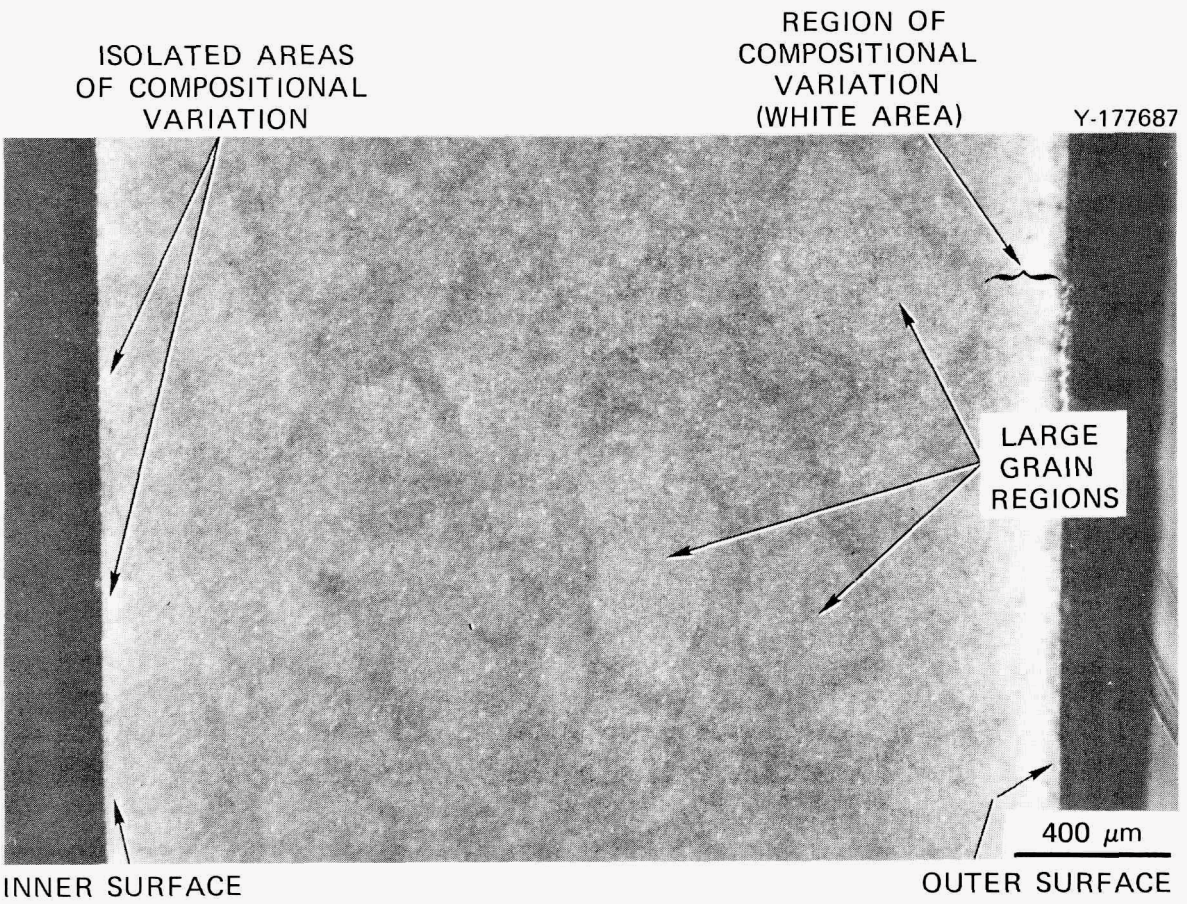

Fig. 41. Cross section of as-received sialon tube showing large internal grain structure and compositional variation along outer and inner surfaces.

of the initial particles used in the fabrication process. Also these grains could have been regions in which the sialon solid solution was varied slightly. An additional compositional variation approximately 50 μm in thickness was also observed near the outside surface of the sialon tube. This compositional variation appears as the white regions in Figs. 41 and 42. Furthermore, Fig. 41 reveals small isolated quantities of the white phase along the inner surface.

The structural differences between the inner and outer surfaces of the as-received tube were further investigated with the SEM. The resulting micrographs, which illustrate typical regions on the inner and outer surfaces, are shown in Figs. 43 and 44, respectively. The particles

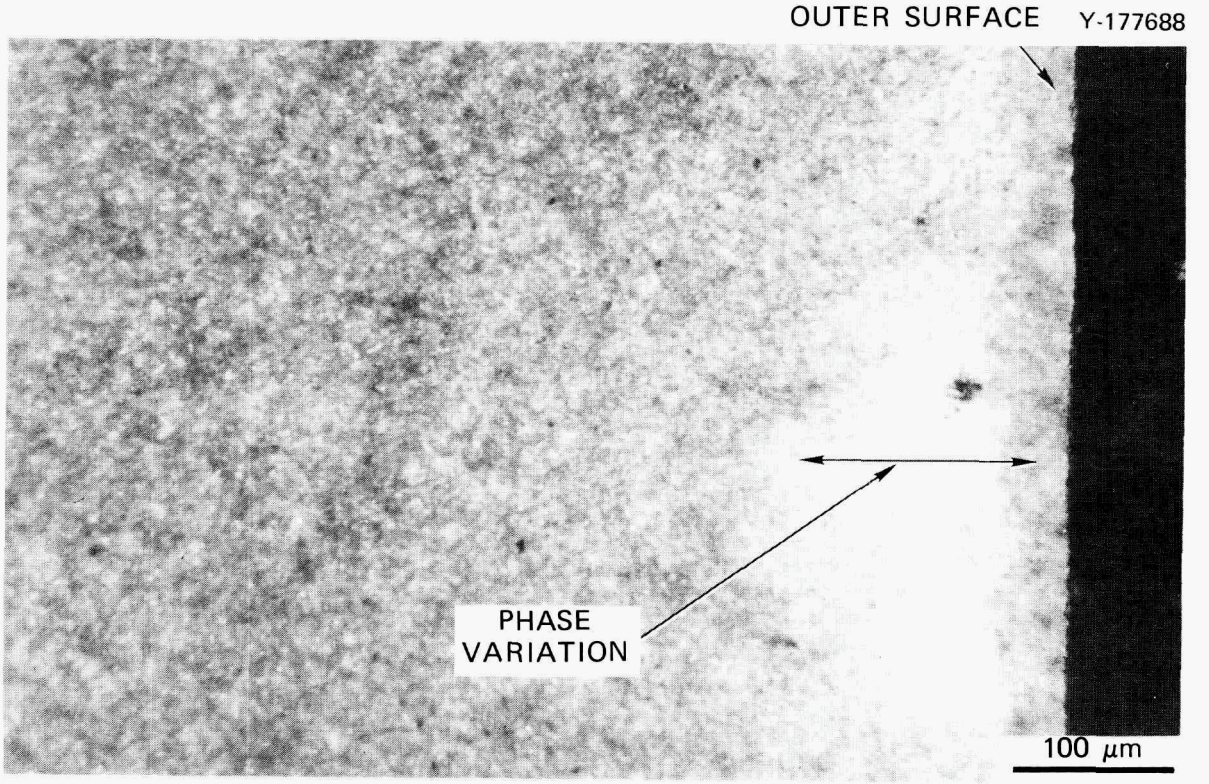

Fig. 42. Phase variation of outer surface region of as-received sialon.

along the inner surface had a platelet morphology that is similar to that exhibited by β-Si_3N_4. An energy-dispersive x-ray analysis of the inside surface indicated that the major elements and their relative peak intensities were as follows: Mg, 1.0%; Al, 100%; Si, 37.5%; Ca, 1.3%; and Fe, 0.8%. The rounded appearance of the particles along the outer surface (Fig. 44) suggests that the sharp discontinuities associated with the initial platelet morphology were partially destroyed as a result of either viscous flow or possibly an oxidation reaction occurring during the thermal treatment of the green-state sialon tube. In fact, the appearance of the outer surface was reminiscent of a highly oxidized β-Si_3N_4 ceramic. Therefore, in the fabrication of the sialon material, differences in the firing temperature and environment between the inside and outside surfaces could have led to a variation in the respective oxidation behavior and, thus, the surface morphology. Finally, the energy-dispersive x-ray

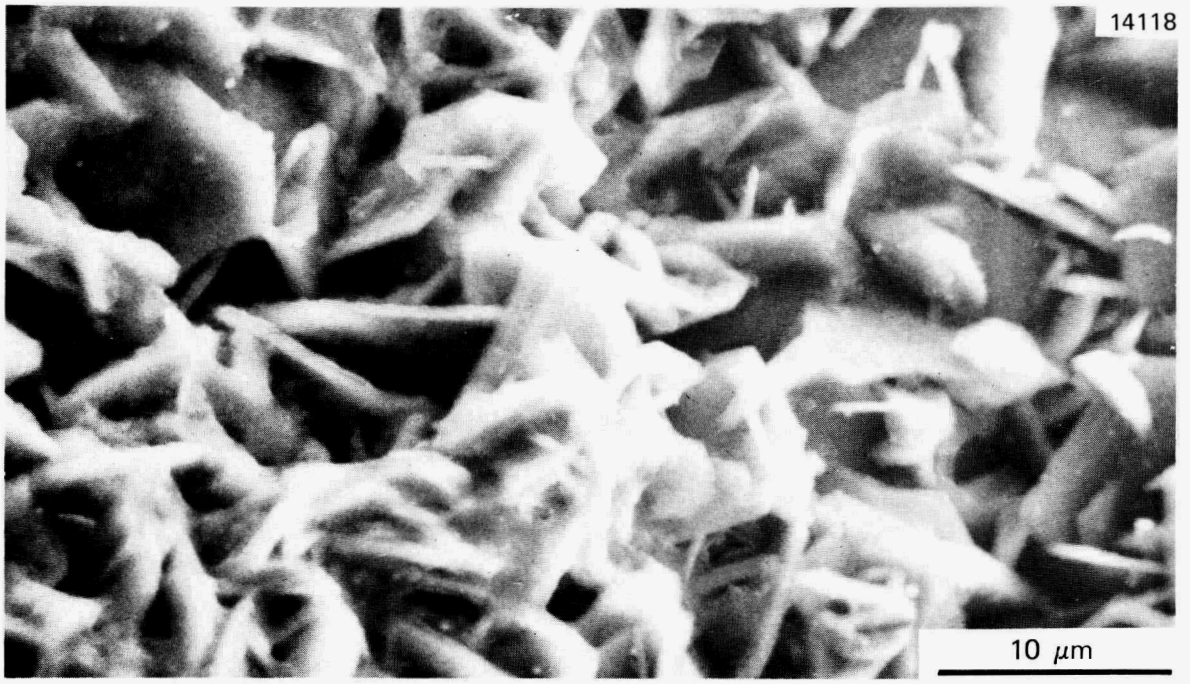

Fig. 43. Scanning electron micrograph of inner surface of as-received sialon, showing platelike morphology.

Fig. 44. Scanning electron micrograph of outer surface of as-received sialon, showing more rounded particle morphology.

analysis of the outer surface indicated that the concentrations of Mg, Al, Fe, and Ca were greater and the Si concentration was slightly less when compared with the respective concentrations along the inner surface.

Further SEM examinations of a polished cross section of the as-received sialon revealed at least two types of isolated phases within the bulk material. These are shown in Fig. 45, which is an area located approximately halfway between the inner and outer surfaces. An energy-dispersive x-ray analysis of the two phases and the bulk material revealed insignificant differences in the relative amounts of magnesium, aluminum, and silicon. However, the iron content in region 2 (white phase) was much smaller than that in either region 1 or the bulk material. It is also interesting that within the interior of the sialon tube the silicon concentration was considerably greater than the aluminum concentration. This sharply contrasts with the relative concentrations of aluminum and silicon measured on the inner and outer surfaces. Finally, Fig. 45 shows some evidence that the dark phase (region 1) represented subsurface porosity. The existence of such porosity has been described.[7]

The microstructural characteristics along the inner and outer surface regions of the polished cross section were considerably different from those shown in Fig. 45. For example, the size of the isolated white phase (region 2) was much smaller in the areas adjacent to the tube surfaces. This is demonstrated in Fig. 46, which is an area near the outer surface of the sialon tube. Figure 46 also reveals the presence of a substantial amount of dark phase (region 3) having a plate-type morphology. This phase, which was also present in very limited concentrations along the inner surface, was presumably responsible for the platelet structure observed earlier along the inner and outer surfaces (Figs. 43 and 44, respectively). It may have also been related to the white phase observed in the optical micrographs (Figs. 41 and 42). Once again, the SEM elemental analysis did not reveal any significant differences in the Al, Si, Fe, and Mg concentrations between these phases and the bulk material.

In an attempt to distinguish the chemical composition of the constituents present in the as-received sialon, x-ray diffraction patterns were obtained for the inner and outer surfaces. The results that are outlined in Table 11 indicate that a number of chemical compounds including β-Si_3N_4, $Si_3Al_{2.67}N_4O_4$, β'-sialon, Mg-sialon(6H) were present along the

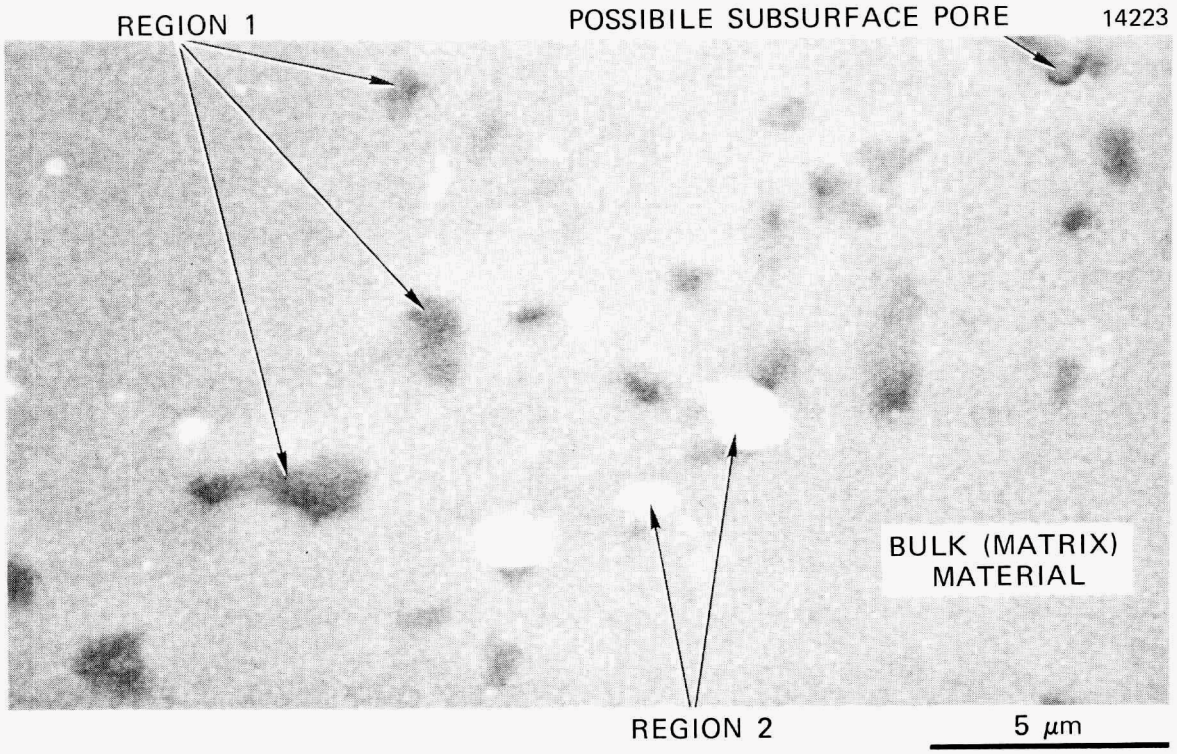

Fig. 45. Cross-sectional scanning electron micrograph of as-received sialon, showing phases present within the tube interior.

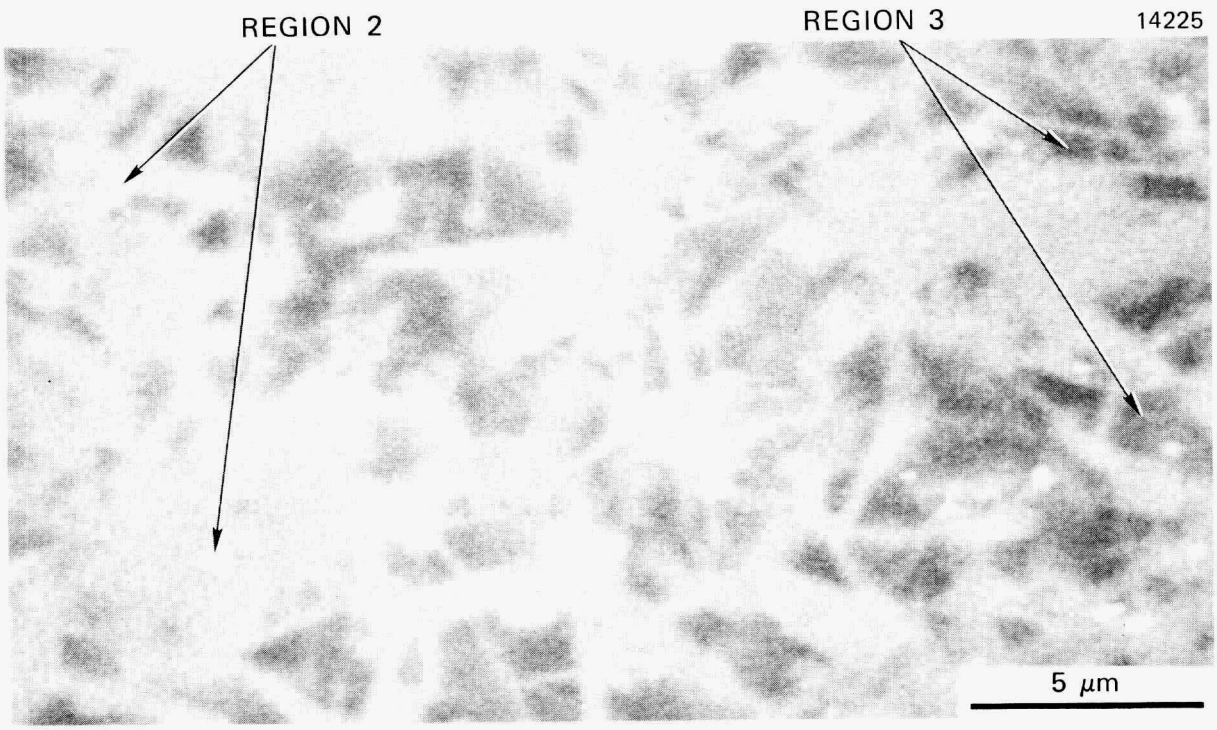

Fig. 46. Scanning electron micrograph of polished cross section of outer surface region of pretest sialon.

inner and outer surfaces of the sialon tube. Furthermore, the existence of several unidentifiable d-spacings associated with the outer surface diffraction trace suggests that one or two additional phases were present in this region. These phases may have been responsible for the microstructural variation between the two tube surfaces. It should be pointed out that several factors complicated identification of the chemical constituents associated with the sialon material. First, the x-ray data that were available for identification were limited to very specific specimen compositions. Consequently, we could not account for all the possible solid solution compositions. Second, the apparent variations in chemical homogeneity observed throughout the sialon (Figs. 41 through 44) probably increased the variance of the associated d-spacings, thus making identification more difficult.

As previously stated, the coal slag that deposited upon all tubes during CRAF Test 2 was strongly bonded to the sialon. Metallographic examinations of the exposed sialon suggested that the actual bonding occurred between an oxide layer approximately 150 μm in thickness, which formed on the outside of the tube during the exposure, and the coal slag. The nature of this bonding is shown in Fig. 47, which is an upstream cross section of the exposed sialon tube. This oxide layer, which was similar to that formed on the sialon during laboratory oxidation experiments, was apparently related to the microstructural inhomogeneites in the outer tube surface of the as-received sialon (the white phases in Figs. 41 and 42). This was further confirmed by the limited oxidation observed along the inside surface of the tube, which in the as-received condition was more homogeneous. Figure 47 also reveals a reaction zone between the slag and oxide layer. As discussed in a subsequent section, the formation of this intimate bonding during the high-temperature exposure may have resulted in thermomechanical stresses upon cooldown to ambient temperature. Such stresses were probably responsible for the extensive cracking observed in the exposed sialon.

The oxidation of the sialon and the subsequent oxide-slag reaction were also observed in the downstream region of the exposed material. However, small differences existed between the upstream and downstream microstructures. For example, the porosity that occurred throughout the

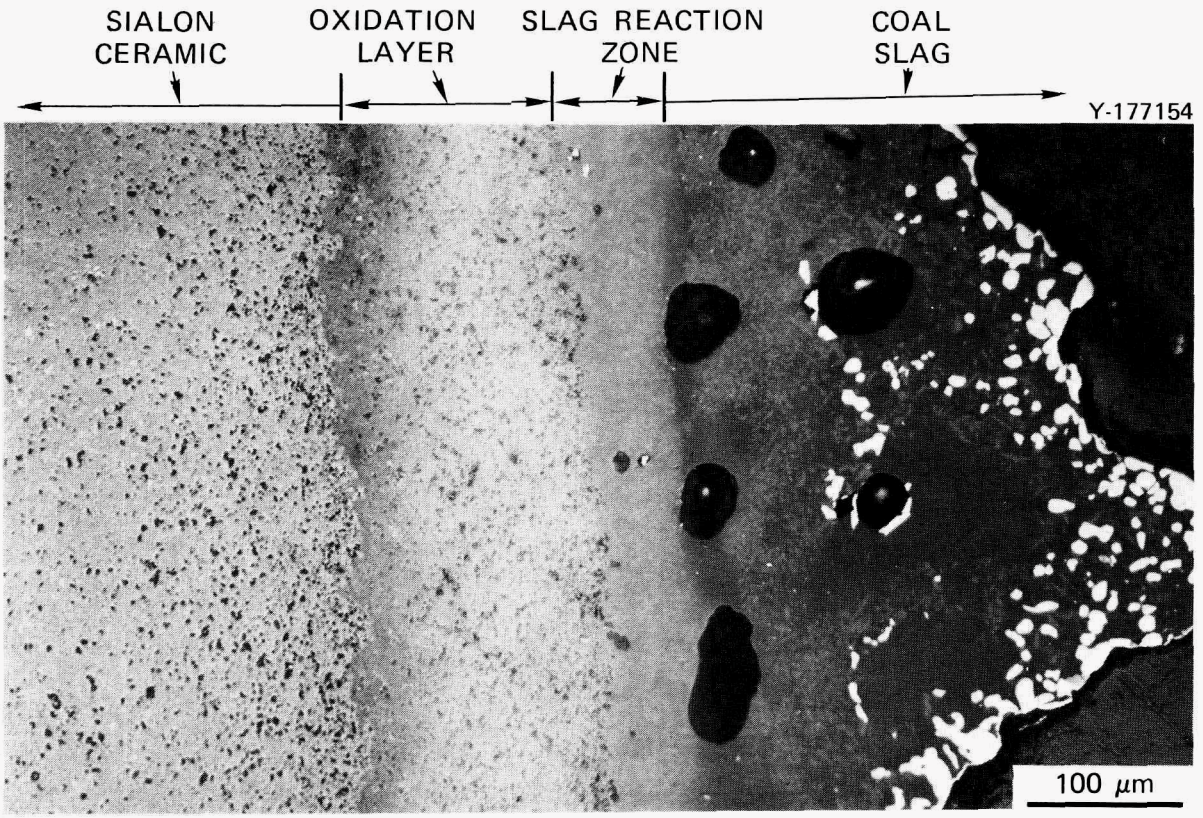

Fig. 47. Various reaction layers in upstream region in exposed sialon.

upstream oxide layer was generally limited in the oxide layer on the downstream side. This is illustrated by the scanning electron micrographs of the upstream and downstream regions shown in Figs. 48 and 49, respectively. Several individual pores in the upstream oxide layer are also shown at higher magnification in Fig. 50. The internal structure exhibited by the larger pore is somewhat reminiscent of the platelike morphology of the dark phase (region 3) observed in Fig. 46. Therefore, during CRAF Test 2 the platelike component in the upstream region may have been preferentially removed as a result of the oxidation process or reaction with the chemical constituents in the coal slag. However, the reasons for the reduced porosity on the downstream side of the tube are unknown. The microstructural characteristics of the coal slag in the upstream region differed significantly from those in the downstream deposit. These differences, which were typical for the slag on all five

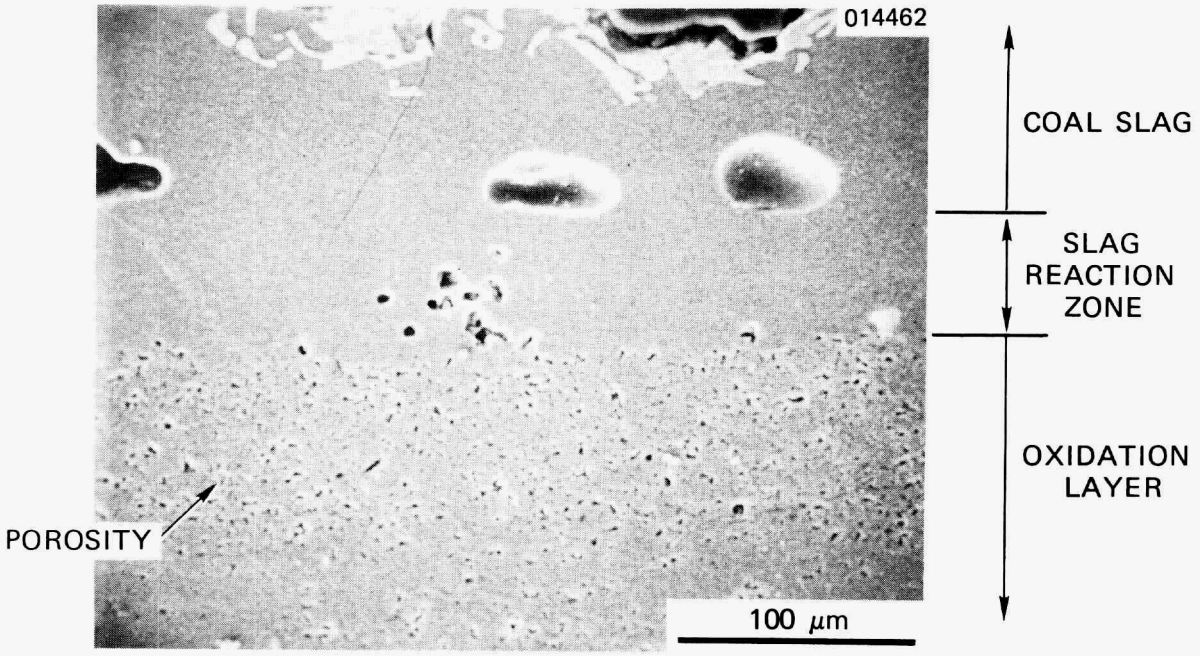

Fig. 48. Scanning electron micrograph of upstream region in exposed sialon, illustrating considerable porosity in oxide layer.

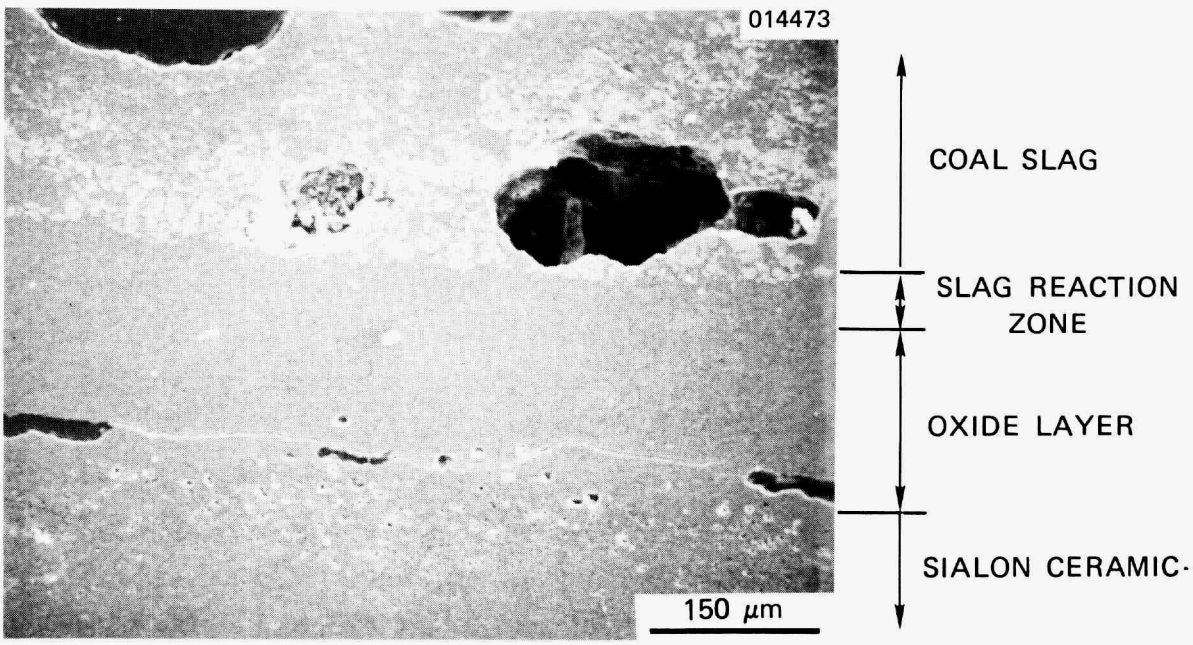

Fig. 49. Scanning electron micrograph of downstream region in exposed sialon, illustrating low porosity in oxide layer.

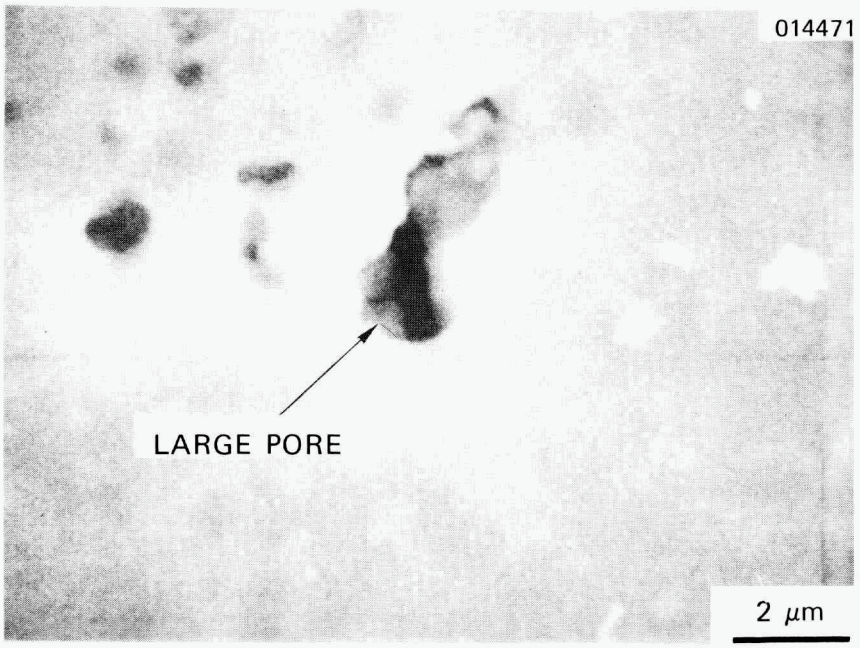

Fig. 50. Scanning electron micrograph of upstream pores in exposed sialon oxidation layer, showing internal platelike morphology.

ceramic materials, are discussed in more detail later. Finally, it should be mentioned that no significant changes occurred within the interior of the sialon ceramic as a result of the exposure to the coal combustion products.

It is interesting that in Figs. 48 and 49 the boundaries between the slag matrix, oxidation layer, and unoxidized sialon ceramic cannot be readily distinguished. In fact, the positions of the boundaries that are labeled in the scanning micrographs were based on the results of optical microscopy. The lack of boundary definition suggests that the elemental compositions in these regions were quite similar. This was further confirmed by the energy-dispersive x-ray analyses, which revealed no substantial variations in the concentrations of the major elements, Si, Al, Fe, and Mg. Futhermore, the concentrations of these four elements were almost identical with those measured earlier in the cross-section view (Fig. 46). Therefore, silicon in the form of SiO_2 probably formed the major component of both the sialon oxidation layer and the coal slag. Also, this similarity in chemical composition likely facilitated the bonding between the slag and oxide phase.

The results of the x-ray analyses of the upstream region of the exposed sialon are included in Table 11. In the studies, the slag was removed so that only the oxide layer remained. Three chemical compounds including α-cristobalite (SiO_2), α-$Mg_2Al_4Si_5O_{18}$, and an aluminosilicate were present in addition to the constituents detected in the outer surface of the as-received material. Therefore, these three compounds were probably associated with the formation of the oxide layer, which is consistent with the detection of significant concentrations of Mg, Al, and Si in the oxide phase by the energy-dispersive x-ray analysis. Separate oxidation studies[6] have also reported the existence of SiO_2 and $Mg_2Al_4Si_5O_{18}$ in oxide films formed on similar sialon materials. The chemical constituents in the exposed subsurface specimen were essentially identical with those found in the as-received material, suggesting that the changes in the sialon resulting from the 496-h exposure were limited to the surface regions.

AD 998 Al_2O_3

The microstructure of the as-received aluminum oxide, which was typical of that used[1] in CRAF Test 1, is illustrated in the SEM micrograph in Fig. 51. The major phase composition (Table 11) was corundum (α-Al_2O_3). As in the case of the sialon, the coal slag that deposited upon the Al_2O_3 materials was strongly bonded to the upstream tube surface. This increased adherence was apparently due to the formation of a 6- to 12-μm-thick boundary, which is shown in the optical micrograph in Fig. 52. The scanning electron micrograph of the upstream region given in Fig. 53 also reveals needlelike crystals in the slag near the Al_2O_3 reaction zone. An elemental x-ray analysis of both intermediate bonding phase and needlelike crystals indicated high concentrations of aluminum, silicon, and iron, with aluminum being the major component. The distribution of these elements at the ceramic-slag interface is further illustrated for the region shown in Fig. 54(a) by the elemental x-ray maps of aluminum, silicon, and iron given in Fig. 54(b) through (d), respectively. Again it is apparent that the reaction zone was predominantly an aluminum-silicon-oxygen compound. In fact, the subsequent x-ray studies of the coal slag suggested

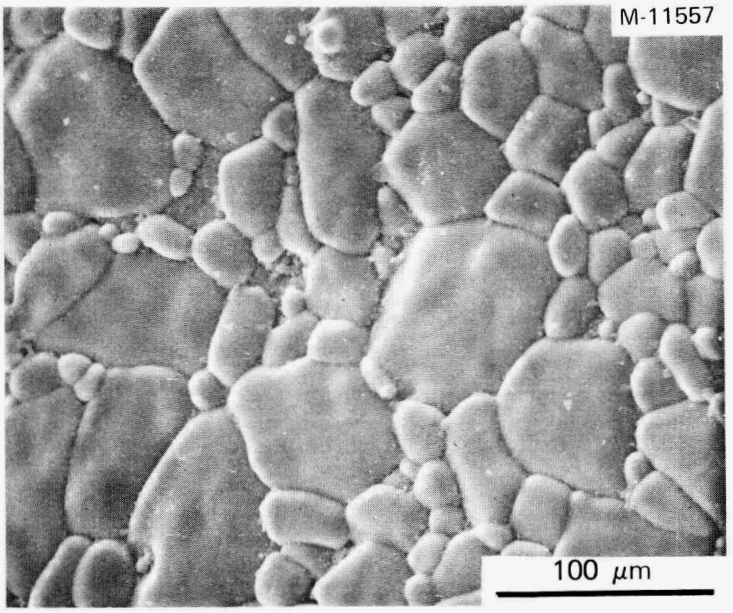

Fig. 51. Surface scanning electron micrograph of as-received alumina, showing typical grain structure.

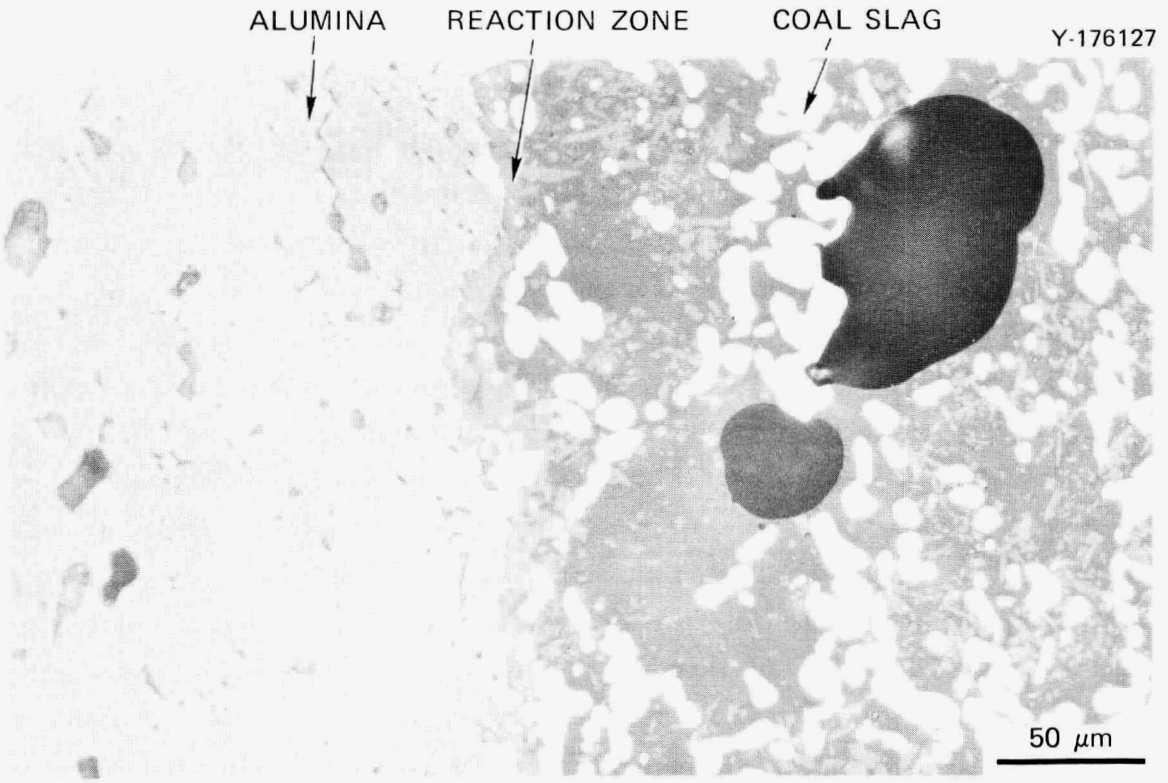

Fig. 52. Optical micrograph of upstream region in exposed alumina, showing presence of reaction zone between coal slag and alumina matrix.

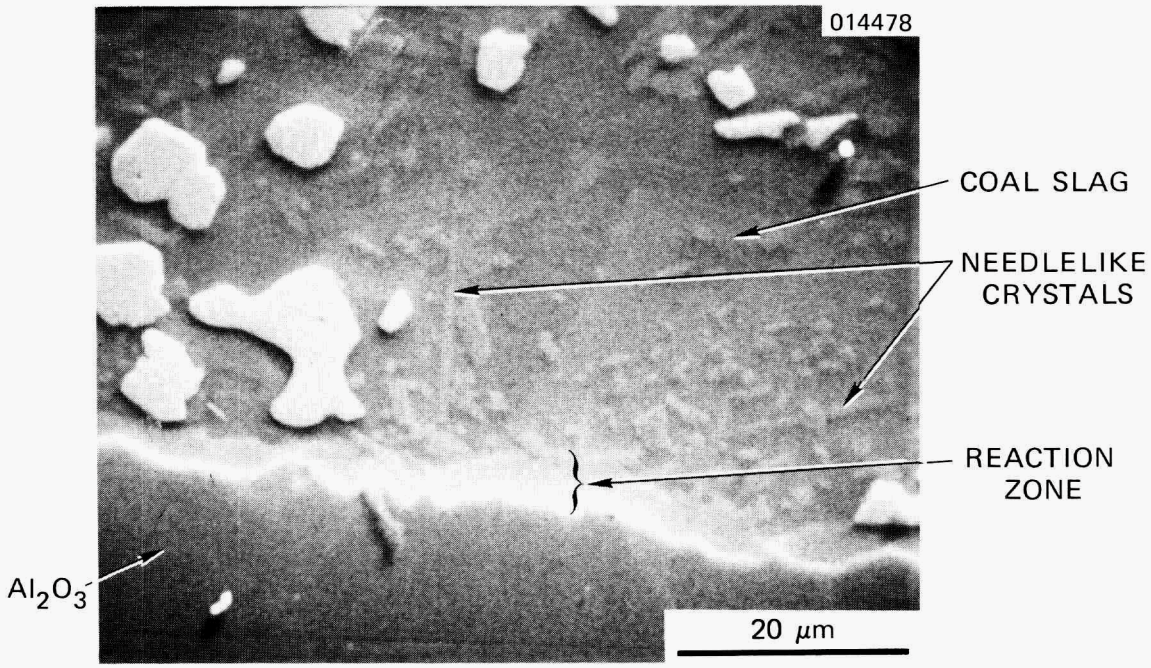

Fig. 53. Scanning electron micrograph backscattered image of upstream region in exposed alumina, illustrating Al_2O_3-slag reaction zone and adjacent formation of needlelike crystals.

that the elongated crystals, which were quite similar in composition to the reaction zone, were composed of some type of aluminosilicate, possibly mullite. Therefore, during the 496-h exposure the coal slag matrix, which contained high concentrations of silicon (in the form of an SiO_2 melt), reacted with the alumina surface to form the aluminosilicate compound. As discussed later, this probably resulted in the formation of thermal stresses upon cooldown due to the thermal expansion mismatch between the alumina and coal slag. Finally, it should be pointed out that the alumina-slag reaction zone was not well developed along the downstream region of the tube. For example, Fig. 55, which is a scanning electron micrograph of the downstream area, reveals only the presence of large irregularly shaped crystals. These were later determined to have high concentrations of iron.

The behavior of the Al_2O_3 in CRAF Test 2 was distinctly different from that observed in CRAF Test 1, in which a 100-μm-thick layer of iron-nickel aluminate formed on the outer surface of the Al_2O_3 tube. In addition,

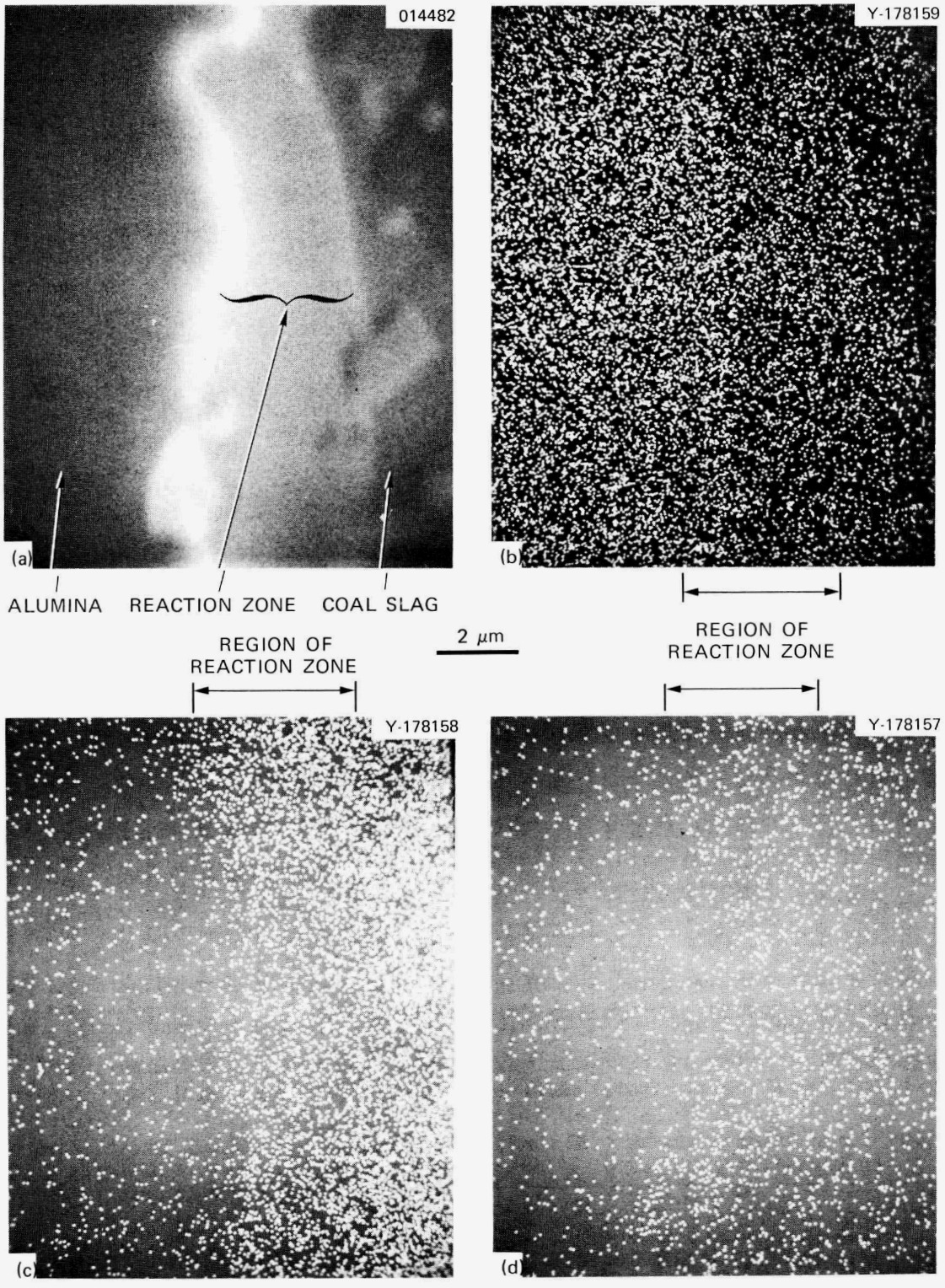

Fig. 54. Distribution of major elements in upstream interfacial region in exposed alumina. (a) Backscatter image. (b) X-ray map for aluminum. (c) X-ray map for silicon. (d) X-ray map for iron.

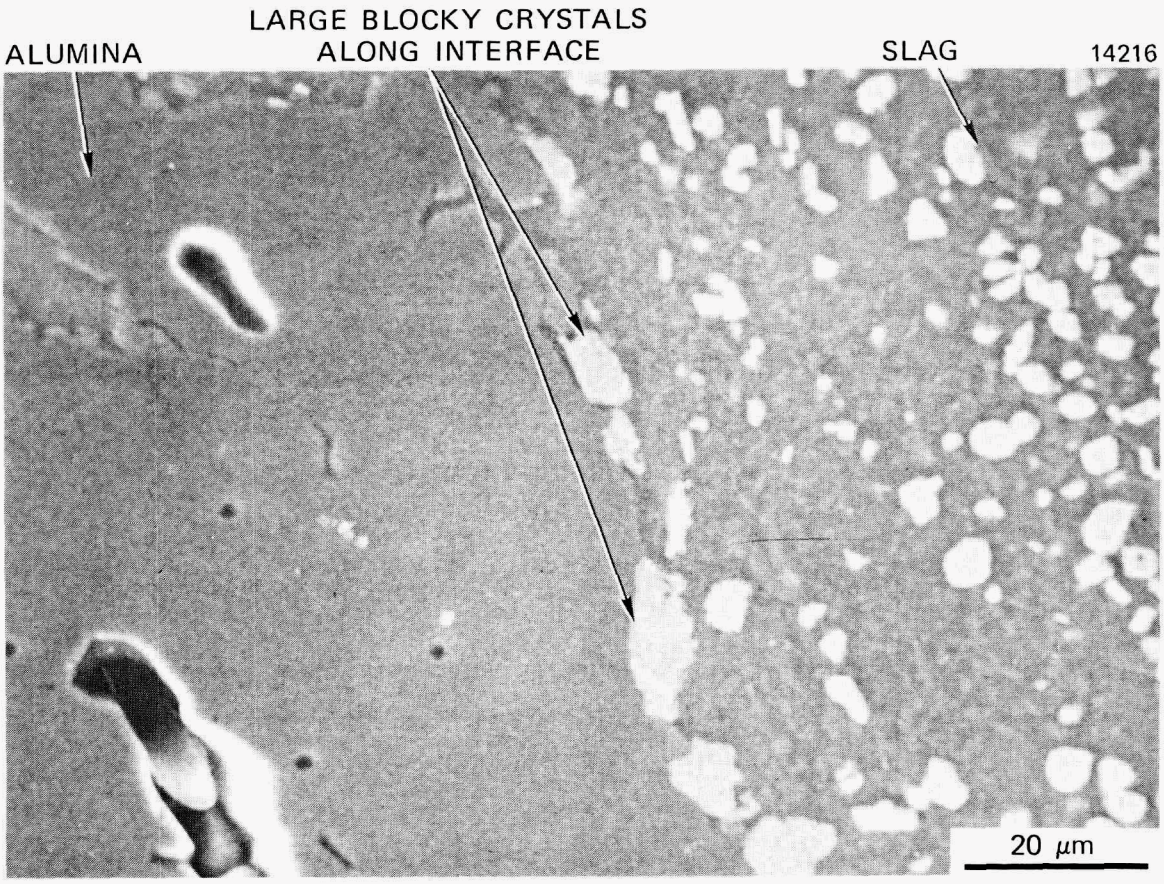

Fig. 55. Scanning electron micrograph of downstream region in exposed alumina.

there was evidence of grain growth in the upstream surface of the exposed Al_2O_3 used in Test 1. A similar analysis of grain size in the exposed alumina used in this study was unsuccessful because of problems with the etchant. However, SEM observations of a fracture surface perpendicular to the slag-alumina interface suggested that no significant grain growth occurred during the exposure.

The x-ray diffraction results (Table 11) indicated that the upstream surface of the exposed alumina contained minor amounts of SiO_2 in the form of either tridymite or α-quartz. These components may represent remnants of the coal slag matrix. Although the energy-dispersive x-ray analyses revealed the presence of an aluminosilicate compound at the alumina

surface, its concentration was apparently too low to be detected by x-ray diffraction. No additional phases other than the α-Al_2O_3 (corundum) were found in the subsurface Al_2O_3 sample.

Coal Slag

Metallographic and SEM observations of the coal slag removed from the upstream surface of various tubes revealed a microstructure consisting of large pores ranging from 42 to 127 μm in diameter and at least two types of crystals dispersed in a glassy slag matrix. These features are designated in Fig. 56(a), which is an optical micrograph of the upstream slag adjacent to the tube surface. The first group of crystals exhibited an irregular and often blocky morphology. In addition, the size of these crystals increased from about 9 μm at the ceramic-slag interface [Fig. 56(a)] to about 23 μm at the other slag surface, which was exposed to the combustion atmosphere [Fig. 56(b)]. In many instances, circumferential cracks were observed in the glassy slag matrix around the largest crystals [Fig. 56(b)]. This cracking, which occurred only when the blocky crystals exceeded a critical size, apparently resulted from a significant thermal expansion mismatch between the slag matrix and crystal. This situation is analogous to microcracking that occurs in polycrystalline materials composed of grains having a large thermal expansion anisotropy.[14–17] Such microcracking also requires that the average grain size exceed a critical value. The second type of crystals present in the slag was much smaller than the blocky type and exhibited a needlelike morphology (Fig. 56). Furthermore, the volume distribution of these elongated crystals was much more uniform than that of the larger irregularly shaped crystals. In fact, the concentration of the latter exhibited abrupt changes within the bulk of the upstream slag. This behavior, which is shown in Fig. 57, may have resulted from variations in the flue gas aerodynamics in the vicinity of the slag surface. These variations probably altered the viscous flow characteristics of the slag at temperature and ultimately led to the observed fluctuations in the volume distribution of large blocky crystals. The fact that the distribution of the elongated crystals was not affected suggests that they were not present during the actual exposure but precipitated out of the slag matrix upon the final cooldown of the CRAF.

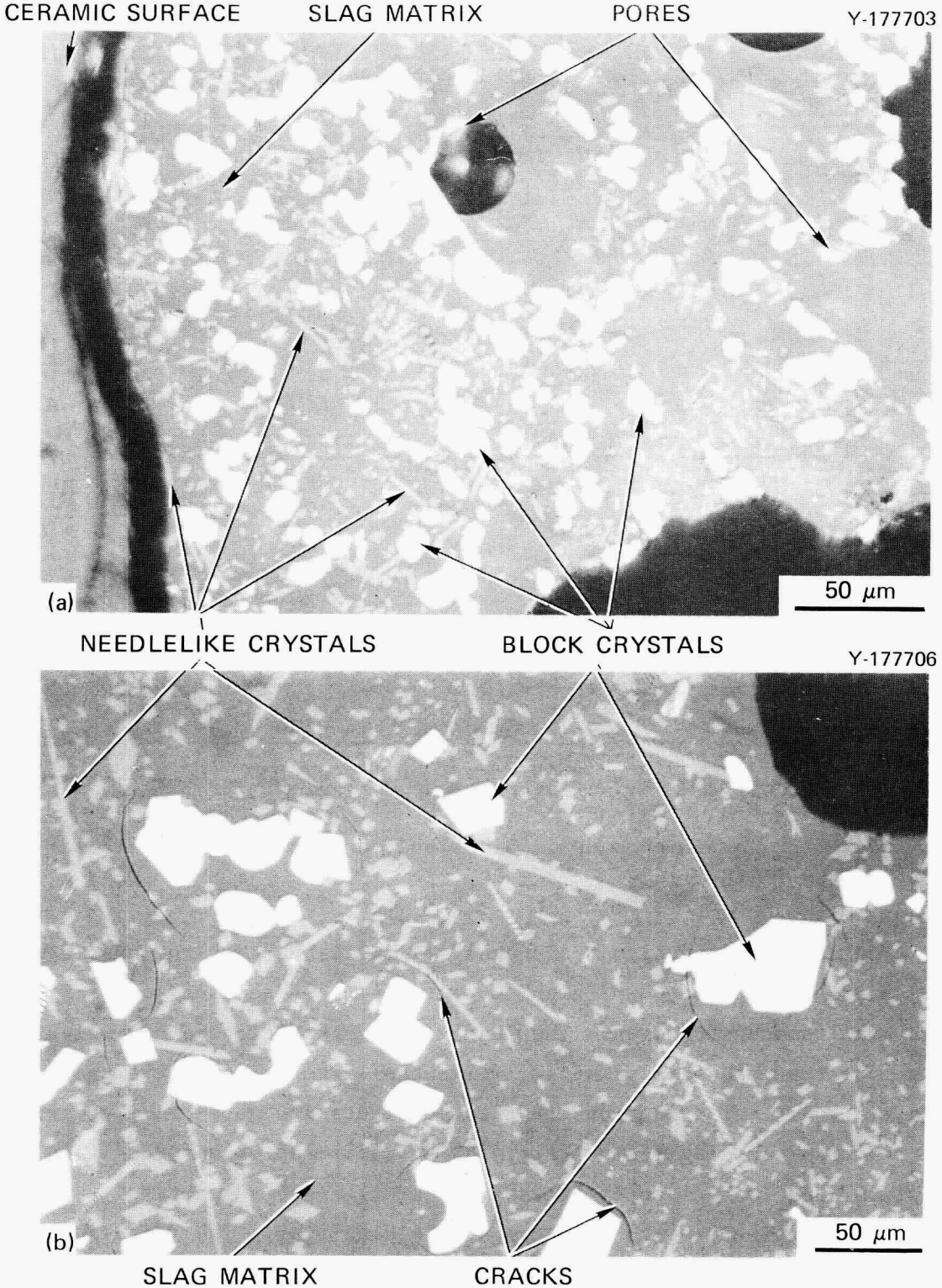

Fig. 56. Cross sections of upstream coal slag. (a) Adjacent to the exposed CVD SiC surface. (This micrograph reveals the features typical of the upstream slag samples removed from all tubes.) (b) Just below surface exposed to the combustion atmosphere.

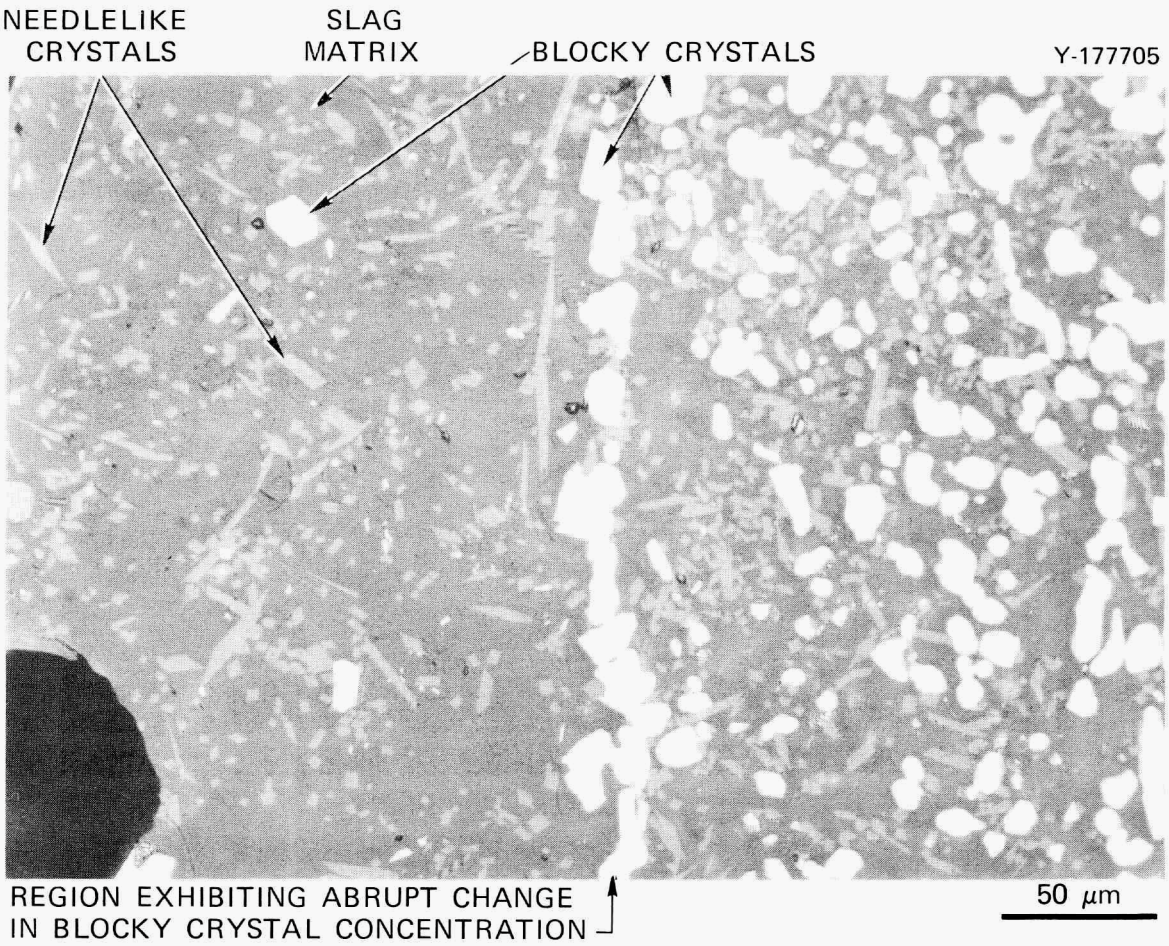

Fig. 57. Abrupt changes in distribution of blocky crystals in upstream coal slag.

The energy-dispersive x-ray analyses indicated that the upstream coal slag matrix was composed of high concentrations of aluminum and silicon with small amounts of iron. The needlelike crystals contained slightly more iron than the glassy matrix, while the larger blocky crystals were iron rich. The distributions of these elements are more clearly defined for the upstream slag region (Fig. 58) by the x-ray maps for silicon, aluminum, and iron given in Fig. 58(b) through (d), respectively. The x-ray diffraction results of the upstream slag (Table 11) revealed several forms of SiO_2 including α-quartz, α-cristobalite, β-cristobalite, and possibly tridymite. These phases may have been present in the glassy slag matrix. In addition, the α-Fe_2O_3 (hematite) and $3Al_2O_3 \cdot 2SiO_2$ (mullite)

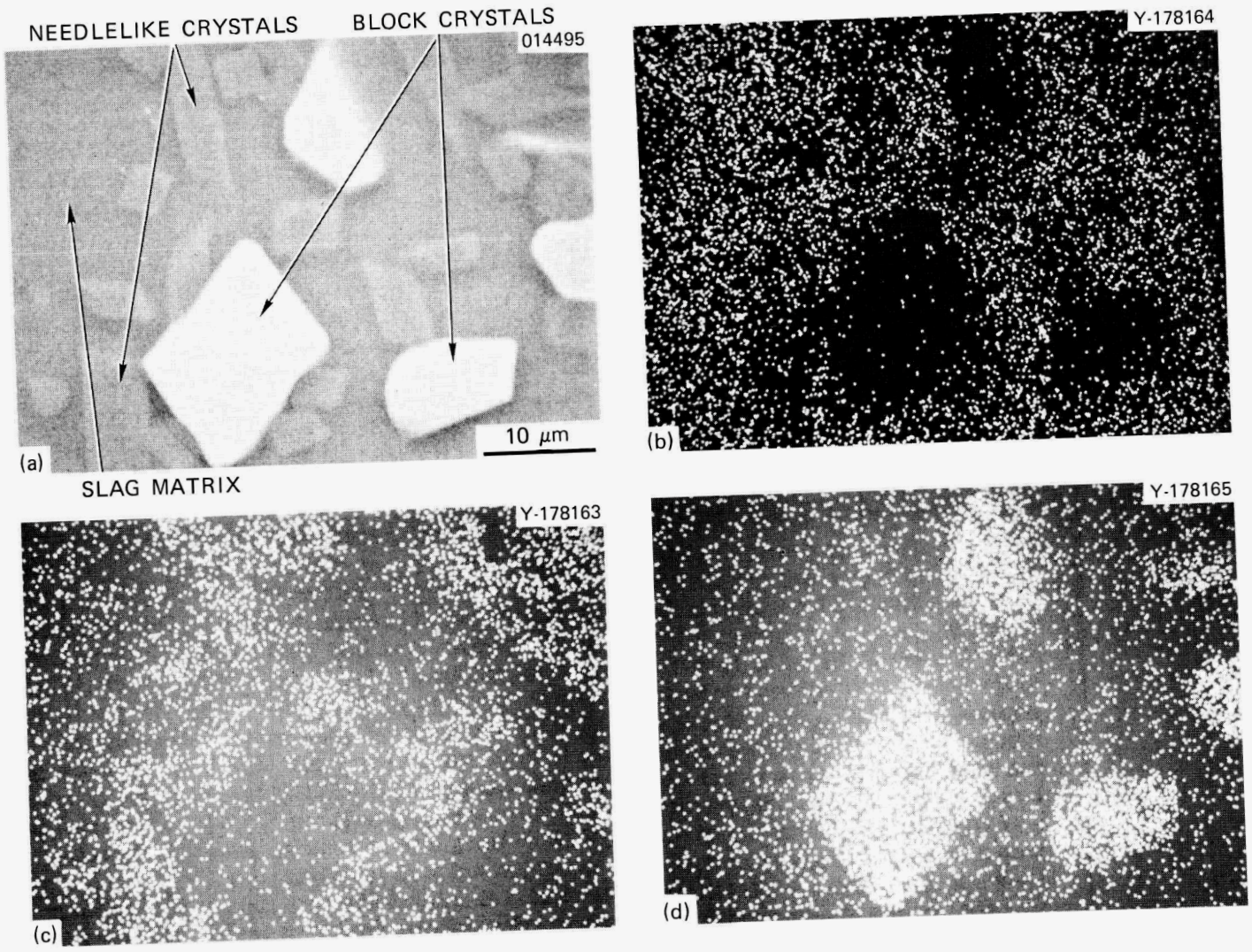

Fig. 58. Typical distribution of major elements in coal slag deposits removed from the exposed ceramic tubes. (a) SEM backscatter image of typical slag region. (b) Elemental x-ray map showing distribution of silicon. (c) Elemental x-ray map showing distribution of aluminum. (d) Elemental x-ray map showing distribution of iron.

probably represented the major constituents in the blocky crystals and needlelike crystals, respectively. The slight displacement of the experimental d-spacings from the published values suggests that some solid solution occurred in these phases. For example, the presence of the $Fe(Al,Cr)O_4$ compound (Table 11) indicates that limited solid solution existed between iron oxide and minor impurities in the slag.

The microstructural characteristics of the downstream slag were distinctly different from those along the upstream portion of the tube. For example, a micrograph of the downstream coal slag remaining on the KT SiC is given in Fig. 59. In general, the crystals present in the glassy slag matrix were poorly developed except near the ceramic-slag interface. Furthermore, the blocklike crystals tended to become smaller

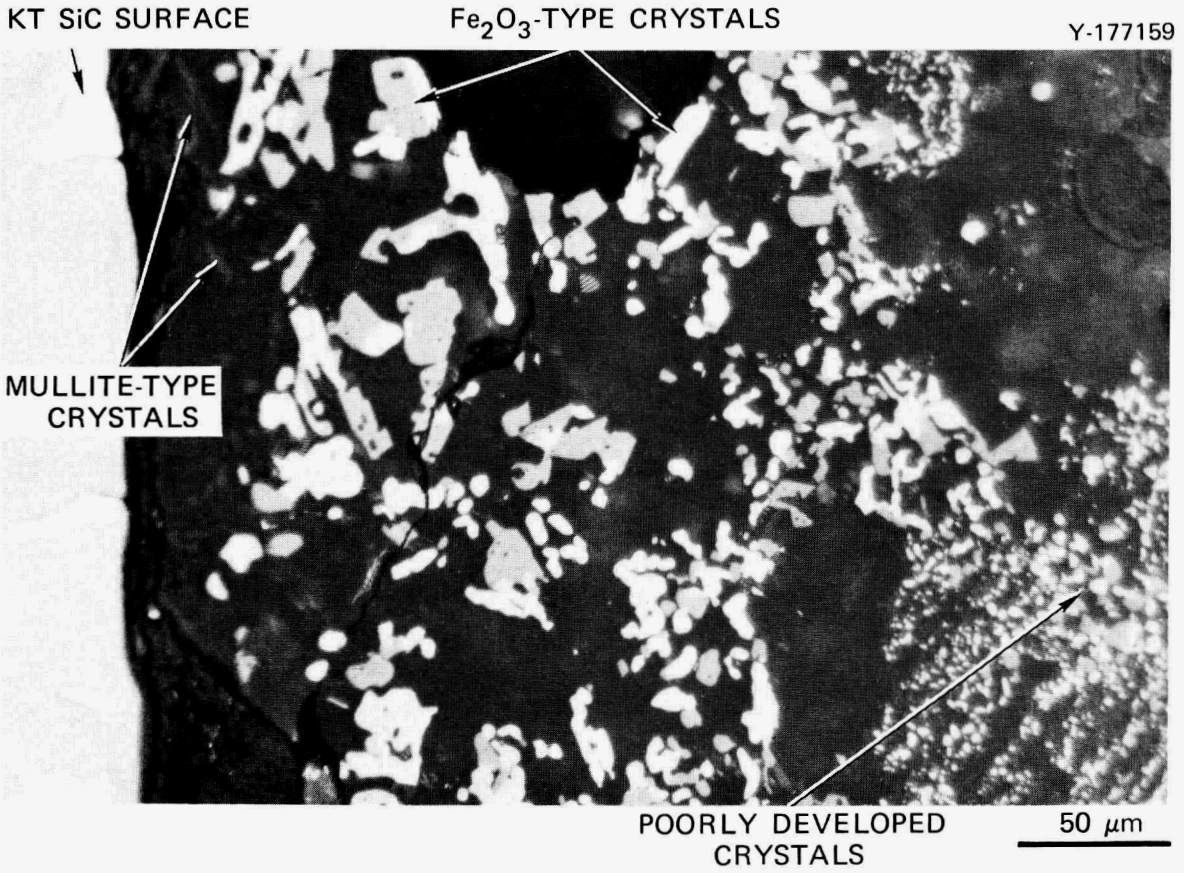

Fig. 59. Microstructural characteristics of downstream coal slag remaining on exposed KT SiC tube.

with increasing distance from this interface. Notice that the concentration of needlelike crystals (mullite) was also much smaller than in the upstream slag. The difference between the upstream and downstream slag characteristics was apparently related to variations in the flue gas aerodyamics along the upstream and downstream portions of the tubes. In the case of the downstream areas, turbulent flow of the flue gas may have limited the development of the slag crystals, possibly by modifying the slag temperature. Such flow may have also been responsible for the unusual distribution of the light-colored crystals observed in Fig. 59.

Helium Permeability

The results of the helium permeability analyses of the as-received (pretest) and exposed tubes are summarized in Table 12. Measurements were made while 101, 247, 446, and 618-kPa pressure differentials were maintained between the inside and outside of each ceramic tube. The detection limit of the helium spectrometer was 5×10^{-16} m^3/s. All tubes except KT SiC (tube 2) and α-SiC (tube 1) exhibited pretest permeabilities (leak rates) less than 8×10^{-15} m^3/s at all four pressure differentials. In addition, the pretest helium permeabilities of both the KT SiC (tube 1) and the CVD SiC (tube 2) increased by about an order of magnitude as the pressure difference increased from 101 to 618 kPa. The helium flow rate through the remaining as-received tubes showed no significant dependence upon the pressure differential. The postexposure permeabilities were not substantially different from the respective pretest values at 101 kPa. However, the helium leak rates for all surviving exposed materials increased by one to two orders of magnitude when the pressure differential was raised from 247 to 618 kPa. These increases were probably due to chemical, microstructural, or structural changes that occurred as a result of the exposure to the combustion products of the COM fuel. The cracks that formed near the radial delamination boundaries in the exposed CVD SiC may have provided fast paths for gas permeation on a microscopic scale. Also impurity elements in the exposed silicon carbides could have created localized chemical or microstructural changes that facilitated the gas

Table 12. Room-temperature helium permeability data on exposed and pretest ceramic tubes in CRAF Test 2

Material	Tested	He permeability, m^3/s, at prescribed pressure differential			
		101 kPa	247 kPa	446 kPa	618 kPa
KT SiC					
Tube 1	Pre	$<5.0 \times 10^{-16}$	$<5.0 \times 10^{-16}$	3.0×10^{-15}	3.0×10^{-15}
	Post	1.6×10^{-15}	1.6×10^{-15}	1.5×10^{-13}	3.5×10^{-13}
Tube 2	Pre	1.4×10^{-14}	1.4×10^{-14}	1.6×10^{-14}	1.6×10^{-14}
	Post	3.3×10^{-14}	2.1×10^{-13}	7.8×10^{-13}	1.5×10^{-12}
α-SiC					
Tube 1	Pre	2.4×10^{-14}	2.4×10^{-14}	2.4×10^{-14}	2.8×10^{-14}
	Post	3.7×10^{-15}	7.2×10^{-15}	1.5×10^{-14}	2.9×10^{-14}
Tube 2	Pre	$<5.0 \times 10^{-16}$	$<5.0 \times 10^{-16}$	$<5.0 \times 10^{-16}$	$<5.0 \times 10^{-16}$
	Post	9.3×10^{-16}	9.9×10^{-15}	3.1×10^{-14}	7.5×10^{-14}
CVD SiC					
Tube 1	Pre	1.8×10^{-15}	3.6×10^{-15}	3.6×10^{-15}	3.6×10^{-15}
	Post	5.7×10^{-16}	2.9×10^{-15}	1.4×10^{-14}	5.7×10^{-14}
Tube 2	Pre	$<5.0 \times 10^{-16}$	4.9×10^{-15}	4.9×10^{-15}	4.9×10^{-15}
	Post	$<5.0 \times 10^{-16}$	2.1×10^{-15}	1.2×10^{-14}	3.1×10^{-14}
Sialon					
Tube 1	Pre	$<5.0 \times 10^{-16}$	$<5.0 \times 10^{-16}$	$<5.0 \times 10^{-16}$	2.8×10^{-15}
	Post	*a*	*a*	*a*	*a*
Tube 2	Pre	*b*	*b*	*b*	*b*
	Post	*a*	*a*	*a*	*a*
Al_2O_3					
Tube 1	Pre	8.0×10^{-15}	8.0×10^{-15}	8.0×10^{-15}	8.0×10^{-15}
	Post	*a*	*a*	*a*	*a*
Tube 2	Pre	*b*	*b*	*b*	*b*
	Post	*a*	*a*	*a*	*a*

[a]Tube cracked too extensively for postexposure analysis.

[b]Tube exhibited helium transport above measurement ability of leak detector.

transport process. Unfortunately, little is known about the micromechanisms responsible for gas transport through ceramic materials or how such mechanisms are affected by the presence of various elements or secondary phases. Finally, the increases in the helium permeability would be of particular concern in high-temperature HX systems using high-pressure helium on the secondary side since significant helium leakage could adversely affect the economics in a system such as a closed-cycle gas turbine.

Values of the room-temperature gas permeability factor, K, were calculated from the information given in Table 12 with Eq. (3). The results are shown in Table 13. The parameter K, which is analogous to the thermal conductivity, characterizes the relationship between the gas pressure gradient across a material and the corresponding gas flow rate through the material. Since gas permeation is a thermally activated process, K depends exponentially on temperature. Therefore, the gas permeation rates may be several orders of magnitude larger than the room-temperature values at the temperatures of interest in actual HX systems. However, the expected increase in the helium permeation at high temperatures is based on the assumption that the transport mechanism does not change with temperature. If this assumption was correct in CRAF Test 2, then the helium permeability values in Table 12 would have to be modified accordingly to predict the helium leak rates that would be experienced in a ceramic HX system fired with acidic ash coal. The helium losses through ceramic-to-ceramic or ceramic-to-metal joints employed in constructing such an HX would also have to be determined.

Thermal Expansion

The linear thermal expansion of materials to be used in high-temperature HXs is very important because stresses can be generated in these structures by thermal cycling occurring during use as well as by temperature gradients that normally exist within an HX operating at temperature. In addition, a major concern in the use of structural ceramics in HXs is the ability of the structure to withstand stresses generated by thermal expansion during transient conditions.

Table 13. Permeability factors calculated from room-temperature helium permeability data in Table 12

Material	Tested	Permeability factor K, m^2, at prescribed pressure differential			
		101 kPa	247 kPa	446 kPa	618 kPa
KT SiC					
Tube 1	Pre	$<3.4 \times 10^{-26}$	$<1.4 \times 10^{-26}$	4.6×10^{-26}	3.3×10^{-26}
	Post	1.1×10^{-25}	4.2×10^{-26}	2.3×10^{-24}	3.9×10^{-24}
Tube 2	Pre	9.5×10^{-25}	3.9×10^{-25}	2.4×10^{-25}	1.8×10^{-25}
	Post	2.2×10^{-24}	5.8×10^{-24}	1.2×10^{-23}	1.7×10^{-23}
α-SiC					
Tube 1	Pre	7.1×10^{-25}	2.9×10^{-25}	1.6×10^{-25}	1.3×10^{-25}
	Post	1.1×10^{-25}	8.6×10^{-26}	10.0×10^{-26}	1.4×10^{-25}
Tube 2	Pre	$<1.5 \times 10^{-26}$	$<6.0 \times 10^{-27}$	$<3.3 \times 10^{-27}$	$<2.4 \times 10^{-27}$
	Post	2.7×10^{-26}	1.2×10^{-25}	2.1×10^{-25}	3.6×10^{-25}
CVD SiC					
Tube 1	Pre	3.8×10^{-26}	3.1×10^{-26}	1.7×10^{-26}	1.2×10^{-26}
	Post	1.2×10^{-26}	2.5×10^{-26}	6.7×10^{-26}	2.0×10^{-25}
Tube 2	Pre	$<1.0 \times 10^{-26}$	4.2×10^{-26}	2.3×10^{-26}	1.7×10^{-26}
	Post	$<1.0 \times 10^{-26}$	1.8×10^{-26}	5.7×10^{-26}	1.1×10^{-25}
Sialon					
Tube 1	Pre	$<1.8 \times 10^{-26}$	$<7.4 \times 10^{-26}$	4.1×10^{-27}	1.7×10^{-26}
	Post	*a*	*a*	*a*	*a*
Tube 2	Pre	*b*	*b*	*b*	*b*
	Post	*a*	*a*	*a*	*a*
Al_2O_3					
Tube 1	Pre	2.5×10^{-25}	1.0×10^{-25}	5.8×10^{-26}	4.1×10^{-26}
	Post	*a*	*a*	*a*	*a*
Tube 2	Pre	*b*	*b*	*b*	*b*
	Post	*a*	*a*	*a*	*a*

[a]Tube cracked too extensively for postexposure analysis.

[b]Tube exhibited helium transport above measurement capability of leak detector.

The thermal expansion of the five types of ceramics exposed to COM combustion was measured by cutting longitudinally oriented specimens from as-received tubes and from the upstream and downstream sides of exposed tubes. Only an upstream exposed specimen of the sialon tube was measured because the extensive cracking precluded preparation of a specimen from the downstream side. The thermal expansion was measured from room temperature to about 1100°C. Curves showing the thermal expansion in terms of $\Delta L/L$, the incremental change in length divided by the initial length versus temperature will be given and discussed in the following. In general, long-term exposure of the five types of ceramics to the combustion products of the coal and residual oil in the COM fuel resulted in an increase in the thermal expansion at a given temperature, and in some cases this increase was substantial. The accuracy of the thermal expansion measurements that were made with a push-rod dilatometer was ±5%, so we regard measured changes within this range as insignificant. The three types of SiC ceramics will be discussed followed by the AD 998 Al_2O_3 and the sialon.

KT SiC

The thermal expansion behavior of KT SiC will be discussed first, since this type of siliconized SiC has been considered for use in ceramic HXs by several investigators. In Fig. 60 the thermal expansion curves of specimens cut from as-received and exposed KT SiC tubes are shown. Two specimens were cut from an exposed tube as shown in Fig. 13 with their long dimensions parallel with the tube axis. One specimen was from the upstream tube side (the side that faced the combustor), while the other was from the downstream tube side, located 180° away from the upstream side.

From Fig. 60, it is apparent that the thermal expansion of KT SiC increased because of the long-term combustion gas exposure. Analysis of the expansion curves will be discussed for temperatures of 1000 and 1100°C to provide a perspective of the magnitude of the changes. At 1000°C, $\Delta L/L$ values from Fig. 60 indicate that the expansion on the downstream side of the tube increased by 9.5% compared with that of the as-received KT SiC. Furthermore, the expansion of the upstream side was 16.8% more than that of as-received material. The expansion of the upstream

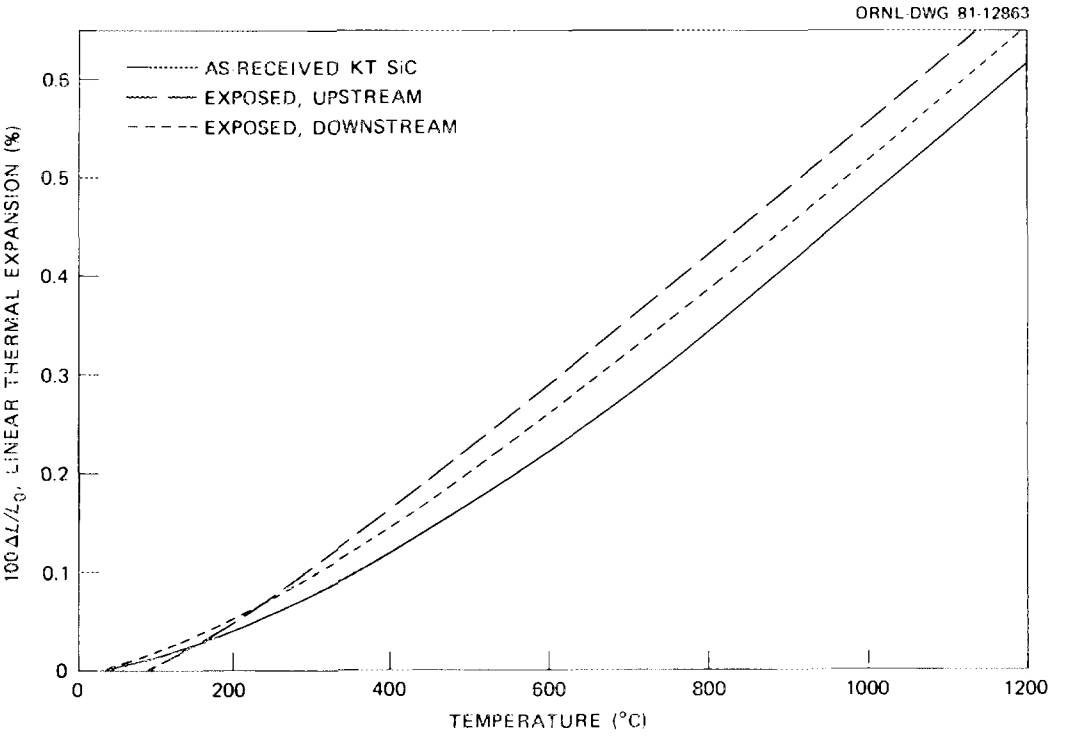

Fig. 60. Thermal expansion of as-received and exposed KT SiC.

specimen was 6.7% greater than that of the downstream specimen. At 1100°C the expansion increase of upstream and downstream specimens was slightly less than that at 1000°C. The downstream specimen had an expansion increase of 7.3%, whereas the upstream specimen increase was 13.8%. The percentage difference between upstream and downstream specimens was 6.0%.

These results indicate, as noted previously, that the thermal expansion of KT SiC increased because of the exposure and that the increase was nonuniform within the tube from the upstream to the downstream side. According to the estimated accuracy of the expansion measurements, the indicated changes are significant. Uniform changes in the thermal expansion of ceramic HX tubes could be accommodated in the design, since thermal dilation must obviously be accounted for anyway. Nonuniform expansion changes in HX tubes could result in substantial bowing stresses in long tubes unless the nonuniform dilation could be accommodated at one of the tube-to-header joints without affecting the leaktightness of the joint.

The origin of the observed expansion increases has not been determined. The increases are apparently not caused by development of

additional major phases within the microstructure of the KT SiC because none were observed in either the optical microscopy or x-ray diffraction analyses. As noted in the chemical analysis discussion, substantial changes in the concentration of certain elements in the material resulted from the exposure. The elements were apparently incorporated into the structure by substitution into either the silicon or the SiC phase, or both, since no significant concentrations of new secondary phases were detected. This process may explain the observed increases. Better understanding of this phenomenon is required, and further studies will be directed to its understanding and ways sought to mitigate the expansion changes.

Sintered α-SiC

The thermal expansion of a specimen cut from an as-received sintered α-SiC tube as well as specimens from the upstream and downstream side of an exposed tube were measured in air with the same dilatometer employed for KT SiC. The expansion curves are shown in Fig. 61. In this ceramic material, exposure to the coal slag resulted in modest increase in thermal expansion at 1000°C of +5.3% in the upstream side specimen. This increase is very close to the accuracy of the measurement possible with the dialotometer employed. At 1100°C, this increase was +5.6%, which is again a value close to the accuracy of the measurement. As shown in Fig. 61, the downstream sample exhibited a thermal expansion essentially identical with that of the as-received material. For α-SiC exposed to the combustion products of the COM, thermal expansion changes were less than those in KT SiC. The expansion behavior of these two structural ceramics was quite different when exposed to the combustion products of No. 6 oil alone and the COM containing acidic-ash coal in No. 6 oil. In the former case (CRAF Test 1), all three siliconized types of SiC (KT, NC 430, and Refel) had essentially no change in their thermal expansions due to the long-term high-temperature exposure, while the sintered α-SiC showed a substantial increase for upstream side specimens. In this experiment the behavior was inverted, with the siliconized KT SiC having a substantial expansion increase, while α-SiC was relatively unaffected. As noted in the discussion for KT SiC, the microstructural and compositional causes for

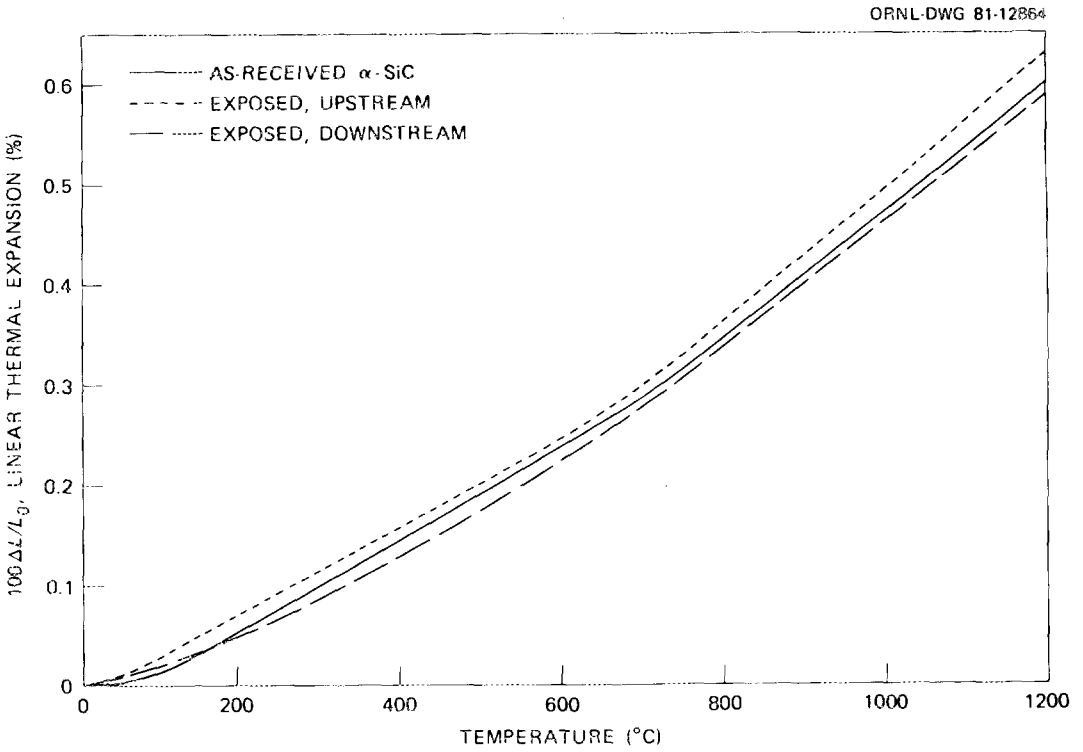

Fig. 61. Thermal expansion of as-received and exposed α-SiC.

these changes have not as yet been determined. However, the results of CRAF Test 1 and this experiment suggest that the nature of the fuel ash in the hot gases, its composition, and perhaps the high-temperature deposition mechanisms(s) have a strong bearing on the diffusion of certain impurity elements into the constituent phases in these ceramics to produce the observed thermal expansion changes.

Chemically Vapor-Deposited SiC

The thermal expansion was measured for specimens cut from as-received CVD SiC and upstream and downstream specimens from an exposed tube. The dependence of the thermal expansion on temperature of these specimens is shown in Fig. 62. For this ceramic material, both upstream and downstream specimens had substantial expansion increases at all temperatures. At both 1000 and 1100°C, the expansion of the upstream specimen was about 17% greater than the as-received specimen, while the downstream specimen had an expansion increase of about 13%. The expansion difference of 4%

between the upstream and downstream specimens was within the accuracy of the measurement, but the data suggest that a small expansion differential existed between the two at all temperatures up to at least 1200°C, with the upstream specimen having the larger expansion.

The expansion behavior of CVD SiC after long-term exposure to coal combustion products was substantially different from that reported earlier from exposure to No. 6 oil combustion.[1] In this latter case, CVD SiC had no change in expansion due to the exposure, but in the present case there was a substantial increase in the expansion. Microstructural and x-ray diffraction analyses did not provide obvious evidence for explaining these differences in behavior for this ceramic material in the two different combustion environments. According to the results, the CVD SiC employed in this exposure experiment had a substantial increase in thermal expansion, the increase was relatively uniform from the upstream to downstream sides of the tube.

An explanation for the observed expansion increase in CVD SiC tubes during the exposure is not available, nor is it obvious why this material,

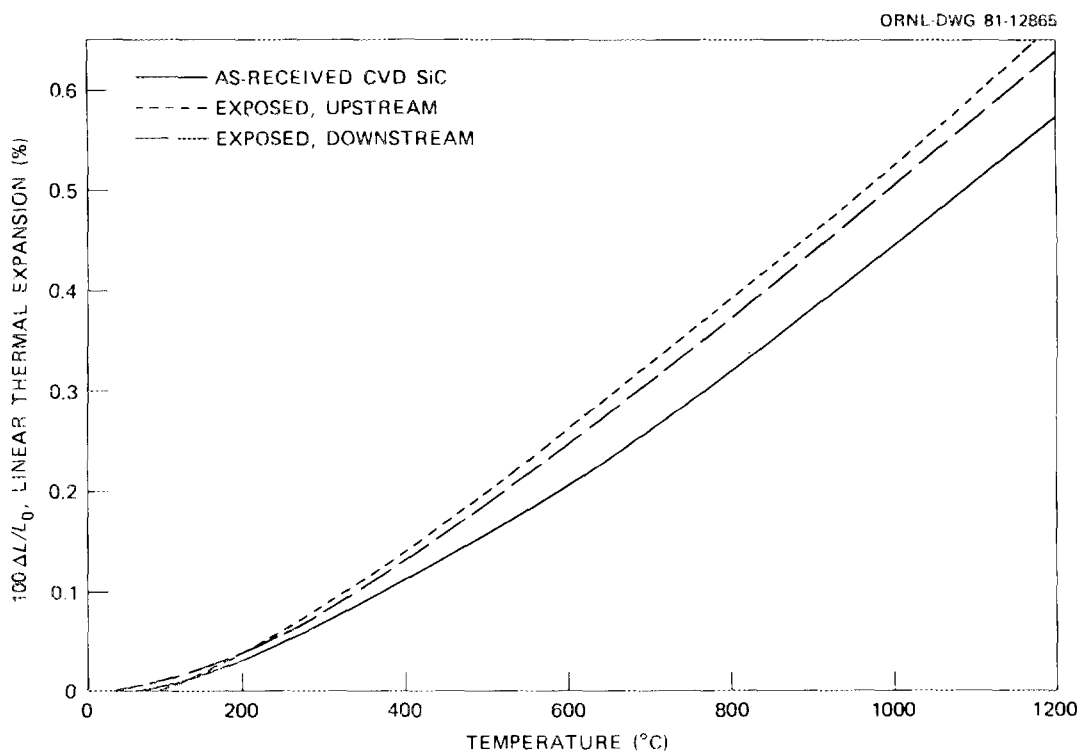

Fig. 62. Thermal expansion of as-received and exposed CVD SiC.

which originally contained a significant concentration of β-SiC, exhibited a relatively large expansion increase, whereas sintered α-SiC showed insignificant changes. The percentage expansion increase in CVD SiC for the upstream specimen was essentially identical with that for the upstream KT SiC specimen.

AD 998 Al_2O_3

The thermal expansion behavior of specimens removed from tubes of AD 998 containing primarily Al_2O_3 was similar to that of KT SiC and α-SiC in that the expansion of the upstream side specimen increased substantially from the as-received value. Thermal expansion data for the AD 998 specimens are shown in Fig. 63. The downstream side specimen expansion was not significantly different from that of the as-received specimen. At 1000°C, the expansion of the upstream exposed specimen was 13.8% greater than that for the as-received specimen, and at 1100°C this percentage was 14.3%. Since the downstream side specimen had essentially the same expansion as the as-received material, these data suggest that high-purity Al_2O_3 HX tubes exposed under the stated conditions would acquire significant stresses as a result of the substantial expansion differential between opposite sides of the tubes. The difference in thermal expansion between the upstream and downstream sides of the tubes at 1000 or 1100°C was about 16.5%. Again, the only experimental evidence obtained to date to explain the observed expansion increase on the upstream side of the tube is based upon the elemental chemical changes associated with the exposure and discussed elsewhere in this report. The microstructural and x-ray diffraction data did not provide an obvious explanation for the observed thermal expansion increase. Further study of this phenomenon is in progress.

GE 128 Sialon

The thermal expansion of specimens removed from tubes of GE 128 sialon was measured for as-received, exposed upstream, and laboratory oxidized conditions. The thermal expansion curves for these conditions are

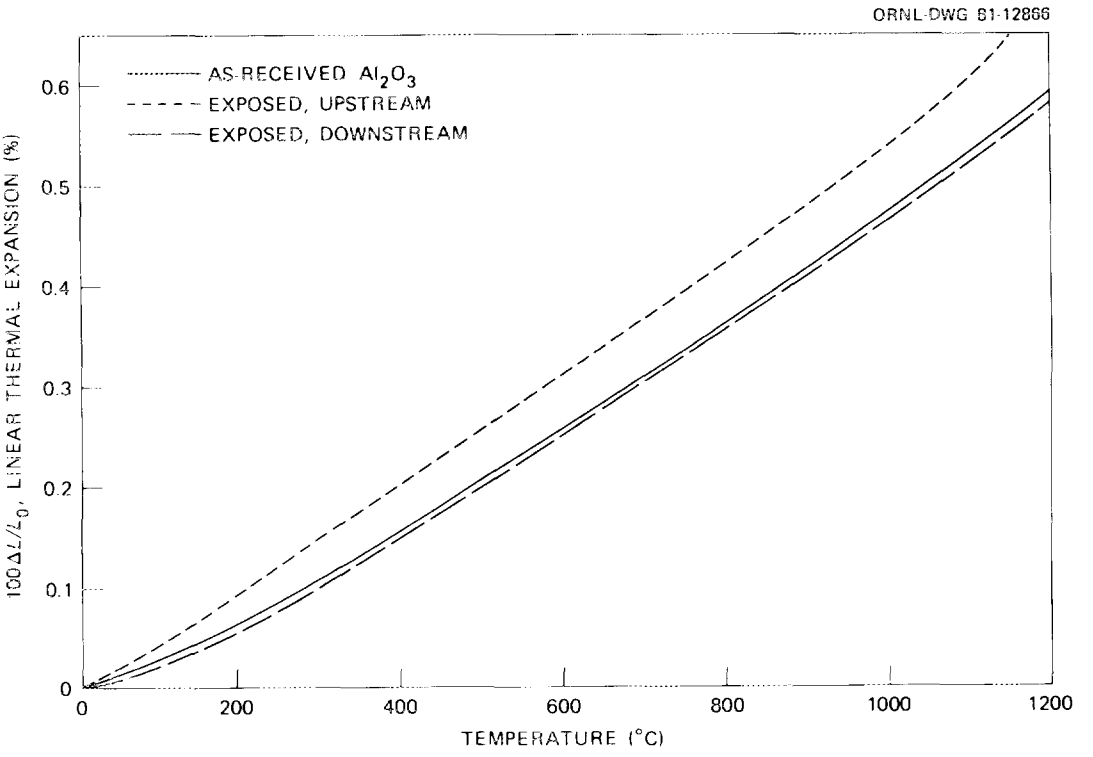

Fig. 63. Thermal expansion of as-received and exposed Al_2O_3.

shown in Fig. 64. A downstream specimen was not obtained from the exposed tubes because of extensive cracking. The expansion curve for as-received material is an average for heating and cooling. This ceramic contained a very complex phase mixture, which apparently was not close to thermodynamic equilibrium as received. This was evidenced by the nonreproducible thermal expansion on heating and cooling exhibited by as-received material. Data from which the average as-received specimen expansion curve in Fig. 64 was derived are shown in Fig. 65 for heating and cooling conditions. Specimens oxidized for long periods of time at high temperature or exposed to fuel combustion for long periods did not exhibit the extensive hysteresis shown in Fig. 65. From Fig. 64, the expansion of the exposed upstream specimen is greater than the expansion of the laboratory oxidized specimen, but because of the complex expansion behavior shown in Fig. 65 for this material, more definitive conclusions on the effect of combustion product exposure on this material are not warranted.

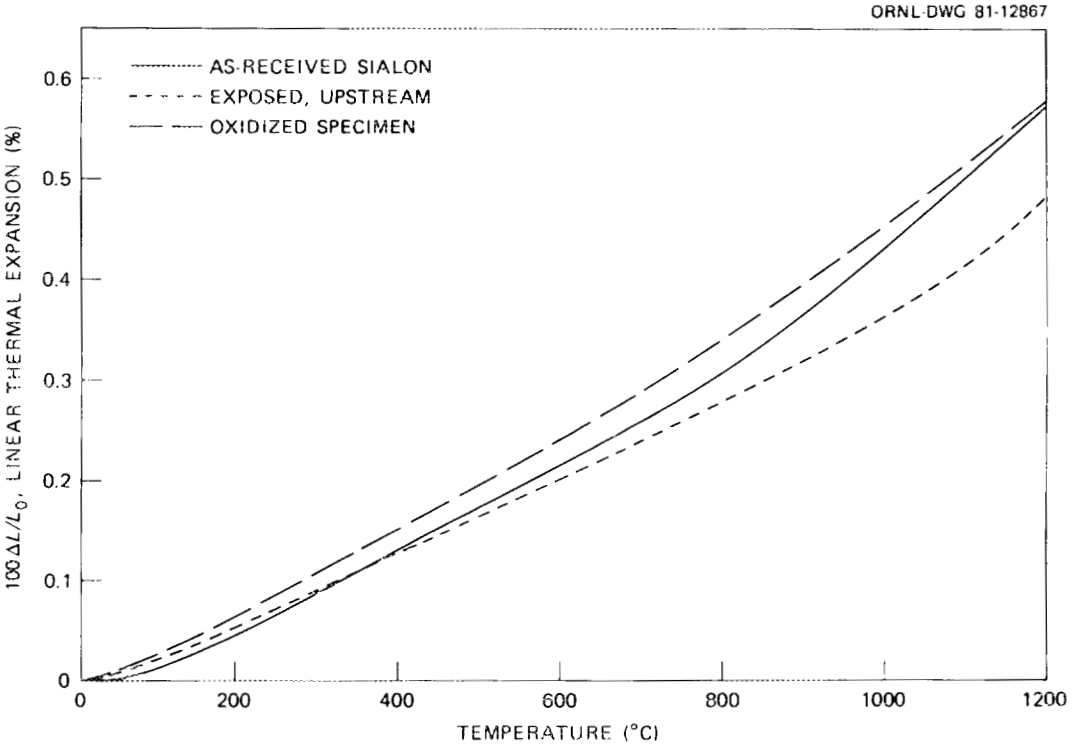

Fig. 64. Thermal expansion of pretest, exposed, and oxidized sialon samples.

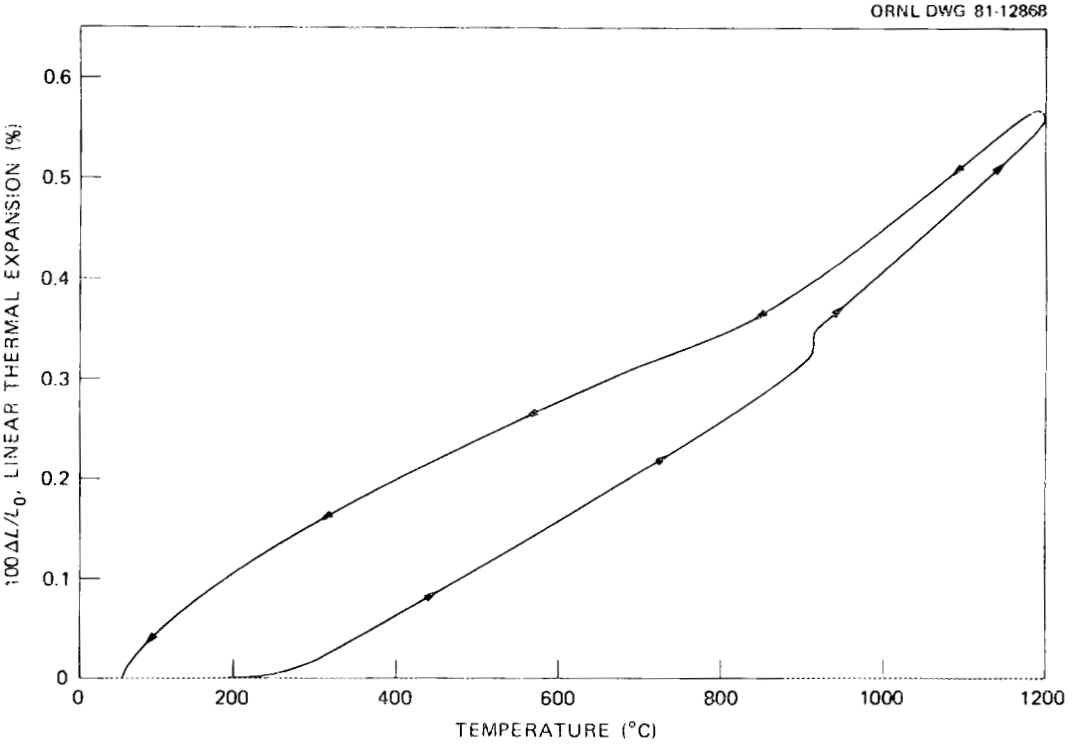

Fig. 65. Thermal expansion and contraction curves for as-received sialon.

Tensile Strength

The C-ring tensile fracture strength was determined for the as-received and surviving exposed tubular materials. With the exception of the sialon, 11 to 14 C-ring samples were prepared from each tube and then tested. However, only four or five C-ring specimens could be fabricated from the sialon and fractured since the corresponding tubes were shorter than the other tubular elements. The average tensile strengths and their standard deviations calculated from these measurements are given in Table 14. The modulus of rupture values reported by the vendor for the materials are also included. A comparison of these modulus of rupture values and the respective as-received fracture strengths reveals some fairly significant variations. These discrepancies, which are particularly large for the sialon, can be attributed to several factors.

Table 14. Results of C-ring strength tests for as-received and exposed tubular materials

Material	Strength value,[a] MPa (ksi)			
	Reported by vendor	As received	Exposed	Change (%)[b]
KT SiC	142 (20.6)	178.6 ± 8.2 (25.9 ± 1.2)	198.6 ± 15.4 (28.8 ± 2.2)	+11.2
CVD SiC	314 (45.5)	346.7 ± 54.0 (50.3 ± 7.8)	334.9 ± 40.5 (48.6 ± 5.9)	−3.4
α-SiC	—	304.6 ± 52.3 (44.2 ± 7.6)	292.0 ± 24.4 (42.4 ± 3.5)	−4.1
Al_2O_3	186 (27.0)	146.8 ± 18.8 (21.3 ± 2.7)	[c]	
Sialon	300 (43.5)	93.4 ± 10.3 (13.6 ± 1.5)	117.2 ± 10.1[c,d] (17.0 ± 1.5)	+25.5

[a]Numbers following ± sign represent standard deviation.

[b]Percent change equals (exposed value minus as-received value)/as-received value.

[c]Tube was cracked too extensively to be measured.

[d]Strength values were obtained from C-ring samples oxidized in air at 1250°C for 100 h.

First, the manufacturer's tests involved the use of generic materials, which were probably considerably different from those used in this study. In fact, one might expect that the strength-controlling surface flaws in flexure bars typically used for such determinations would be different from those in tubular materials because of variations in the respective processing and fabrication techniques. This was particularly true for the sialon. For example, a comparison of the surface characteristics of the sialon tube with those of bend bars used in a related study[18] suggested that the surface flaws were much more severe along tubular surfaces because of the plate-type morphology. This would account for the low value of the as-received C-ring strength compared with the vendor's value. Finally, the variations between the modulus of rupture and as-received C-ring strength may have partially reflected inherent differences in the respective test geometries (i.e., bending versus C-ring compression loading). We are not aware of any pertinent studies that compare the C-ring tensile strength of a particular material with that predicted from flexure measurements.

The experimental data in Table 14 indicate that the C-ring strengths of the SiC tubes were only slightly affected by the exposure to the coal slag. The largest change occurred in the KT SiC, which exhibited an 11.2% increase after the 496-h test. This strength increase, which was also observed in other studies involving siliconized SiC,[1,8] was probably due to blunting of the surface flaws by the viscous oxide layer that formed on the tubular surface during CRAF Test 2. The blunting process was also likely facilitated by deformation of the silicon phase present in the KT SiC. This explanation is consistent with the fact that no strength increases were observed for the CVD SiC or α-SiC, both of which contained no free silicon. In fact, the strength of these two materials appeared to decrease slightly after their exposure to the COM combustion products. However, since the magnitude of these changes was small when compared with the respective standard deviations, the statistical significance of the strength reductions is questionable The postexposure strengths of the sialon and aluminum oxide materials could not be ascertained since these tubes cracked extensively during the CRAF exposure. Nevertheless, insights

into the possible strength changes occurring in the sialon were obtained by comparing the as-received strength with the value determined from C-ring samples exposed to air at 1250°C for 100 h. This treatment resulted in the formation on the outer C-ring surface of an oxide coating that was similar to that observed on the exposed tubes. From Table 14 it is apparent that the oxidized strength was significantly larger than the pretest value. Once again, a crack blunting mechanism related to the oxidation process was probably responsible for the strength increase. Specifically, the oxide layer may have reduced the severity of the plate-like features of the original tube surface. Finally, it should be pointed out that the magnitudes of strength changes observed in CRAF Test 2 were much smaller than those obtained in CRAF Test 1, which involved the combustion of only a No. 6 oil.[1] This suggests that the small nodules that formed on the upstream side of the silicon carbide tubes in Test 1 had a considerably greater influence on the flaw population than did the refractory coal slag present in this study.

The general trends discussed above were based solely on the room-temperature C-ring strength values. However, the high-temperature strength may ultimately limit the use of a potential ceramic HX material. For example, at temperatures above 1300°C, deformation of the silicon phase in siliconized SiC may degrade the overall tubular element. At lower temperatures, fuel impurities such as iron and nickel may combine with the silicon to form low-melting eutectics, which also facilitate this deformation process. In addition, slow crack growth in ceramic materials at high temperature will result in a long-term strength degradation, which may not be apparent in the room-temperature values of the pretest and post-test C-ring strength. Consequently high-temperature strength measurements of as-received and exposed materials would be quite useful.

The fact that the alumina and sialon cracked extensively during the 496-h exposure indicates that fairly large stresses were generated in the tubes. The CRAF Test 2 exposure conditions included at least two important sources of stress. The first was thermal stresses that resulted from the temperature gradients established across the tube walls. For example, if the heat transfer through the tubes is characterized by a uniform radial flow that is independent of the longitudinal position along the

tubes, one can estimate the temperature distribution for steady-state conditions as

$$T(r) = T_i + (q/2\pi kL)\ln(r/r_i) \ , \tag{5}$$

where q is the steady state heat flow,* k is the thermal conductivity of the particular tubular material, L is the tube length, r_i is the inner radius of the tube, and T_i is the temperature at $r = r_i$. The derivation of this equation is also based on the assumption that the temperatures of the inner and outer surfaces did not vary with position. Furthermore, the temperature variations arising from the presence of the coal slag, which was preferentially deposited upon the upstream side of all tubes, are not considered in this treatment.

The primary advantage of the temperature distribution given above is that it can be readily used in conjunction with the equations of linear elasticity[19,20] to calculate the magnitude of the stresses resulting from the differential thermal strains established by the temperature gradient. In terms of polar coordinates the tangential, radial, and longitudinal stresses (σ_θ, σ_r, and σ_z, respectively) are

$$\sigma_\theta = A - B/r^2 - E\alpha[T(r) + C]/2(1 - \nu) \ , \tag{6}$$

$$\sigma_r = A + B/r^2 - E\alpha T(r)/2(1 - \nu) \ , \tag{7}$$

and

$$\sigma_z = M - E\alpha T(r)/(1 - \nu) \ , \tag{8}$$

where E is Young's modulus, ν is Poisson's ratio, α is the thermal expansion coefficient, C is equal to $q/2\pi kL$, and A, B, and M are integration constants, which must be chosen to satisfy the boundary conditions. From

*The value of q can be determined from the data in Table 2.

this analysis, one predicts that the maximum tensile stresses should occur at the inner surface of the tube, where $\sigma_\theta = \sigma_z > 0$ and $\sigma_r = 0$. In addition, the magnitude of the σ_θ values predicted for the various tubular materials (Table 15) is fairly small when compared with the respective pretest strengths. Therefore, it is unlikely that these particular thermal stresses were responsible for the cracking observed in the sialon and alumina tubes. However, it should be mentioned that these predicted stress values neglect the contribution from bending that would arise from unsymmetrical heat flow through the tubes.[9] Since this contribution would become particularly important in long tubular materials used in a cross-flow HX array, it must be considered.

Thermal stresses could have also been generated as a result of the thermal expansion mismatch between the thick deposits of coal slag and the tubular materials. Since the slag matrix was composed primarily of an aluminosilicate glass, its average thermal expansion coefficient was probably about $4 \times 10^{-6}/°C$, which is smaller than the coefficients associated

Table 15. Estimation of thermal stresses resulting from steady state heat flow through ceramic tubes in CRAF Test 1

Material	Tangential stress, σ_θ, at inner radius[a]		Ratio of σ_θ to measured pretest strength
	(MPa)	(ksi)	
α-SiC	17.2	2.50	0.06
CVD SiC	17.2	2.50	0.05
KT SiC	58.6	8.51	0.33
Al_2O_3	67.8	9.83	0.46
Sialon	17.1	2.48	0.18

[a] At $r = r_i$, $\sigma_\theta = \sigma_z$ and $\sigma_r = 0$.

with all five ceramic materials (Table 6). Although the property data in Table 6 indicate that the thermal expansion coefficient of sialon is smaller than $4 \times 10^{-6}/°C$, the experimental thermal expansion data for the tubular material revealed a significantly higher value ($\sim 4.7 \times 10^{-6}/°C$). Consequently, during the cooldown following the long-term exposure, the contraction of the ceramic tubes was constrained by the coal slag layer. In the case of the SiC tubes, this constraint was extremely limited because of the lack of adequate bonding between the ceramic and slag. However, the strong adherence of the slag to both the alumina and sialon tubes may have facilitated this constraining action, which ultimately led to the formation of considerable mechanical stresses on cooldown to ambient temperature.

One can estimate these stresses by approximating the slag-ceramic geometry as two concentric cylinders differing in thermal expansion coefficients. Furthermore, at some elevated temperature T_h, the constraint and thus the induced stresses are assumed to be zero. In CRAF Test 2, T_h corresponds to the temperature at which the slag viscosity was sufficient to elastically restrain the contraction of the alumina or sialon tubes. Upon cooldown to room temperature, T_r, the differential contraction between the concentric cylinders, produces a pressure P_i at the interface,[20] which is given as

$$P_i = \frac{(T_h - T_r)(\alpha_c - \alpha_s)}{\frac{1}{E_c}\left(\frac{1 + k_1^2}{1 - k_1^2} - \nu_c\right) + \frac{1}{E_s}\left(\frac{k_2^2 + 1}{k_2^2 - 1} + \nu_s\right)} , \tag{9}$$

where k_1 is the ratio of the inner to outer radius of the inner cylinder (i.e., ceramic tube), k_2 is the ratio of the outer to inner radius of the outer cylinder (i.e., the coal slag), E is Young's modulus, ν is Poisson's ratio, and α is the thermal expansion coefficient. The subscripts c and s refer to the ceramic and slag, respectively. The radial and tangential stresses that are developed in the ceramic as a result of this pressure are

$$\sigma_r = P_i(1 - a_i^2/r^2)/(1 - k_1^2) \text{ (radial)} \tag{10}$$

and

$$\sigma_\theta = P_i(1 + a_i^2/r^2)/(1 - k_1^2) \text{ (tangential)} , \tag{11}$$

where a_i is the inner radius of the ceramic tube. If the appropriate numbers are substituted into Eqs. (9), (10), and (11),* one finds that the tangential stresses are quite high, particularly at the inner radius ($r = a_i$). For example, the σ_θ value predicted for the alumina tube is 140 MPa (20.3 ksi), which is comparable to the pretest C-ring strength value (Table 14). Therefore, the strong bonding between the alumina and coal slag plus the substantial ceramic-slag thermal expansion mismatch were likely responsible for the extensive cracking in the Al_2O_3 material. Conversely, the σ_θ predicted for sialon of 21 MPa (3.0 ksi) is significantly smaller than the respective as-received strength value. This suggests that other factors were responsible for the severe fracturing observed in the sialon. Finally, the predicted σ_θ values are based on the assumption of a uniform slag thickness because this is required for the concentric cylinder geometry analysis. Although this uniformity was lacking in the actual tubular geometry, the σ_θ values given above still provide a relative estimate of the tensile stresses.

The previous stress analyses were based on fairly simplified stress distributions, which were chosen because of their mathematical simplicity. However, in actual HX applications, the stress state will probably be a complicated mixture of tension, compression, and bending. The exact nature of the stress state will also depend on how the individual tubular elements

---

*The assumed slag characteristics are as follows: T_h = 500°C, E_s = 75.8 GPa, ν = 0.25, and $\alpha_s = 4.0 \times 10^{-6}$/°C. The slag thickness is taken to be 6.35 mm.

are joined together and how they are fastened into the header blocks. Consequently, a more sophisticated analysis will eventually be necessary to ensure that the maximum service stress does not exceed the strength of the tubular material. Nevertheless, the present C-ring strength measurements and associated stress analyses still yield useful information, which can be used to make an initial evaluation of potential ceramic HX materials.

SUMMARY AND CONCLUSIONS

The 496-h exposure to the combustion products of the acidic-ash coal resulted in the formation of thick deposits of coal slag on all tubes. The fact that the chemical composition of the coal slag was quite similar to that of the initial coal ash gave evidence that the COM fuel could be successfully used to study the effects of coal combustion upon the structural and chemical properties of the five ceramic materials. However, the alteration of these properties resulting from the combustion of the oil itself was apparently minimized.

The strong interfacial bonds formed between the coal slag and both the sialon and Al_2O_3 tube were apparently responsible for the extensive cracking observed in these two materials. This fracture problem raises serious questions concerning the use of the sialon and Al_2O_3 materials in HX applications involving highly fouling environments containing acidic coal ash constituents. Conversely, all the silicon carbide tubes including KT SiC, α-SiC, and CVD SiC survived the exposure without any major material degradation. From this observation and the results of CRAF Test 1, it is apparent that the KT, α-, and CVD silicon carbides are excellent HX candidates when either No. 6 oil or acidic coal ash fuel impurities are present in the HX environment.

With the exception of the KT SiC, metallographic and SEM analyses revealed no significant changes in the microstructures of the silicon carbide materials following the 496-h exposure. A few isolated corrosion pits formed along the upstream surface of the KT SiC. However, the total amount of surface corrosion was still quite limited. The microstructural analyses of the sialon and Al_2O_3 tubes revealed a 150-μm-thick oxidation layer at the sialon-slag interface and a 6- to 12-μm-thick aluminosilicate

layer at the alumina-slag interface. The oxide product at the sialon surface was apparently composed of silicon oxide and a magnesium aluminosilicate. The strong interfacial bonding coupled with the thermal expansion mismatch between the slag and both ceramic materials may have led to the formation of large tensile stresses in the respective tubular elements upon cooldown from the 1230°C test temperature. These stresses would have been sufficient to cause fracture in the alumina tubes.

Besides the above-mentioned microstructural changes, the 496-h exposure was also responsible for a complex redistribution in the concentration of many of the minor elemental impurities. The reasons for these changes and their effect on the strength, thermal expansion, and helium permeability of the tubular materials were not clearly evident. However, there was evidence that the formation of the thick coal slag deposits during the test limited the transport of elements such as iron, nickel, and sodium. This was further confirmed by the fairly large concentrations of these fuel impurities in the tubular materials exposed in CRAF Test 1, which were covered only with small isolated nodules.

The helium permeabilities of the surviving exposed silicon carbide tubes were not significantly different from the respective values measured for the as-received materials at each pressure differential. In addition, the helium leak rates for both the pretest and exposed tubes increased by at most one order of magnitude as the helium pressure differential was raised to 618 kPa. The only exception to this was the exposed α-SiC (tube 2), which exhibited an increase in helium permeability two orders of magnitude.

The results of the thermal expansion measurements after the long-term exposure revealed some very significant changes in many of the tubes. Except for the sialon, the thermal expansion of the exposed upstream sample at temperatures around 1100°C was significantly larger than that of the as-received material. The thermal expansion of the exposed downstream specimen generally fell between these two extremes. The differential expansion characteristics of the exposed tubes are of particular concern since they would be expected to cause the formation of considerable stresses in long tubular elements. The as-received sialon ceramic exhibited a large expansion-contraction hysteresis, which was related to

the formation of an oxide layer on the outer surface. This hysteresis effect may have been partly responsible for the cracking in this material. Currently, differential thermal expansion measurements, which are considerably more sensitive to microstructural variations, are being made in an attempt to better understand the unusual thermal expansion characteristics we observed.

A fairly large increase in the room-temperature C-ring strength of the KT SiC occurred during the test exposure. This increase was apparently related to high-temperature flaw blunting processes, which decreased the severity of the surface flaws. These processes were probably facilitated by deformation of the silicon phase, which is consistent with the absence of significant strength increases for either the CVD or α-SiC ceramics. Both these materials contain little or no free silicon. The strength changes in Al_2O_3 or sialon could not be ascertained because of the extensive cracking of the exposed materials. However, the as-received strength values for both ceramics were fairly low.

ACKNOWLEDGMENTS

The authors express appreciation to James Hickerson of the Pittsburgh Energy Technology Center for his support in sponsoring this program at ORNL. We also acknowledge G. C. Wei of the Metals and Ceramics Division at ORNL for his contributions associated with the initial set-up of the CRAF and the ceramic specimens, which are the basis of this report. Other Metals and Ceramics Division personnel whose contributions were particularly significant in making the work successful include: J. F. Willmering, D. B. Fielden, and B. R. Chilcoat for operating the CRAF; S. B. Waters, L. L. Hall, and D. B. Fielden for specimen preparation; W. H. Warwick for ceramography; and O. B. Cavin for x-ray diffraction. In addition, the assistance of H. W. Dunn and F. L. Ball in the Analytical Chemistry Division for scanning electron microscopy and electron microprobe analyses is also appreciated. Special thanks are expressed to R. K. Williams and A. J. Caputo for reviewing the manuscript; Faye Burns for typing the draft; Felicia Foust for assembling the draft and proofreading; Sigfred Peterson for editing the report; J. P. Hickey for the graphics; Alice Rice, Shirley Frykman, and Patsy Thornton for typing the appendix and distribution; and Denise Campbell and Aurelia Carter for preparing the final version for printing.

REFERENCES

1. G. C. Wei and V. J. Tennery, *Evaluation of Tubular Ceramic Heat Exchanger Materials in Residual Oil Combustion Environment*, ORNL/TM-7578, March 1981.
2. V. J. Tennery and G. C. Wei, *Recuperator Materials Technology Assessment*, ORNL/TM-6227, February 1978.
3. W. Kays and A. L. London, *Compact Heat Exchangers*, McGraw-Hill, New York, 1964.
4. R. Perkins, *Reaction of Silicon Carbide With Fused Coal Ash*, Report EPRI AF-294, Electric Power Research Institute, Palo Alto, Calif., November 1976.
5. G. W. Weber and V. J. Tennery, *Materials Analyses of Ceramics for Glass Furnace Recuperators*, ORNL/TM-6970, November 1979.
6. A. Gatti and M. J. Noone, *Methods of Fabricating Ceramic Materials*, AFML-TR-77-135, General Electric Co., Philadelphia, November 1977.
7. G. K. Layden, *Development of SiAlON Materials*, CR-135290, United Technologies Research Center, East Hartford, Conn., December 1977.
8. M. Combs et al., *High-Temperature Ceramic Heat Exchanger Development, Final Technical Report*, Report 79-15721, AiResearch Manufacturing Co. of California, Torrance, Calif., Jan. 31, 1979.
9. M. E. Ward and J. C. Napier, *Development of Ceramic Tube Heat Exchanger With Relaxing Joint*, FE-2556-17, Solar Turbines International, San Diego, Calif., June 15, 1978.
10. J. N. Cernica, *Strength of Materials*, Holt, Reinehart, and Winston, New York, 1966, pp. 205–6.
11. E. P. Popov, *Mechanics of Materials*, Prentice-Hall, Englewood Cliffs, N. J., 1978, pp. 150–55.
12. K. H. Jack, "X-Ray Data for Sialons and Other Nitrogen Ceramic Phases," unpublished data, Department of Metallurgy and Engineering Materials Crystallographic Laboratory, University of Newcastle Upon Tyne, England.

13. Joint Committee on Powdered Diffraction Standards, *Powder Diffraction File*, Swarthmore, Pa., 1979.

14. W. Davidge and T. J. Green, "The Strength of Two-Phase Ceramic Glass Materials," *J. Mater. Sci.* 3: 629–34 (1968).

15. A. G. Evans, "Microfracture From Thermal Expansion Anisotropy — I. Single Phase Systems," *Acta Metall.* 26: 1845–53 (1978).

16. N. Claussen, J. Staab, and R. Pabst, "Effect of Induced Microcracking on Fracture Toughness of Ceramics," *Am. Ceram. Soc. Bull.* 56: 559–62 (1977).

17. D. R. Clarke, "Microfracture in Brittle Solids Resulting From Aniostropic Shape Changes," *Acta Metall.* 28: 913–24 (1979).

18. P. F. Becher, unpublished work, ORNL.

19. S. P. Timoshenko and J. N. Goodiner, *Theory of Elasticity*, McGraw-Hill, New York, 1970, pp. 443–59.

20. H. Ford and J. M. Alexander, *Advanced Mechanics of Materials*, Wiley, New York, 1977, pp. 273–88.

APPENDIX

Indexing Results of Diffraction Patterns Obtained for As-Received and Exposed Ceramic Materials and Coal Slag

Table A1. X-ray diffraction results for KT SiC

	As-received material		Exposed material — upstream area				Known d, nm, and (intensities)				
			Surface region		Subsurface region						
	d (nm)	Relative intensity	d (nm)	Relative intensity	d (nm)	Relative intensity	α-SiC 33R JCPDS 22-1316	α-SiC 12H JCPDS 29-1128	α-SiC 51R JCPDS 4-0756	Si JCPDS 5-0565	C 4H Graphite 4H JCPDS 25-284
1			0.48795	0.05							
2			0.37154	0.01							
3	0.33597	0.01	0.33204	0.02	0.33450	0.02					0.3348 (1.00)
4			0.32644	0.02							
5	0.31317	0.17	0.30872	0.10	0.31234	0.18				0.3138 (1.00)	
6			0.28269	0.02							
7			0.28045	0.03							
8			0.27541	0.02							
9	0.26269	0.17	0.25938	0.11	0.26169	0.29	0.263 (0.50)	0.2628 (0.35)	0.263 (0.50)		
10			0.25608	0.01	0.25698	<0.01			0.257 (0.20)		
11	0.25177	1.00	0.24853	1.00	0.25063	1.00	0.253 (1.00)	0.2516 (1.00)	0.251 (1.00)		
12	0.23571	0.15	0.23313	0.10	0.23488	0.62	0.238 (0.60)	0.2357 (0.35)	0.236 (0.40)		
13	0.23261	0.01							0.234 (0.30)		
14	0.21779	0.13	0.21580	0.15	0.21704	0.15	0.218 (0.30)	0.2179 (0.14)	0.217 (0.20)		
15					0.20972	0.06	0.209 (0.20)				
16	0.20298	<0.01									0.2027 (0.15)
17	0.20005	0.02	0.19831	0.02	0.19915	0.02	0.200 (0.20)	0.1999 (0.05)	0.198 (0.10)		
18	0.19206	0.13	0.19039	0.11	0.19099	0.10				0.1920 (0.60)	
19			0.18679	0.09	0.18668	0.02					
20			0.17953	0.01							0.1795 (0.03)
21	0.16794	0.02	0.16642	0.03	0.16695	0.02	0.169 (0.20)	0.16771 (0.06)	0.169 (0.10)		0.1674 (0.06)
22	0.16372	0.06	0.16268	0.07	0.16294	0.13	0.164 (0.20)		0.165 (0.10)	0.1638 (0.35)	
23					0.15842	0.01	0.156 (0.30)				

Table A1. (Continued)

	As-received material		Exposed material — upstream area				Known d, nm, and (intensities)				
			Surface region		Subsurface region						
	d (nm)	Relative intensity	d (nm)	Relative intensity	d (nm)	Relative intensity	α-SiC 33R JCPDS 22-1316	α-SiC 12H JCPDS 29-1128	α-SiC 51R JCPDS 4-0756	Si JCPDS 5-0565	C 4H Graphite 4H JCPDS 25-284
24	0.15408	0.77	0.15324	0.82	0.15324	0.30	0.154 (0.80)	0.15407 (0.43)	0.155 (0.50)		0.1540 (0.04)
25					0.14364	0.01	0.1434 (0.30)		0.143 (0.20)		
26	0.14221	0.05	0.14144	0.07	0.14132	0.04	0.1410 (0.30)	0.14198 (0.12)	0.141 (0.20)		
27			0.13636	0.02							
28	0.13584	0.01			0.13492	0.01				0.1357 (0.08)	
29	0.13291	0.01			0.13212	0.07		0.13291 (0.02)	0.133 (0.10)		
30	0.13147	0.27	0.13085	0.67	0.13066	0.52	0.1313 (0.70)	0.13139 (0.28)	0.131 (0.50)	0.1315 (0.01)	
31	0.12905	0.18	0.12843	0.06	0.12827	0.02	0.1291 (0.80)	0.12897 (0.04)	0.129 (0.10)		
32	0.12595	0.05	0.12527	0.14	0.12518	0.17	0.1260 (0.30)	0.1258 (0.03)	0.126 (0.10)		
33	0.12460	0.02	0.12414	0.06	0.12384	0.01			0.125 (0.10)	0.1246 (0.13)	
34			0.12317	0.04							
35	0.12223	0.01			0.12147	0.01			0.121 (0.10)		0.1228 (0.04)
36	0.11354	0.01	0.11421	0.02	0.11282	0.03			0.114 (0.10)		0.1133 (0.01)
37	0.11087	0.03	0.11054	0.06	0.11011	0.02			0.110 (0.10)	0.11083 (0.17)	
38	0.10902	0.05	0.10857	0.11	0.10830	0.03	0.1091 (0.20)	0.10804 (0.03)	0.109 (0.10)		
39	0.10620	0.02			0.10599	<0.01	0.1072 (0.10)		0.107 (0.20)		
40	0.10452	0.02	0.10424	0.06	0.10388	0.03		0.10441 (0.03)	0.104 (0.10)	0.10450 (0.09)	0.1050 (0.01)
41					0.10303	0.01					
42	0.10067	0.01			0.10010	0.03			0.100 (0.10)		
43	0.10003	0.13	0.09978	0.25	0.09947	0.07	0.0999 (0.40)	0.09998 (0.05)	0.0995 (0.20)		
44	0.09895	0.02	0.09872	0.03	0.09840	0.02	0.0988 (0.40)	0.09890 (0.02)	0.0984 (0.10)		0.0990 (0.04)
45	0.09753	0.14	0.09731	0.12	0.09790	<0.01	0.0975 (0.40)	0.09743 (0.03)	0.0971 (0.20)		

Table A2. X-ray diffraction results for CVD SiC

	As-received material		Exposed material — upstream area				Known d, nm, and (intensities)	
			Surface region		Subsurface region			
	d (nm)	Relative intensity	d (nm)	Relative intensity	d (nm)	Relative intensity	α-SiC 12H JCPDS 29-1128	C 4H Graphite 4H JCPDS 25-284
1			0.49718	0.02				
2			0.33482	<0.01	0.33479	<0.01		0.3348 (1.00)
3			0.29379	0.01				
4			0.29075	0.01				
5			0.28270	0.09				
6			0.27821	<0.01	0.27941	<0.01		
7			0.27063	0.03				
8	0.26598	0.14	0.26442	0.16	0.26482	0.09	0.2628 (0.35)	
9	0.25163	1.00	0.25031	1.00	0.25222	1.00	0.2516 (1.00)	
10	0.21769	0.05	0.21660	0.10	0.21798	0.01	0.2179 (0.14)	
11	0.20240	0.01	0.20291	<0.01			0.1999 (0.05)	0.2027 (0.15)
12			0.18740	0.11				
13	0.15397	0.47	0.15348	0.43	0.15422	0.38	0.15406 (0.43)	0.1540 (0.04)
14					0.14288	0.01	0.14198 (0.12)	
15	0.13152	0.31	0.13091	0.25	0.13145	0.28	0.13139 (0.28)	0.1315 (0.04)
16			0.12884	0.06				
17	0.12603	0.04	0.12552	0.05	0.12610	0.04	0.12580 (0.03)	
18			0.11446	0.01				
19	0.10905	0.02	0.10854	0.01	0.10895	<0.01	0.10804 (0.03)	
20			0.10462	0.01			0.10441 (0.03)	0.1050 (0.01)
21	0.10009	<0.01	0.09986	0.04	0.09998	0.05	0.09998 (0.05)	0.0990 (0.04)
22	0.09757	<0.01	0.09714	0.04	0.09752	<0.01	0.09743 (0.03)	

Table A3. X-ray diffraction results for α-SiC

	As-received material		Exposed material — upstream area				Known d, nm, and (intensities)				
			Surface region		Subsurface region						
	d (nm)	Relative intensity	d (nm)	Relative intensity	d (nm)	Relative intensity	α-SiC 33R JCPDS 22-1316	α-SiC 12H JCPDS 29-1128	α-SiC 4H JCPDS 22-1317	α-SiC 15R JCPDS 22-1301	C Graphite JCPDS 23-64
1			0.54183	0.01							
2					0.50178	0.04					
3	0.33512	0.02	0.33212	0.01	0.33630	0.01					0.336 (1.00)
4					0.30706	0.01					
5			0.28088	0.05	0.27816	0.01					
6	0.26604	0.02			0.26634	0.01			0.2661 (0.20)	0.266 (0.40)	
7	0.26084	0.26	0.26002	0.21	0.26204	0.38	0.263 (0.50)	0.2628 (0.35)			
8	0.25523	0.02	0.25498	<0.01	0.25619	0.06			0.2573 (1.00)	0.258 (0.80)	
9	0.25014	1.00	0.24931	1.00	0.25115	1.00	0.253 (1.00)	0.2516 (1.00)	0.2513 (0.80)	0.251 (0.80)	
10					0.23854	0.04	0.238 (0.60)	0.2357 (0.35)		0.240 (0.70)	
11	0.23441	0.80	0.23364	0.27	0.23530	0.45			0.2352 (0.90)	0.232 (0.60)	
12	0.21718	0.21	0.21611	0.13	0.21759	0.18	0.218 (0.30)	0.2179 (0.14)		0.219 (0.10)	
13	0.20987	0.01			0.21048	0.01	0.209 (0.20)			0.211 (0.30)	
14	0.20781	0.01			0.20803	0.01			0.2084 (0.25)		0.203 (0.50)
15	0.19901	0.08	0.19870	0.04	0.19980	0.08	0.200 (0.20)	0.1999 (0.05)		0.197 (0.10)	
16			0.18716	0.08							
17	0.16998	0.01	0.16981	<0.01	0.16992	0.02	0.169 (0.20)			0.170 (0.20)	
18	0.16723	0.08	0.16699	0.05	0.16774	0.09	0.164 (0.20)	0.16771 (0.06)			0.1678 (0.80)
19	0.16030	0.02	0.16029	<0.01	0.16066	0.01			0.1604 (0.30)		
20	0.15901	0.01	0.15909	<0.01	0.15947	0.02				0.159 (0.60)	
21	0.15552	0.01			0.15568	0.01	0.156 (0.30)				
22	0.15360	0.74	0.15336	0.43	0.15394	0.81	0.154 (0.80)	0.15407 (0.43)	0.1537 (0.45)	0.154 (1.00)	0.1544 (0.10)
23	0.14399	0.04	0.14391	0.02	0.14429	0.02	0.1434 (0.30)			0.1444 (0.60)	

Table A3. (Continued)

	As-received material		Exposed material — upstream area				Known d, nm, and (intensities)				
			Surface region		Subsurface region						
	d (nm)	Relative intensity	d (nm)	Relative intensity	d (nm)	Relative intensity	α-SiC 33R JCPDS 22-1316	α-SiC 12H JCPDS 29-1128	α-SiC 4H JCPDS 22-1317	α-SiC 15R JCPDS 22-1301	C Graphite JCPDS 23-64
24	0.14177	0.26	0.14160	0.13	0.14207	0.24	0.1410 (0.30)	0.14198 (0.12)	0.1418 (0.40)		
25	0.13958	0.01			0.13987	0.01				0.1398 (0.40)	
26					0.13706	<0.01					
27	0.13261	0.04	0.13217	0.03	0.13283	0.06		0.13291 (0.02)		0.1320 (0.20)	
28	0.13115	0.63	0.13098	0.30	0.13139	0.76	0.1313 (0.70)	0.13139 (0.28)	0.1311 (0.35)	0.1311 (0.90)	
29	0.12869	0.09	0.12854	0.06	0.12892	0.13	0.1291 (0.30)	0.12897 (0.04)	0.1286 (0.25)	0.1297 (0.20)	
30	0.12559	0.03	0.12546	0.05	0.12575	0.08	0.1260 (0.30)	0.12580 (0.03)		0.1257 (0.20)	
31	0.21291	0.05	0.12174	0.01	0.12210	0.06					0.1232 (0.30)
32			0.11476	<0.01							
33	0.11335	0.04	0.11330	0.01	0.11347	0.04					0.1138 (0.05)
34	0.11045	<0.01	0.11062	<0.01	0.11078	0.01			0.1110 (0.15)	0.1105 (0.30)	
35	0.10888	0.12	0.10876	0.03	0.10897	0.10	0.1091 (0.20)	0.10894 (0.03)		0.1089 (0.20)	
36	0.10653	0.02	0.10662	0.01	0.10658	0.02	0.1072 (0.10)			0.1053 (0.40)	
37	0.10439	0.09	0.10430	0.03	0.10447	0.09	0.1044 (0.30)	0.10441 (0.03)	0.1042 (0.30)	0.1035 (0.40)	
38	0.10056	0.01	0.10068	<0.01	Not analyzed				0.1001 (0.20)	0.1000 (0.60)	
39	0.09996	0.09	0.09978	0.06	Not analyzed		0.0999 (0.40)	0.09998 (0.05)		0.0990 (0.30)	0.0994 (0.40)
40	0.09884	0.04	0.09867	0.03	Not analyzed		0.0988 (0.40)	0.09890 (0.02)	0.09863 (0.20)	0.0984 (0.30)	
41	0.09748	0.08	0.09732	0.05	Not analyzed		0.0975 (0.40)	0.09743 (0.03)	0.09744 (0.15)	0.0975 (0.60)	

Table A4. X-ray diffraction results for as-received sialon

	Experimental results				Known d, nm, and (intensities)			
	Outer surface		Inner surface		β'-Si_2N_4 JCPDS 29-1132	$Si_3Al_{2.67}N_4O_4$ JCPDS 25-1492	β'-sialon $Si_2Al_4N_4O_4$[a,b]	Mg-sialon 6H[a,b]
	d (nm)	Relative intensity	d (nm)	Relative intensity				
1	0.71296	0.03	0.71185	0.01				
2	0.66198	0.03	0.66819	0.21	0.658 (0.42)	0.665 (0.40)	0.6679 (m)	
3			0.51965	<0.01				
4	0.37880	0.01	0.38512	0.35	0.380 (0.42)	0.384 (0.40)	0.3856 (m)	
5	0.32725	0.24	0.3325	0.95	0.329 (1.00)	0.332 (0.75)	0.3339 (vs)	0.3271 (w)
6	0.28387	0.01						
7	0.27420	0.75	0.27756	0.30			0.2740 (vs)	
8			0.27180	0.91		0.2714 (0.90)		0.2722 (s)
9	0.26604	0.29	0.26676	0.16	0.266 (0.95)			0.2650 (vs)
10	0.26227	0.10	0.26134	0.19				0.2616 (w)
11	0.25770	0.98						
12	0.24780	1.00	0.25161	1.00	0.249 (0.95)	0.2513 (0.90)	0.2524 (vs)	
13	0.23660	0.59	0.24060	0.13			0.2370 (w)	02383 (s)
14	0.23346	0.01	0.23511	0.10		0.2350 (0.15)		0.2333 (w)
15	0.23122	0.07	0.23157	0.04	0.231 (0.06)			
16	0.22848	0.06						
17	0.21869	0.21	0.2217	0.36	0.218 (0.33)	0.2216 (0.50)	0.2226 (s)	0.2224 (m)
18	0.21481	0.18	0.21619	0.03				
19	0.21247	0.13						
20	0.19883	0.11	0.20144	0.04				0.2057 (w)
21	0.19554	0.51	0.19729	0.03				
22	0.19381	0.14	0.19189	0.11	0.1902 (0.08)	0.1919 (0.20)	0.1933 (w)	
23	0.18872	0.07			0.1892 (0.05)			0.1899 (vs)
24	0.18203	0.42	0.18468	0.17	0.1827 (0.12)	0.1844 (0.25)	0.1852 (mw)	
25	0.17654	0.07	0.17754	0.34		0.1777 (0.60)	0.1789 (s)	
26	0.17688	0.18	0.17546	0.07	0.1753 (0.35)			0.1751 (w)
27	0.17263	0.14						
28	0.16574	0.06	0.16823	<0.01		0.1662 (0.01)		
29			0.16123	0.13	0.1592 (0.11)	0.1612 (0.30)	0.1623 (m)	
30	0.15839	0.08						
31	0.15672	0.05	0.1568	0.06		0.1567 (0.19)	0.1577 (mw)	
32			0.15404	<0.01	0.1548 (0.06)			
33			0.15356	0.02			0.1532 (m)	0.1531 (vs)
34	0.15147	0.33	0.15231	0.14	0.1511 (0.14)	0.1525 (0.35)		
35	0.14900	0.90				0.1487 (0.40)	0.1562 (m)	0.1497 (m)
36	0.14675	0.16	0.14860	0.13	0.1455 (0.14)		0.1457 (mw)	
37	0.14403	0.01	0.14512	0.11	0.1438 (0.07)	0.1451 (0.25)		

Table A4. (Continued)

	Experimental results				Known d, nm, and (Intensities)			
	Outer surface		Inner surface		β'-Si_2N_4 JCPDS 29-1132	$Si_3Al_{2.67}N_4O_4$ JCPDS 25-1492	β'-sialon $Si_2Al_4N_4O_4$[a,b]	Mg-sialon 6H[a,b]
	d (nm)	Relative Intensity	d (nm)	Relative Intensity				
38	0.14250	0.06	0.14250	0.01	0.1434 (0.06)			
39	0.13819	0.04	0.13876	0.02		0.1386 (0.14)	0.1400 (vw)	0.1391 (m)
40			0.13556	0.42	0.1359 (0.02)	0.1357 (1.00)	0.1365 (vs)	
41	0.13408	0.15	0.13398	0.02	0.1341 (0.40)		0.1336 (w)	0.1335 (m)
42	0.13244	0.18	0.13287	0.05	0.1331 (0.08)	0.1330 (0.08)		0.1326 (w)
43	0.13115	0.09					0.1311 (s)	
44	0.12988	0.42	0.13057	0.18	0.1289 (0.20)	0.1304 (0.60)	[c]	0.1309 (w)
45	0.12833	0.18						[c]
46	0.12802	0.09	0.12786	0.17	0.1268 (0.06)	0.1279 (0.60)		
47	0.12591	0.04	0.12557	0.02	0.1257 (0.16)	0.1256 (0.04)		
48	0.12478	0.13	0.12101	<0.01		0.1214 (0.06)		
49			0.11952	0.02	0.1200 (0.02)	0.1194 (0.06)		
50	0.11830	0.39			0.1184 (0.01)			
51	0.11722	0.03	0.11744	0.02		0.1175 (0.06)		
52			0.11574	0.06	0.1156 (0.02)			
53	0.11392	0.05						
54	0.11244	0.04			0.1138 (0.04)			
55			0.11079	0.03				
56	0.10958	0.18	0.10932	0.03	0.1096 (0.04)			
57	0.10762	0.03	0.10872	<0.01	0.1083 (0.03)			
58	0.10639	0.02	0.10638	0.06	0.1055 (0.01)			
59	0.10479	0.02	0.10477	0.01	0.1048 (0.07)			
60	0.10323	0.06	0.10373	0.04				
61	0.10176	0.02	0.10236	0.01	0.1023 (0.04)			
62	0.10075	0.03	0.10138	0.02	0.1045 (0.02)			

[a] Letters in parentheses represent diffraction line intensities where vw = very weak, w = weak, mw = medium weak, m = medium, s = strong, and vs = very strong.

[b] Data from G. K. Layden, *Development of SiAlON Materials*, CR-135290, United Technologies Research Center, East Hartford, Conn., December 1977, and K. H. Jack, "X-Ray Data for Sialons and Other Nitrogen Ceramic Phases," unpublished data, Dept. of Metallurgy and Engineering Materials Crystallographic Laboratory, University of Newcastle Upon Tyne, England.

[c] d-spacings below preceding value not given.

Table A5. X-ray diffraction results for sialon exposed in CRAF

	Experimental results				Known d, nm, and (intensities)						
	Surface region-upstream		Subsurface-upstream		β'-Si_3N_4 JCPDS 29-1132	$Si_3Al_{2.67}N_6O_4$ JCPDS 25-1492	β'-sialon $Si_2Al_4N_4O_4$ [a,b]	Mg-sialon 8H [a,b]	Alpha cristobalite SiO_2 JCPDS 11-695	α-$Mg_2Al_4Si_5O_{18}$ JCPDS 13-293	Sillimanite $Al_2O_3 \cdot SiO_2$ JCPDS 10-369
	d (nm)	Relative Intensity	d (nm)	Relative Intensity							
1	0.82650	0.04								0.848 (1.00)	
2	0.65067	0.19	0.64402	0.17	0.658 (0.42)	0.665 (0.40)	0.6680 (m)				
3	0.53075	0.02									0.535 (0.70)
4	0.5094	0.02									
5	0.48562	0.01								0.489 (0.30)	
6	0.45931	0.04	0.45702	0.03						0.4679 (0.16)	0.456 (0.30)
7	0.40442	0.09							0.405 (1.00)	0.4094 (0.50)	
8	0.37902	0.30	0.37707	0.30	0.380 (0.42)	0.384 (0.40)	0.3857 (m)				0.373 (0.50)
9	0.36331	0.01							0.353 (0.04)		
10	0.33920	0.05								0.3379 (0.50)	0.341 (0.90)
11	0.33475	0.11				0.332 (0.75)	0.3342 (vs)				0.336 (1.00)
12	0.32876	0.83	0.32744	0.85	0.329 (1.00)						
13	0.31078	0.03							0.314 (0.12)	0.3138 (0.65)	0.319 (0.10)
14	0.30089	0.04								0.3027 (0.05)	
15	0.28410	0.04	0.28169	0.08					0.2841 (0.14)		0.283 (0.70)
16	0.27562	0.07	0.27523	0.35		0.2714 (0.90)	0.2741 (vs)				
17	0.26869	0.86	026785	0.80	0.266 (0.95)			0.2670 (vs)			0.268 (0.80)
18	0.26408	0.16	0.26320	0.12				0.2043 (s)		0.2640 (0.25)	
19	0.26018	0.08	0.25939	0.04				0.2589 (mw)			
20	0.25289	0.07				0.2513 (0.90)	0.2525 (vs)				0.253 (0.90)
21	0.24930	1.00	0.24863	1.00	0.249 (0.95)			0.24971 (mw)	0.2485 (0.20)		
22	0.24206	0.11	0.24137	0.06						0.2414 (0.04)	0.242 (0.60)
23	0.23876	0.06	0.23773	0.03		0.2350 (0.15)	0.2371 (w)	0.2383 (s)			0.237 (0.10)
24	0.23306	0.07	0.23219	0.07	0.231 (0.06)			0.2349 (mw)		0.2338 (0.12)	0.230 (0.30)

Table A5. (Continued)

	Experimental results				Known d, nm, and (intensities)						
	Surface region-upstream		Subsurface-upstream		β'-Si_3N_4 JCPDS 29-1132	$Si_3Al_{2.67}N_4O_4$ JCPDS 25-1492	β'-sialon $Si_2Al_4N_4O_4$ [a,b]	Mg-sialon 8H [a,b]	Alpha cristobalite SiO_2 JCPDS 11-695	α-$Mg_2Al_4Si_5O_{18}$ JCPDS 13-293	Sillimanite $Al_2O_3 \cdot SiO_2$ JCPDS 10-369
	d (nm)	Relative intensity	d (nm)	Relative intensity							
25	0.21987	0.33	0.21925	0.28	0.218 (0.33)	0.2216 (0.50)	0.2234 (s)				0.220 (1.00)
26	0.21655	0.08	0.21596	0.09						0.2165 (0.06)	
27	0.21472	0.02						0.2128 (w)			
28	0.21076	0.02	0.21121	0.01				0.2114 (w)		0.2108 (0.08)	0.210 (0.60)
29	0.20081	0.07	0.20039	0.06				0.2001 (w)		0.2098 (0.12)	
30			0.19510	0.01							
31	0.19068	0.12	0.19041	0.13	0.1902 (0.08)	0.1919 (0.20)	0.1926 (w)			0.1904 (0.04)	
32	0.18740	0.07	0.18729	0.11	0.1892 (0.05)			0.1878 (s)	0.1870 (0.08)	0.1875 (0.16)	0.1868 (0.50)
33	0.18562	0.06				0.1844 (0.25)	0.1852 (mw)				
34	0.18326	0.14	0.18316	0.12	0.1827 (0.12)						0.1829 (0.60)
35	0.17662	0.28	0.17630	0.34	0.1753 (0.35)	0.1777 (0.60)	0.1789 (s)	0.1764 (w)			
36	0.17451	0.06	0.17415	0.06							0.1705 (0.50)
37	0.16808	0.02							0.1680 (0.04)	0.16882 (0.30)	0.1679 (0.70)
38	0.16027	0.11	0.16020	0.10	0.1592 (0.11)	0.1612 (0.30)	0.1622 (m)		0.1612 (0.08)		
39	0.15864	0.03	0.15815	0.02			0.1575 (mw)			0.15885 (0.10)	0.1595 (0.70)
40	0.15589	0.06	0.15562	0.06		0.1567 (0.19)					0.1559 (0.30)
41			0.15476	0.05	0.1548 (0.06)			0.1542 (vs)			
42	0.15312	0.02	0.15285	0.01		0.1525 (0.35)	0.1532 (m)				0.1535 (0.20)
43	0.15168	0.13	0.15167	0.13	0.1511 (0.14)		0.1503 (m)				0.1516 (0.90)
44	0.14769	0.09	0.14762	0.10		0.1487 (0.40)		0.1471 (m)	0.1494 (0.06)	0.14935 (0.08)	0.1467 (0.10)
45	0.14437	0.10	0.14434	0.10	0.1455 (0.14)	0.1451 (0.25	0.1458 (mw)				0.1450 (0.40)
46	0.14240	0.06	0.14216	0.07	0.1438 (0.07)				0.1431 (0.44)		0.1440 (0.70)
47	0.13508	0.32	0.13508	0.32	0.1341 (0.40)	0.1357 (1.00)	0.1365 (vs)		0.1352 (0.04)		0.1343 (0.10)
48	0.13374	0.08	0.13362	0.05	0.1331 (0.08)	0.1330 (0.08)	0.1335 (w)	0.1335 (w)	0.1333 (0.04)		0.1337 (0.70)

Table A5. (Continued)

	Experimental results				Known d, nm, and (intensities)						
	Surface region-upstream		Subsurface-upstream		β'-Si_3N_4 JCPDS 29-1132	$Si_3Al_{2.67}N_4O_4$ JCPDS 25-1492	β'-sialon $Si_2Al_4N_4O_4$[a,b]	Mg-sialon BH[a,b]	Alpha cristobalite SiO_2 JCPDS 11-695	α-$Mg_2Al_4Si_5O_{18}$ JCPDS 13-293	Sillimanite $Al_2O_3 \cdot SiO_2$ JCPDS 10-369
	d (nm)	Relative Intensity	d (nm)	Relative Intensity							
49	0.13268	0.07	0.13250	0.03	0.1318 (0.04)		0.1311 (s)	0.1332 (s)			[c]
50	0.12983	0.16	0.12979	0.16	0.1289 (0.20)	0.1304 (0.60)	[c]	[c]	0.1299 (0.04)		
51	0.12850	0.05	0.12851	0.03		0.1279 (0.60)			0.1281 (0.04)		
52	0.12730	0.14	0.12728	0.13							
53	0.12589	0.03			0.1263 (0.06)	0.1256 (0.04)					
54	0.12530	0.04	0.12510	0.02	0.1257 (0.16)						
55	0.12384	0.01							0.1242 (0.02)		
56	0.12322	0.01							0.1233 (0.02)		
57	0.12088	<0.01	0.12074	0.01	0.1200 (0.02)	0.1214 (0.06)			0.1210 (0.04)		
58	0.11884	0.01	0.11897	<0.01	0.1183 (0.01)	0.1194 (0.06)			0.1183 (0.02)		
59	0.11694	0.01	0.11688	0.02	0.1156 (0.02)	0.1175 (0.06)			[c]		
60	0.11047	0.05	0.11045	0.02		[c]					

[a] Letters in parentheses represent diffraction line intensities where vw = very weak, w = weak, mw = medium, weak, m = medium, s = strong, and vs = very strong.

[b] Data from G. K. Layden, *Development of SiAlON Materials*, CR-135290, United Technologies Research Center, East Hartford, Conn., December 1977, and K. H. Jack, "X-Ray Data for Sialons and Other Nitrogen Ceramic Phases," unpublished data, Dept. of Metallurgy and Engineering Materials Crystallographic Laboratory, University of Newcastle Upon Tyne, England.

[c] d-spacings below preceding value not given.

Table A6. X-ray diffraction results for Al_2O_3

	As-received material		Exposed material — upstream area				Known d, nm, and (Intensities)		
			Surface region		Subsurface region				
	d (nm)	Relative Intensity	d (nm)	Relative Intensity	d (nm)	Relative Intensity	α-Al_2O_3 JCPDS 10-173	Tridymite SiO_2 JCPDS 14-260	Alpha quartz α-SiO_2 JCPDS 5-0490
1			0.42682	0.19				0.4268 (1.00)	0.426 (0.35)
2			0.38318	0.05				0.3832 (0.50)	
3	0.34702	0.61	0.34679	0.23	0.34412	0.20	0.3479 (0.75)	0.3432 (0.40)	0.3343 (1.00)
4					0.31657	1.00		0.3162 (0.20)	
5			0.26810	<0.01					
6	0.25446	0.69	0.25402	0.61	0.25308	0.28	0.2552 (0.90)		
7			0 25031	0.01				0.2493 (0.60)	
8			0.24275	<0.01	0.24187	<0.01			0.2458 (0.12)
9	0.23738	0.21	0.23735	0.13	0.23613	0.11	0.2379 (0.40)	0.2367 (0.30)	
10			0.22979	<0.01				0.2303 (0.50)	0.2282 (0.12)
11	0.21604	0.10	0.21624	0.04	0.21519	<0.01	0.2165 (<0.01)	0.21185 (0.30)	
12	0.20822	0.66	0.20764	1.00	0.20733	0.27	0.2085 (1.00)		
13	0.19613	0.01	0.19562	0.02	0.19554	<0.01	0.1964 (0.02)		
14	0.17368	1.00	0.17338	0.40	0.17315	0.13	0.1740 (0.45)		
15	0.15989	0.54	0.15966	0.73	0.15948	0.23	0.1601 (0.80)		
16	0.15439	0.02	0.15427	0.01	0.15407	0.01	0.1546 (0.04)		0.1841 (0.15)
17	0.15133	0.04					0.1514 (0.06)		
18	0.15099	0.06	0.15054	0.07	0.15041	0.02	0.1510 (0.08)		
19			0.14220	<0.01					
20	0.14037	0.65	0.13984	0.31	0.13996	0.08	0.1404 (0.30)		
21	0.13704	0.20	0.13683	0.14	0.13697	0.14	0.1374 (0.50)		0.1375 (0.11)
22	0.13362	0.01	0.13315	0.01	0.13321	<0.01	0.1337 (0.02)		
23	0.12746	0.02	0.12704	0.03	0.12724	<0.01	0.1276 (0.04)		
24	0.12390	0.08	0.12358	0.26	0.12358	0.04	0.1239 (0.10)		
25	0.12336	0.10	0.12302	0.18			0.12343 (0.08)		
26			0.11892	0.01					
27	0.11897	0.09	0.11858	0.08	0.11864	0.01	0.11898 (0.08)		
28	0.11596	0.01	0.11564	0.01	0.11578	<0.01	0.11600 (<0.01)		
29	0.11466	0.020	0.11439	0.03	0.11443	0.01	0.11470 (0.06)		
30	0.11246	0.03	0.11225	0.03			0.11255 (0.06)		
31			0.11206	0.04			0.11246 (0.04)		
32	0.10989	0.08	0.10962	0.12	0.10960	0.01	0.10988 (0.08)		
33	0.10825	0.02	0.10795	0.06	0.10808	0.02	0.10831 (0.04)		
34	0.10780	0.07	0.10752	0.02	0.10759	0.01	0.10781 (0.08)		
35	0.10423	0.15	0.10397	0.03	0.10407	0.03	0.10426 (0.14)		
36	0.10177	0.02	0.10149	0.09	0.10157	0.01	0.10175 (0.02)		
37	0.09977	0.16	0.09953	0.11	0.09960	0.03	0.09976 (0.12)		
38			0.09829	0.01	0.09842	<0.01	0.09857 (0.01)		
39	0.09822	0.06	0.09796	0.01	0.09807	<0.01	0.09819 (0.04)		

Table A7. X-ray diffraction results for upstream coal slag

	Experimental results		Known d, nm, and (intensities)						
	d (nm)	Relative intensity	Alpha quartz α-SiO_2 JCPDS 5-0490	Alpha cristobolite SiO_2 JCPDS 11-695	Beta cristobolite SiO_2 JCPDS 4-0359	Tridymite SiO_2 JCPDS 14-260	$Fe(Al,Cr)_2O_4$ JCPDS 1-1129	Hematite α-Fe_2O_3 JCPDS 13-534	Mullite $3Al_2O_3{\cdot}2SiO_2$ JCPDS 15-776
1	0.5352 (0.08)	0.09							0.539 (0.50)
2	0.42584	0.12	0.426 (0.35)			0.4268 (1.00)			
3	0.41330	0.53			0.415 (1.00)				
4	0.40168	0.32		0.405 (1.00)		0.4075 (0.90)			
5	0.37757	0.05				0.3800 (0.90)			0.3774 (0.08)
6	0.36061	0.50				0.3609 (0.40)		0.366 (0.25)	
7	0.35163	0.04		0.353 (0.04)					
8	0.33929	0.26							0.339 (1.00)
9	0.33595	0.36	0.3343 (1.00)						
10	0.32433	0.05							
11	0.31589	0.16		0.314 (0.12)					
12	0.29176	0.14			0.292 (0.05)		0.291 (0.25)		
13	0.28048	0.17		0.2841 (0.14)					0.2886 (0.20)
14	0.26652	0.80						0.269 (1.00)	0.2694 (0.40)
15	0.25126	0.53			0.253 (0.80)			0.251 (0.50)	0.2524 (0.50)
16	0.24853	1.00	0.2458 (0.12)	0.2485 (0.20)		0.2493 (0.60)	0.248 (1.00)		
17	0.24206	0.05		0.2445 (0.06)					0.2428 (0.14)
18	0.23944	0.07							0.2393 (<0.02)
19	0.22857	0.04	0.2282 (0.12)			0.2286 (0.50)		0.2285 (0.02)	0.2292 (0.20)
20	0.22539	0.12							
21	0.21712	0.36			0.217 (0.10)			0.2201 (0.30)	0.2206 (0.60)
22	0.21299	0.08	0.2128 (0.09)	0.2118 (0.06)		0.2130 (0.30)			0.2121 (0.25)
23	0.20832	0.14			0.207 (0.30)	0.2088 (0.40)		0.2070 (0.02)	
24	0.20461	0.12	0.1980 (0.06)	0.2019 (0.04)	0.199 (0.05)	0.20455 (0.30)	0.205 (0.25)		
25	0.18724	0.26		0.1870 (0.08)		0.18705 (0.30)			0.1887 (0.08)
26	0.18397	0.22				α		0.1838 (0.40)	0.1841 (0.10)

Table A7. (Continued)

	Experimental results		Known d, nm, and (intensities)						
	d (nm)	Relative intensity	Alpha quartz α-SiO_2 JCPDS 5-0490	Alpha cristobolite SiO_2 JCPDS 11-695	Beta cristobolite SiO_2 JCPDS 4-0359	Tridymite SiO_2 JCPDS 14-260	$Fe(Al,Cr)_2O_4$ JCPDS 1-1129	Hematite α-Fe_2O_3 JCPDS 13-534	Mullite $3Al_2O_3 \cdot 2SiO_2$ JCPDS 15-776
27	0.18241	0.21	0.1817 (0.17)						
28	0.17866	0.28			0.1795 (0.05)				
29	0.16660	0.09	0.1672 (0.07)		0.169 (0.05)		0.167 (0.04)	0.1680 (0.60)	
30	0.16437	0.15			0.1651 (0.60)			0.1634 (0.04)	
31	0.15995	0.07						0.1596 (0.10)	0.15999 (0.20)
32	0.15846	0.05					0.158 (0.35)		0.15786 (0.12)
33	0.15245	0.17							0.15242 (0.35)
34	0.14927	0.24						0.1484 (0.35)	
35	0.14734	0.27			0.1460 (0.50)		0.146 (0.40)		
36	0.14412	0.20		0.1431 (0.44)				0.1452 (0.15)	0.14421 (0.18)
37	0.14139	0.12							
38	0.13347	0.05						0.1349 (0.04)	0.13356 (0.12)
39	0.13008	0.10						0.1310 (0.20)	
40	0.12798	0.08	0.1288 (0.30)		0.1266 (0.30)				
41	0.12506	0.06	0.1256 (0.04)				0.126 (0.04)	0.1258 (0.08)	
42	0.12362	0.09			0.1210 (0.30)		0.121 (0.04)		
43	0.11809	0.04	0.11802 (0.04)					0.1189 (0.08)	
44	0.11540	0.05	0.11530 (0.02)						
45	0.11332	0.06			0.1131 (0.20)				
46	0.10964	0.07			0.1090 (0.05)				
47	0.10685	0.53					0.107 (0.08)		
48	0.10485	0.07							
49	0.10247	0.04			0.1030 (0.05)				
50	0.09816	0.06			0.1001 (0.10)			0.09890 (0.10)	

[a] d-spacings below preceding value not given.

ORNL/TM-7958

INTERNAL DISTRIBUTION

1–2. Central Research Library
3. Document Reference Section
4–5. Laboratory Records Department
6. Laboratory Records, ORNL RC
7. ORNL Patent Section
8. V. B. Baylor
9. P. F. Becher
10. R. A. Bradley
11. W. H. Butler
12. P. T. Carlson
13. J. A. Carpenter, Jr.
14. G. M. Caton
15. E. L. Churnetski
16. J. H. DeVan
17. J. R. DiStefano
18. R. G. Donnelly
19. J. S. Faulkner
20. J. I. Federer
21–25. M. K. Ferber
26. C. B. Finch
27. B. E. Foster
28. T. G. Godfrey, Jr.
29. W. A. Hartman
30–32. M. R. Hill
33. R. S. Holcomb
34. J. K. Huffstetler
35. D. R. Johnson
36. J. E. Jones, Jr.
37. R. R. Judkins
38. R. P. Krishnan
39. J. J. Kurtz
40. W. J. Lackey, Jr.
41. K. H. Lin
42. R. A. McKee
43. L. E. McNeese
44. G. S. Painter
45. P. L. Rittenhouse
46. A. C. Schaffhauser
47. M. Siman-Tov
48. G. M. Slaughter
49. J. O. Stiegler
50–54. V. J. Tennery
55. C. S. Yust
56. A. L. Bement, Jr. (Consultant)
57. E. H. Kottcamp, Jr. (Consultant)
58. Alan Lawley (Consultant)
59. T. B. Massalski (Consultant)
60. R. H. Redwine (Consultant)
61. K. M. Zwilsky (Consultant)

EXTERNAL DISTRIBUTION

62. AIRESEARCH MANUFACTURING COMPANY, 111 South 34th Street, P.O. Box 5217, Phoenix, AR 85010

    David R. Richerson

63. AIRESEARCH MANUFACTURING COMPANY OF CALIFORNIA, 2525 W. 190th St., Torrance, CA 90509

    David M. Kotchick

64–65. ARGONNE NATIONAL LABORATORY, 9700 South Cass Avenue, Argonne, IL 60439

    Dave Kupperman
    Roger B. Poeppel

66. ARMCO, INC. RESEARCH AND TECHNOLOGY, 703 Curtis Street, Middletown, OH 45043

    Bruce H. Baker

67. BABCOCK AND WILCOX COMPANY, 1562 Beeson St., P.O. Box 835, Alliance, OH 44601

    W. E. Leyda

68. BABCOCK AND WILCOX COMPANY, P.O. Box 1260, Lynchburg, VA 24505

    Bill Long

69. BETHLEHEM STEEL CORPORATION, HOMER RESEARCH LABORATORY, Bethlehem, PA 18017

    R. H. Herron

70. CARBORUNDUM COMPANY, P.O. Box 832, Niagara Falls, NY 14302

    Gary W. Weber

71. COMBUSTION ENGINEERING, INC., P.O. Box 828, Valley Forge, PA 19482

    J. R. Friedrichs

72. COORS PORCELAIN COMPANY, 600 9th Street, Golden CO 80401

    Donald W. Roy

73. DORNIER-SYSTEM GmbH, Postfach 1360, 7990 Friedrichshafen 1, Federal Republic of Germany

    Gerd Willmann

74. ENERGY AND ENVIRONMENTAL ANALYSIS, INC., 1111 N. Nineteenth Street, Arlington, VA 22209

    Viren Kotheri

75. GAS RESEARCH INSTITUTE, 8600 West Bryn Mawr Avenue, Chicago, IL 60631

    Charles J. Dobos

76. GENERAL ATOMIC COMPANY, P.O. Box 81608, San Diego, CA 92138

    R. W. Schleicher

77. HAGUE INTERNATIONAL, 3 Adams Street, South Portland, ME 04106

    Stephen B. Young

78. HOT WORK INTERNATIONAL, 606 North Broadway, Lexington, KY 40408

    John Newby

79. INDUSTRIAL PROGRAMS, OFFICE OF ASSISTANT SECRETARY, Conservation and Solar Energy, Forrestal Building, 1000 Independence Building, Room 2H085, Washington, DC 20585

James W. Osborne

80. KYOCERA INTERNATIONAL, INC., 8611 Balboa Avenue, San Diego, CA 92123

Edwin H. Kraft

81. LOS ALAMOS NATIONAL LABORATORY, Los Alamos, NM 87545

F. D. Gac

82. LUCAS RESEARCH CENTRE, Shirley Solihull, West Midlands B90 4JJ, England

Roger Hunt

83. NORTON COMPANY, Industrial Ceramics Division, Worcester, MA 01606

David P. Reed

84. ROCKWELL INTERNATIONAL CORPORATION, Rocketdyne Division, 6633 Canoga Avenue, Canoga Park, CA 91304

Harry W. Carpenter

85. SOLAR TURBINES INTERNATIONAL, P.O. Box 80966, San Diego, CA 92138

Michael E. Ward

86. THERMAL TRANSFER, 1100 Roco Road, Monroeville, PA 15146

Gordon L. Hanson

87. UKAEA, SPRINGFIELDS NUCLEAR POWER DEVELOPMENT LABORATORIES, Salwick Preston PR4 ORR, United Kingdom

Peter Kennedy

88. UNITED STATES STEEL CORPORATION, 125 Jameson Lane, Monroeville, PA 15146

Bill Vance

89. UNITED TECHNOLOGIES RESEARCH CENTER, 400 Main Street, East Hartford, CT 06108

D. J. McFarlin

90. DOE, OFFICE OF FOSSIL ENERGY, Washington, DC 20545

S. J. Dapkunas

91. DOE, IDAHO OPERATIONS OFFICE, 550 2nd Street, Idaho Falls, ID 83401

W. H. Thielbahr

92. DOE, OFFICE OF COAL UTILIZATION SYSTEMS, MS E-178 GTN, Washington, DC 20545

Jorgen Birkeland

93. DOE, PITTSBURGH ENERGY TECHNOLOGY CENTER, P.O. Box 10940, Pittsburgh, PA 15236

James D. Hickerson

94-95. DOE, OAK RIDGE OPERATIONS OFFICE, P.O. Box E, Oak Ridge, TN 37830

E. E. Hoffman

Office of Assistant Manager for Energy Research and Development

96-122. DOE, TECHNICAL INFORMATION CENTER, OFFICE OF INFORMATION SERVICES, P.O. Box 62, Oak Ridge, TN 37830

☆U.S. GOVERNMENT PRINTING OFFICE: 1981-546-087/349